ENS DE LYON

UNIVERSITÉ DE LYON

École Normale Supérieure de Lyon
Habilitation à Diriger des Recherches

Ludovic Bellon

Laboratoire de Physique - CNRS UMR 5672

Exploring nano-mechanics through thermal fluctuations

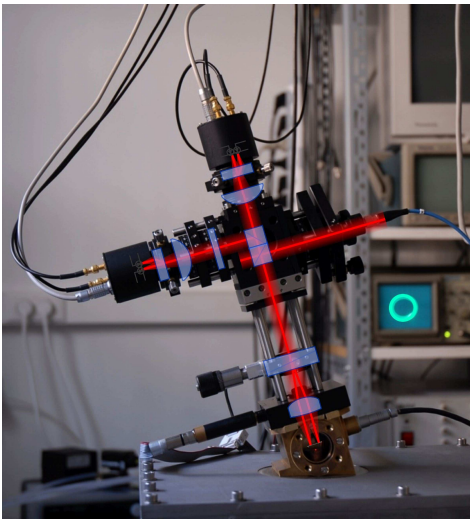

Soutenance publique le 23 novembre 2010
devant le jury constitué de :

Arezki Boudaoud	Président
Joël Chevrier	Rapporteur
Matteo Ciccotti	Rapporteur
Philippe Poncharal	Rapporteur
Mark Rutland	Examinateur

ENS de Lyon, 15 parvis René-Descartes, BP 7000, 69342 Lyon cedex 07

N° d'ordre : 024

Remerciements

Ce mémoire résume 7 années de recherches effectuées au sein du Laboratoire de Physique de l'ENS Lyon. Il est le résultat de mon travail, bien sûr, mais aussi de l'émulation de mes collègues dans l'excellente ambiance de travail que nous offre ce laboratoire. Je tiens à remercier ici tous ceux qui ont contribué, de près ou de loin, à la réussite de mes investigations scientifiques.

Je commencerai naturellement par Piero Paolino, mon premier étudiant en thèse, qui m'a accordé sa confiance en s'embarquant dans l'aventure d'une thèse sur un instrument en développement, avec un directeur novice. Pour son investissement dans l'expérience, son travail au laboratoire et au-delà, mais aussi pour son amitié, je lui adresse un *grazie mille* !

Mes remerciements vont ensuite à tous mes collègues du laboratoire : Sergio Ciliberto, pour ses conseils et encouragements, nos nombreuses discussions scientifiques, mais aussi pour avoir financé à fonds perdus une grande partie de mes recherches sans demander aucun retour ; Artyom Petrosyan, pour ses conseils éclairés en optique et ses connaissances pratiques encyclopédiques ; Audrey Steinberger pour la relecture méticuleuse de mon manuscrit ; Angel Alastuey pour m'avoir sorti de quelques impasses analytiques ; Cendrine Moskalenko pour ses conseils avisés d'utilisatrice d'AFM ; Patrick Flandrin et Stéphane Roux pour m'avoir donné quelques ficelles de l'analyse temps fréquence ; Jean-François Pinton pour la motivation et la bonne humeur contagieuse qu'il sait transmettre à tout le laboratoire ; Franck Ropars et le service d'électronique, Franck Vittoz et l'atelier de mécanique pour leurs réponses toujours souriantes à mes demandes farfelues ; Laurence Mauduit, Nadine Clervaux et Laure Dumazel qui dégrippent pour nous les rouages administratifs complexes ; François Delduc pour ses encouragements lors de ma première direction de thèse ; Marc Pannunzio et Julien Lopez pour leur travail instrumental pendant leurs stages...

Au-delà du laboratoire, je souhaite également remercier mes voisins lyonnais et la communauté française du champ proche pour son accueil en-

thousiaste du petit nouveau aux idées décalées (comment ? construire son AFM ? un AFM sans échantillon ?), notamment lors des forums annuels de microscopies à sonde locale... Merci donc à Agnès Piednoir, Brice Gautier, Armel Descamps, David Albertini, Georges Bremond, Christelle Guerret, Christian Frétigny, Jean-Pierre Aimé, François Bertin, Joël Chevrier, qui ont su me mettre en confiance et ont cru dans le potentiel de mon approche. Merci également à Benoit Roman pour nos discussions sur les expériences et ses conseils pour dompter l'Elastica.

Ces travaux de recherches reposent également sur diverses collaborations, et je remercie notamment Bruno Tiribilli et Massimo Vassalli de Florence, et Jean-Pierre Aimé, Sophie Marsaudon et Julien Buchoux de Bordeaux. Merci aussi à tous ceux qui bâtissent avec moi les projets de demain : Audrey Steinberger bien sûr, Francisco Melo également, mais aussi mes futurs doctorants Tianjun Li et Felipe Aguilar à qui je souhaite une excellente réussite !

Enfin, j'exprime toute ma gratitude à Joël Chevrier, Matteo Ciccotti et Philippe Poncharal, qui ont accepté de rapporter ce mémoire, ainsi qu'à Arezky Boudaoud et Mark Rutland, qui complètent mon jury.

Et pour finir, un immense merci à ma femme et mes enfants, qui prennent avec le sourire tout le temps que je ne leur consacre pas quand je suis perdu dans mes rédactions, calculs, cogitations et autres rêveries de physicien...

Contents

Chapter 1

Introduction

A *mémoire d'habilitation à diriger les recherches* appears to be a very open concept: the only requirement of the manuscript is to situate the applicant's research in its area. It results in a vast variety of documents, ranging from article collections to deep reviews of a domain. My own choice lays somewhere in between these two options. I took this opportunity to conclude several unpublished works, and prepare a coherent manuscript of my contributions to my main current playground: nano-mechanics. Each chapter is independent of the others and can be read without referring to my publications.

The introduction first summarizes the path that led me from *aging of glassy materials*, my PhD subject, to micro and nanoscale mechanics. The next three chapters detail my current interests: I first present the high precision tool I have developed to conduct my researches, then two applications on the mechanical characterization of micro-cantilevers and the study of carbon nanotubes in interaction with a substrate. The conclusion finally underlines the promising perspectives of these works. The appendix presents some points of details of the manuscript.

I shall thus start this introduction by giving a short chronological outlook of my scientific path towards my current research interests[1], before quickly mentioning my implication in student's supervision and teaching.

[1] To preserve a global coherence to this manuscript, some of my minor research interests are not presented.

Aging of glassy systems

I realized my PhD thesis in the *Laboratoire de Physique - École Normale Supérieure de Lyon (ENS Lyon)*, under the supervision of Sergio Ciliberto, from 1997 to 2001. This work, entitled *Viellissement des systèmes vitreux et rapport fluctuation-dissipation*[2] [14], presents an experimental study of aging in glassy materials. These systems, when quenched from a high temperature equilibrium phase, are frozen in an unstable but very slowly evolving state. They are thus weakly out of equilibrium, and present as such a challenge to physical modeling [48]. The aim of my thesis was to test recent theoretical approaches of the subject: based on the analogy between spin glasses and structural glasses, these approaches extend the fluctuation-dissipation theorem (FDT) to these materials. It allows the definition of an effective temperature T_{eff} [35], measured with the fluctuation-dissipation ratio of such a system.

Part of my research has been first dedicated to the study of memory effects in a polymer (poly(methyl methacrylate) or PMMA) [8, 12]. Based on experiments on spin glasses[73], we demonstrated a strong analogy on fine effects in the behavior of these two different systems. Their common properties could be theoretically described in the frame of a hierarchical energy landscape. This analogy made PMMA a good candidate for a study of the fluctuation dissipation ratio based on the measurement of electric observables. It turned out not being possible to demonstrate any deviation of the FDT to corroborate the pertinency of the theoretical approach: T_{eff} was simply equal to the thermal bath temperature.

However, using a colloidal glass of Laponite, we demonstrated a clear deviation to the FDT on macroscopic electrical variables, in agreement with recent theories on aging [9]. In order to check the intrinsic character of this property, we proposed a second determination via a rheological study of this material. An ultra-sensitive rheometer has been set up [10], and the effective temperature was shown to depend on the observable [7]. This effect was not anticipated, but is now demonstrated in various models of aging [118, 132]. In continuation to this PhD work, we showed that a strong deviation to the FDT could also be observed in a polymeric glass (polycarbonate), and linked this behavior to the intermittency of the electric noise in the samples [24].

[2] Aging of glassy systems and fluctuation-dissipation ratio

Convection in Laponite

My post-doc took place in the Mechanics Department of the *University of Chile*, in Santiago. In the *Laboratorio de Estudios Avanzados en Fenomenos Non Lineales*, I collaborated with Rodrigo Hernandez on fluid mechanics experiments that where already running in his young lab [137]. My main topic was however to set up a new convection experiment, with the goal of studying the coupling between aging and flow in a thermal driven motion. Indeed, the recent theoretical framework for glassy systems suggests that aging should be altered by a small energy injection in the system. It could lead to a stationary weakly out of equilibrium state, with properties similar to the aging regime for the effective temperature. Such a situation would be far simpler to study as stationarity would allow time averages, much simpler to conduct than the ensemble averages needed to test aging systems.

A convection experiment could be used for such purpose, as the flow and associated shear are produced without any moving element, that would unavoidably perturb the measurement of fluctuations. We thus built a new setup to test this possibility, with the first aim to study the coupling between aging and convective flow. Although we couldn't reach a stationary state, this coupling proved to be rich. Convection is obviously altered by the rising viscosity of the material, with an initial turbulent heat transfer when the viscosity is low, and a transition to conductive heat transfer at long times, when the gel has formed and is too viscous to allow any flow. The opposite coupling can also be observed: the characteristic time scale of aging is found to depend on the roll pattern selected during the decay of convection. More rolls, leading to a higher shear stress, are delaying the gel formation [13].

Towards nanoscale phenomena

Back in the *ENS Lyon* where I was hired as a CNRS researcher in 2003, we were interested in studying aging of glassy systems at a smaller scale with respect to my former macroscopic experiments. Our inspiration came from the work of Israeloff and co-workers [131, 138], who used an atomic force microscope (AFM) as a local probe of dielectric fluctuation at nanometric scale. Getting closer to the pertinent spatial scale for glassy phenomenon could open a vast variety of experimental tests for corresponding theories. As the main goal was to precisely study fluctuations using an AFM, we decided to build our own device. Indeed, one of the outcome of my PhD work resulted in designing an outstanding differential interferometer [11], which should outperform most current AFM setups in terms of precision of the detection.

I therefore started to design my own AFM in 2004, backed by Pierdomenico Paolino, my first PhD student from 2005 to 2008. The adaptation of the design of our quadrature phase interferometer to the requirement of scanning force probes led to the exploration of a novel angle measurement technique [103], and various refinements in the initial interferometer. The first chapter of this manuscript describes in details the principle and experimental realization of our AFM, which features a very high resolution in force. A comparison of the benefits and drawbacks of our setup with respect to commercial devices as well as other high precision setups is conducted. The operation as a standard scanning microscope is demonstrated, and instrumental perspectives of this works are mentioned. Publications on this part have been delayed up to now to allow possible patenting. However, such a valorization didn't succeed (yet), and an instrumental article is about to be submitted [106].

During this setup phase, we performed a number of tests by measuring the deflexion of AFM cantilevers induced by thermal noise. This simple test to check the precision of our interferometer turned into a full axis of research, leading to most of the results of the PhD thesis of P. Paolino. Indeed, an unexpected phenomenon has been identified in some spectrums, namely a $1/f$ mechanical noise. We demonstrated that this behavior is the result of a viscoelastic dissipation process linked to the optional metallic coating of the cantilevers. Using the FDT and the Kramers-Kronig relations, we were able to characterize this damping mechanism and provide a quantitative phenomenological description of it [104]. The description of the noise spectrum around the resonance of the cantilever and at low frequencies for uncoated cantilevers, was as well not adequately understood within the classic simple harmonic oscillator approximation. This led us to test in depth Sader's dissipation model for viscous damping of the cantilever by the surrounding atmosphere, eventually leading us to a wide frequency validation of this approach, both on the noise measurement [6] and on the mechanical response function [104].

In collaboration with Bruno Tiribilli, from the *ISC-CNR*[3] in Firenze, we also began to measure maps of fluctuations on the cantilever surface. This procedure allows an easy access to the spatial shape of the normal modes of vibration. The analysis of the experimental data leads to the measurement of the mechanical properties of the cantilever (its spring constant) and of its constituting material (Young's and shear moduli) [107]. These results are presented in the second chapter of this manuscript, together with the analysis of the dissipation processes.

[3]Istituto dei Sistemi Complessi, Consiglio Nazionale delle Ricerche

These results on the fluctuations of AFM cantilevers received a warm welcome in the french AFM community, and triggered a new collaboration with the team of Jean-Pierre Aimé and Sophie Marsaudon, from the *CPMOH*[4] in Bordeaux. Indeed, they were already using thermal noise as a probe of the mechanics of carbon nanotubes (CNT) on a commercial AFM [23]. They saw in our superior resolution an adequate tool to test the behavior of single wall nanotubes, much softer and more difficult to tackle than multi-wall nanotubes. This new collaboration led to very nice experiments on the peeling mechanics of CNT, and the corresponding article has recently been submitted. To fully interpret the measurements, I also conducted a complete analytical study of the interaction between a nanotube and a substrate with a model of absorbed Elastica. Those results are described in the third and last chapter of this work.

As can be seen in this short introduction, the initial motivation to design our own AFM (local fluctuations in aging systems) is still a perspective of this work. Indeed, we crossed many puzzling and interesting phenomena during our instrumental quest, and began some promising collaborations on various topics in the micro and nano-mechanics area. The conclusion of this manuscript present the tracks we intend to follow in the next years...

Teaching

Before entering the core of this document, let me finally mention briefly my contribution to teaching in the ENS Lyon and my supervision activities.

I started teaching during my PhD in practical electronic training sessions in the Préparation à l'Agrégation de Sciences Physique of the ENS Lyon (master level, 64h a year for 3 years). I was not involved in formal teaching during my post-doc nor during my first years as a CNRS researcher, but recently signed up for a light annual implication (64h a year). I'm mainly involved in practical sessions again, though I should be starting a more formal course on instrumentation in 2011 and gave twice in 2009 a course focused on AFM abroad (*ECNU*[5], Shanghai, China and *USACH*[6], Santiago, Chile). Practical training corresponds to the way I like to interact with students: it really allows a bidirectional communication, and it's easier to lead the students to handle the problems and find appropriate solutions by themselves.

[4] Centre de Physique Moléculaire et Optique Herztienne
[5] East China Normal University
[6] Universidad de Santiago de Chile

Since my thesis, I've been involved in the supervision or co-supervision of various internships:

- Manuel Vial (fifth year engineer student in mechanics, Universidad de Chile, 12 month in 2002): Modulation of the wake of a flat plate.
- Mathieu Gibert (Maîtrise de physique ENS Lyon, 3 months in 2002): Convection in Laponite.
- Agnius Meškaukas (Erasmus Lithuanian student, Maîtrise de Physique Université Lyon 1, 3 months in 2004): Macroscopic dielectric measurements on hydration water.
- Marc Pannunzio (second year in DUT Mesure Physique Annecy, 3 months in 2006): Temperature regulation of the sample holder in the AFM setup.
- Julien Lopez (first year in Master Instrumentation, Université de Provence, 3 months in 2010): Imaging with quadrature phase interferometer AFM.

I've also been involved in the supervision of the PhD thesis of Kun Zhang (2005-2008) [150], a chinese student in joint supervision between the chemistry lab in the *ENS Lyon* and the *ECNU* in Shanghai. K. Zhang realized his thesis on mesoporous silica, and performed some macroscopic dielectric measurements of hydration water in these materials in the physics lab of the ENS Lyon. Back in China after his PhD, he is now an assistant professor in the *ECNU*.

Finally, I directed the PhD thesis of Pierdomenico Paolino [105], an italian student who had graduated from the *Università degli Studi di Napoli Federico II*. Between 2005 and 2008, P. Paolino took part in the design of the AFM setup, and conducted his research on the thermal noise and dissipation of micro-cantilevers. This manuscript owes a lot to his work, as will be illustrated in the next pages. He is now in a post-doc position the *PPMD, ESCPI*[7], in Paris.

[7]Laboratoire de Physico-chimie des Polymères et des Milieux Dispersés, École Supérieure de Chimie et Physique Industrielle

Chapter 2

Quadrature phase interferometer for AFM measurement

Abstract

In this first chapter, we present our innovative atomic force microscope (AFM). Its detection is based on a quadrature phase differential interferometer: we measure the optical path difference between a laser beam reflecting above the cantilever tip and a reference beam reflecting on the static base of the sensor. A design with very low environmental susceptibility and another allowing calibrated measurements on a wide spectral range are described. Both enable a very high resolution (down to $10^{-14}\,\mathrm{m}/\sqrt{\mathrm{Hz}}$*), illustrated by a thermal noise measurement on an AFM cantilever. A quick review shows that our precision is equaling or out-performing the best results reported in the literature, but for a much larger deflexion range, up to a few* μm.

The dual output of the interferometer implies a specific handling to interface common scanning probe microscope controllers. We present the analog circuitries we have designed to tackle static (contact mode) and dynamic (tapping mode) operations, with a thorough analysis of their characteristics. Imaging of a simple calibration sample, demonstrating the relevance of our approach, concludes this chapter.

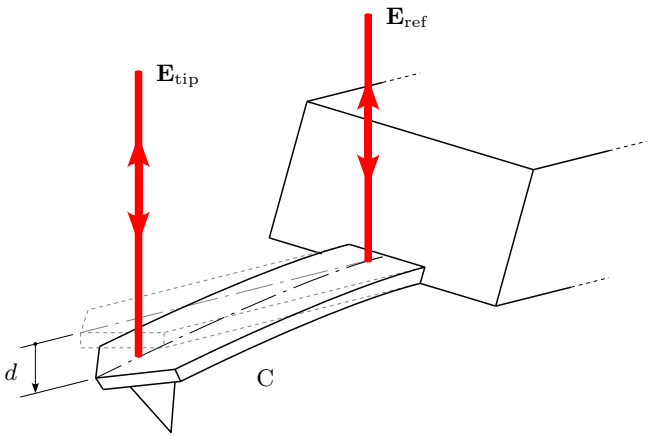

Figure 2.1 – *Measurement area: two parallel laser beams are focused on the cantilever C, the reference one is reflected by the static base (electric field* $\mathbf{E}_{\text{ref}}$*) and the sensing one by free end of the sensor (*$\mathbf{E}_{\text{tip}}$*). A deflexion d of the cantilever increases the optical path difference by* $\delta L = 2d$*, and we access this information through the interferences between the two beams.*

2.1 Introduction

Since its invention by Binnig, Quate and Gerber [19] more than 20 years ago, Atomic Force Microscopy (AFM) has turned into a mature technique widely spread in many domains (material sciences, biology, nanotechnology...). The detection scheme proposed in the original article was quickly dropped for handier optical methods. In the early ages of AFM, interferometric setups have been investigated by several authors as an option to measure the deflexion of the cantilever [42, 43, 98, 116, 117, 128]. The introduction of the optical lever technique [97] however, much simpler to implement and still very sensitive, limited those techniques to a few specialized application where optical access to the cantilever is restricted (cryogenic experiments for instance) or the ultimate precision of the measurement is important [66, 75, 93]. Our initial goal, aiming at studies of thermal fluctuations at nanoscale, belong to this last category: lowering the detection noise was the starting point of our instrumental development.

The main originality of our work is the use of quadrature phase interferometry in the context of AFM measurement. In 2002, we introduced this

technique, an instrumental perspective of my PhD thesis [14], under the appellation of *complex contrast interferometry* [11]. As our initial inspiration came from an AFM detection set-up [128], it was natural to apply our findings back to this area when we started to tackle nanoscale phenomena in 2004. Along the track toward our current setup, we explored a possible alternative with an interferometric measurement of angular deflexion [103]. It turned out not to be suited to the micrometer sized AFM cantilever, but still present another nice introduction to quadrature phase interferometry and its greatly extended measurement range.

We present in this chapter a few approaches we have explored in order to build a very sensitive detection scheme. They are all based on differential interferometry [43, 128]: two beams are produced in the measurement region of the AFM, the first being reflected on a static reference point of the sensor, the second on the free end of the cantilever (illustration in figure 2.1). The optical path difference between those two 2 beams is thus directly proportional to the deflexion d of the cantilever, and knowledge of the wavelength gives a precise calibration of the measurement. The analysis of the interfering beams is performed with a quadrature phase design, limiting as much as possible any slow drift problems, and allowing a virtually infinite defection range.

The chapter is organized as follows: A first section describes the various configurations of the sensing area, and the quadrature phase interferometric detection scheme common to our realizations. We then present thermal noise measurements as an illustration of the high sensitivity of our approach, before a comparison with other high resolution techniques. We describe in a second part how to process the output of our interferometer to use it in a common feedback loop used for imaging. A few preliminary images acquired with our set-up in static and dynamic modes are presented before concluding remarks.

2.2 Experimental setups

2.2.1 Interferometer: sensing area

Bi-calcite setup

We developed several strategies to produce the two beams in the measurement region of the AFM. The first one is inspired by reference [128], where a calcite prism is used. In our setup, as illustrated by Fig. 2.2, light passes

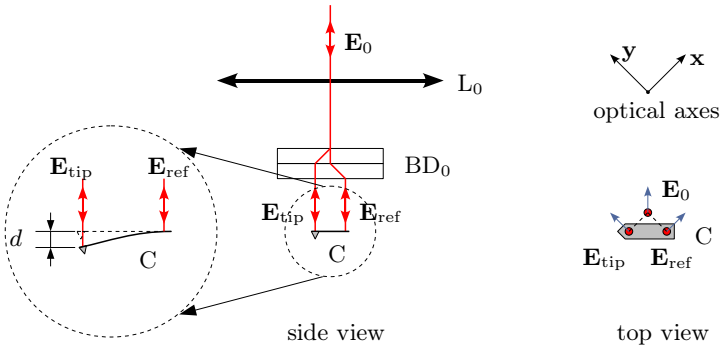

Figure 2.2 – *Measurement area: the incident beam (electric field* $\mathbf{E}_0$*) is focused on the cantilever C by the lens* L_0*. When passing through 2 calcite beam displacers* BD_0 *with orthogonal optical axes* $\mathbf{x}$ *and* $\mathbf{y}$*, light is split into 2 parallel beams, which are reflected by the base and free end of the sensor (fields* $\mathbf{E}_{\text{ref}}$ *and* $\mathbf{E}_{\text{tip}}$*). A deflexion* d *of the cantilever increases the optical path of the second beam by* $\delta L = 2d$*. On the top view, blue arrows show the direction of polarization of each beam.*

through two calcite beam displacers[1] after the focusing lens. The optical axis of the prisms are set perpendicular to each other, hence each polarization of the incident beam is once the ordinary and once the extraordinary ray. Both output beams are then equivalent : their optical path length is equal through the prisms. This setup has 2 advantages : not only the intrinsic optical path is the same on a flat cantilever (canceling the noise due to wavelength fluctuation in the light source), but so does the shift in the focus due to parallel plate. We usually associate two 1 mm thick calcite beam displacers. Each one produces a 100 μm shift of its extraordinary ray, so the total separation is approximatively 140 μm and adapted to cantilevers longer than this value. After reflection, the two beams are merged back together by the birefringent components and can be studied in the analysis area. The optical path difference δL is twice the deflexion d of the cantilever:

$$\delta L = 2d \tag{2.1}$$

[1]Calcite ($CaCO_3$ crystal) is a birefringent material. With appropriate cutting, a parallel plate of calcite spatially splits the two polarizations of light: the extraordinary ray exits the prism parallel to the ordinary ray, with a lateral displacement of one tenth the thickness of the plate (for normal incidence and visible wavelengths).

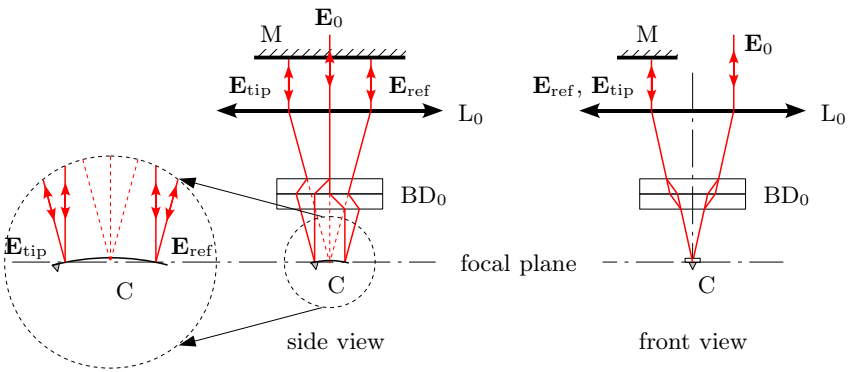

Figure 2.3 – *Double path technique: the incident ray (electric field* $\mathbf{E}_0$*) is focused on the sensor by lens* L_0*, and split in 2 (*$\mathbf{E}_{\text{ref}}$ *and* $\mathbf{E}_{\text{tip}}$*) by the calcite prisms (*BD_0*). After reflection on the curved surface of the cantilever, both beams exit the lens* L_0 *parallel but apart from each other. A perpendicular mirror send them back on their original paths so that they eventually perfectly overlap after a second reflection on the sensor. In practice, we use the 3 dimensions of space: the incident beam* E_0 *is slightly off axis on the lens as seen on the front view, so that its reflections* $\mathbf{E}_{\text{ref}}$ *and* $\mathbf{E}_{\text{tip}}$ *are shifted when exiting* L_0*. A single mirror* M *can be used for both. In this configuration, the optical path difference* δL *is 4 times the deflexion* d*.*

One of the problem we had to deal with is the intrinsic curvature of some cantilevers: when those are coated (to enhance reflectivity for instance), the metallic layer may produce internal stresses which lead to a static curvature of the sensor. Strategies to minimize this effect can be used (symmetric coating for example), but the tolerance of common detection systems to this defect is large since most only use a single reflection on the extremity of the cantilever. In our case, the two light beams must overlap in order to record interferences, and the bending of the reflective surface introduces a spatial separation of the 2 polarizations. For instance, a small 2° curvature (typical tolerance of commercially available sensors) translate into a 2 mm separation of the beams back to the 30 mm focusing length. The contrast in such a case can decrease to very small values, and depending on the cantilevers we sometime need to address this problem.

When a force acting on the tip is deflecting the cantilever, the previous considerations on the intrinsic curvature applies as well to the induced bending. However, a $\pm 2°$ angular range for a 300 μm long cantilever translates into a $\pm 7\,\mu$m deflexion range, much larger than the typical limit of AFM setups.

Double path setup

The simplest solution to deal with curvature limitation is to increase the diameter of the laser beams so that even with such a large separation they still overlap sufficiently to record sharp interferences. Indeed, we can reach a fair contrast on bended cantilevers using a 7 mm (instead of our common 2 mm) beam, though handling clear apertures for such a large diameter is difficult in our compact setup.

Another way to circumvent the problem is illustrated in Fig. 2.3. After reflection on the curved surface, the 2 beams corresponding to the 2 polarizations of the birefringent component are parallel when emerging the focusing lens. Indeed, both virtually come from the focal point but with different angles. We place a flat mirror perpendicular to the beams at this point: both are sent back on their original path, and overlap perfectly after a second reflection on the cantilever. This setup also doubles the sensitivity of the measurement: adding a second reflection on the sensor doubles the optical path dependance on the deflexion of the cantilever. This configuration can thus be interesting even for flat sensors. However, the tuning of the apparatus is much more complex (the focal distance for instance should be perfectly set as the double pass multiplies any error in this direction). Moreover, another problem can be stressed for uncoated cantilevers: their poorly reflecting surface being used twice, the intensity of the signal is lowered significantly and the overall gain in accuracy is much lower than 2.

Wollaston setup

A last strategy to create the two beams of the measurement area is illustrated in Fig. 2.4. It is very similar to that of ref. [43]. The initial beam (field $\mathbf{E}_0$) first crosses a Wollaston beam splitter, which produces 2 rays of orthogonal polarizations ($\mathbf{E}_{\text{ref}}$ and $\mathbf{E}_{\text{tip}}$), with an $\alpha = 2°$ separation angle. If the intersection point of these beams is placed at the focal point of the focusing lens L_0, the resulting beams are focused on the sensor, their optical axes being parallel. Translation of the Wollaston prism along the optical axis does not change the focalization points, but the angle of incidence of the beam on the sensor. It can thus be used to correct for a static curvature of the cantilever.

The distance between the 2 focalization points is given by the angular separation of the prism $\alpha = 2°$ and the focal length $f = 30\,\text{mm}$, that is 1 mm in our setup. This distance is always greater than the length of the cantilever, so the reference beam is reflected on the chip holding the sensor in this configuration. It is thus a little bit out of focus, the typical thickness

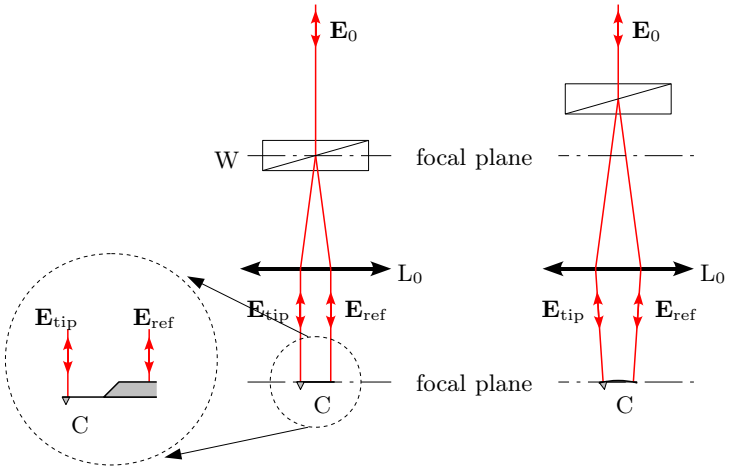

Figure 2.4 – *Wollaston measurement configuration: the incident ray ($\mathbf{E}_0$) is split in its 2 orthogonal polarizations ($\mathbf{E}_{\text{ref}}$ and $\mathbf{E}_{\text{tip}}$) by the Wollaston prism, then focused on the sensor by lens L_0. Tuning the position of birefringent component along the optical axis (right), any small static curvature of the cantilever can be compensated. After reflection, the beams are merged back together and can be analyzed: the optical path difference is twice the deflexion. Due to increased distance between the 2 beams (*1 mm *in our configuration), the reference ($\mathbf{E}_{\text{ref}}$) is taken on the chip holding the cantilever.*

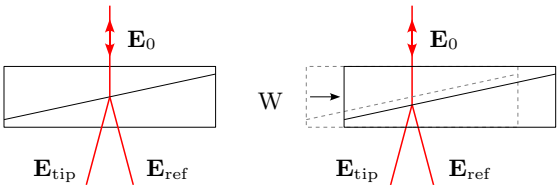

Figure 2.5 – *Tuning the initial optical path difference : a translation of the Wollaston prism W along the separation axis modifies the optical path of the two polarized beam ($\mathbf{E}_{\text{ref}}$ and $\mathbf{E}_{\text{tip}}$) inside the birefringent material. The small shift of the splitting point of the beam has a negligible effect in our setup.*

of the chip being 0.4 mm. Anyway, the reflecting surface is very large and no light is lost, and the small divergence of the 2 beams we will eventually analyze decreases only slightly the contrast of the interferences.

A benefit of this configuration is the possibility to tune the initial path difference between the two beams [43]. Indeed, a translation of the Wollaston prism along the axis of separation changes differently the optical path of the ordinary and extraordinary rays in the birefringent element (see figure 2.5). For a the lateral displacement δx of our prism, we measure this dependence to be $\delta L/\lambda = \delta x/(10\,\mu\text{m})$, where $\lambda = 633\,\text{nm}$ is the wavelength of the He-Ne laser we are using.

Comparison of setups

The three configurations of the measurement area, illustrated in Figs. 2.2 to 2.4, have their own advantages and drawbacks, and we chose for every experiment the best compromise for our specific needs. The first setup (Fig. 2.2) is for example very stable with respect to external disturbances, the 2 beams sharing almost the same path except for the very last millimeters before the cantilever, but it is restricted to flat rectangular cantilevers longer (but ideally not too much) than $140\,\mu$m. The double path arrangement (Fig. 2.3) can be more sensitive and adapted to curved sensors, but is more vulnerable to external vibrations and more complex to tune. The Wollaston configuration (Fig. 2.4) is easy to align and adapted to cantilever of any shape and length (V shaped for instance), but it is also more affected by environmental perturbations and its contrast is not as sharp.

A further comparison of the Wollaston and Bi-calcite configurations, based on thermal noise measurement, is conducted in part 2.2.3

2.2.2 Interferometer: analysis area

The three setups for the measurement area share the same principle: the incident light is split in 2 with a birefringent component, and each ray is focused on the sensor. After reflection, the beams are merged into a single one and the optical path difference between its two polarizations is a linear function of the deflexion of the cantilever. The analyzing area is thus the same for all the measurement configurations. It is based the quadrature phase technique we have developed [11, 103], as illustrated on Fig. 2.6: the light is separated in two equivalent arms (indexed with subscript $n = 1, 2$) with a non polarizing cube beam splitter, then focused on the photodetectors by lenses L_n (focal length 25 mm). To record interferences, the initial

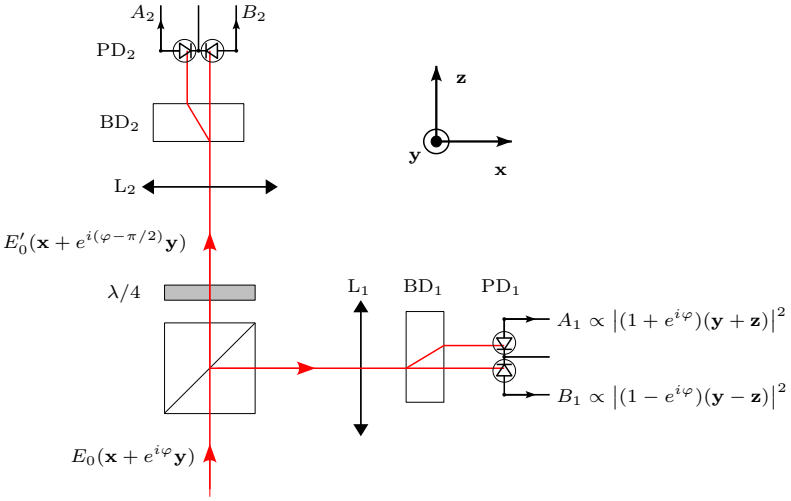

Figure 2.6 – *Experimental setup: analysis area. The light coming from the measurement area is split into two arms, indexed with subscript $n = 1, 2$. In each one, a* 5 mm *calcite prism (beam displacers BD_n) oriented at* 45° *with respect to the measurement birefringent component (BD_0 or W) projects the polarizations to have them interfere. The 2 beams emerging from BD_n are focused by a plano convex lens (L_n, $f = 25$mm) on the 2 segments of a 2 quadrant photodiode PD_n to record their intensities A_n, B_n. Those are used to reconstruct φ and thus measure the deflexion d of the cantilever. In the second analyzing arm ($n = 2$), a quarter wave plate ($\lambda/4$) is added in order to add $\psi_2 = -\pi/2$ to the phase shift φ.*

polarizations are projected by calcite beam displacers (BD_n, 5 mm thick) whose axes are at 45° with respect to the optical axes of the measurement birefringent component (BD_0 or W). The two beams emerging from each calcite prism are 0.5 mm distant, they are collected on the two segments of a 2 quadrant photodiode (*UDT* Spot-2DMI). The only difference between the two arms is the addition of a quarter-wave plate in the second arm, tuned to subtract $\pi/2$ to the phase shift between the 2 polarizations.

For the following computation, we will use the configuration of Fig. 2.2, but it can be easily extended to the other setups with minor changes. Let us call $\mathbf{x}$ and $\mathbf{y}$ the unity vectors along the optical axes of the calcites BD_0, and $\mathbf{E}_0 = E_0(\mathbf{x} + \mathbf{y})$ the electric field of the incident beam, tuned to be linearly polarized at 45° with respect to $\mathbf{x}$ and $\mathbf{y}$. The total field of the

beams after reflection and recombination is $\mathbf{E}_{\text{ref}} + \mathbf{E}_{\text{tip}} = E_0(\mathbf{x} + e^{i\varphi}\mathbf{y})$, with φ the phase shift between the 2 polarizations. Since the optical path difference δL is twice the deflexion d of the cantilever (equation 2.1), φ is simply

$$\varphi = \frac{4\pi}{\lambda} d \tag{2.2}$$

where $\lambda = 633\,\text{nm}$ is the wavelength of the He-Ne laser we use. The optical axes of the analyzing calcite prisms BD_n are oriented at 45° with respect to BD_0 (along $\mathbf{x}+\mathbf{y}$ and $\mathbf{x}-\mathbf{y}$ for BD_2 for example), hence the intensities of the projected beams on the 2 quadrants of the photodiodes are easily computed as

$$\begin{aligned} A_n &= \frac{I_0}{4}(1 + \cos(\varphi + \psi_n)) \\ B_n &= \frac{I_0}{4}(1 - \cos(\varphi + \psi_n)) \end{aligned} \tag{2.3}$$

where subscript n stand for the analyzing arm ($n = 1, 2$), I_0 is the total intensity corresponding to the incident light beam[2], and $\psi_1 = 0$ (first arm, without quarter wave plate) or $\psi_2 = -\pi/2$ (second arm, with quarter wave plate). Using home made low noise analog conditioning electronics or post-acquisition signal processing, we can measure for each arm the contrast function of these two signals:

$$C_n = \frac{A_n - B_n}{A_n + B_n} = \cos(\varphi + \psi_n) \tag{2.4}$$

This way, we get rid of fluctuations of laser intensity, and have a direct measurement of the cosine of the total phase shift for each arm, $\varphi + \psi_n$.

Let us rewrite eq. 2.4 as:

$$C = C_1 + i\,C_2 = \cos(\varphi) + i\sin(\varphi) = e^{i\varphi} \tag{2.5}$$

Under this formulation, the advantage of using two analyzing arms instead of one is obvious : it allows one to have a complete determination of φ (modulo 2π). In the (C_1, C_2) plane, a measurement will lay on the unit circle, its polar angle being the optical phase shift φ. The sensitivity to detect small variations in the deflexion of the cantilever appears this way to be

[2] I_0 is the electrical intensity defined by $I_0 = SP$, where P is the incident beam power (in W) and S is the responsivity of the photodiodes (in A/W). The 1/4 factor in the equations accounts for the beam-splitting process (2 final beams in both analyzing arms).

independent of the static deflexion and the intrinsic optical path difference:

$$\left|\frac{\mathrm{d}C}{\mathrm{d}d}\right| = \frac{4\pi}{\lambda} \tag{2.6}$$

No tuning of the zero is necessary. The use of crossed polarizations for the two interfering beams is a key point of this method, since it allows a post processing of the phase difference (with the quarter-wave plate) to produce the quadrature phase signals.

Eventually, to measure the deflexion d of the cantilever, all what we need to do is to acquire the two contrast C_1 and C_2, and reconstruct d with standard digital data processing tools: $\varphi = 4\pi d/\lambda$ can be computed as

$$\varphi = \arg(C) = \arctan(C_2/C_1) \tag{2.7}$$

Unwrapping of the phase φ to avoid discontinuities every 2π can be necessary for large amplitudes of deflexion. This can easily be performed as long as the sampling frequency f_s is sufficient: the distance between successive points should be smaller than π, which translates of into $f_s > 4\dot{d}/\lambda$ (where $\dot{d}$ is the time derivative of d).

In the experimental realization, the unavoidable imperfections of optical components and of their alignment will lead the complex contrast to lay in reality on a tilted ellipse with axes smaller than one, instead of the unit circle: we can generically write

$$\widetilde{C} = \widetilde{C}_1 + i\,\widetilde{C}_2 = \mathcal{C}_1\cos(\varphi) + c_1 + i\,(\mathcal{C}_2\sin(\varphi+\psi) + c_2) \tag{2.8}$$

where over tilde contrasts represent the measured values (by opposition to the ideal values of equation 2.5), and $\mathcal{C}_n < 1$ are the contrast amplitudes in each arm, c_n the contrast offsets, and ψ a residual mismatch to perfect quadrature [11]. These 5 parameters can easily be extracted from a calibration of the interferometer: we excite a small amplitude oscillation of the free cantilever with a piezo, and get the parameters from a generic fit of the recorded ellipse (see figure 2.7). In the Wollaston configuration, we can also produce the ellipse with a lateral driving of the birefringent prism, allowing us to calibrate the system with no oscillation of the cantilever. The results of these 2 methods in this case are in perfect agreement. Once this elliptic fit done, raw measurements ($\widetilde{C}$) can easily be post processed and projected on the unit circle (C), to extract the actual deflexion [11].

Let us summarize the main points of our interferometric setup. The input laser light is split into a reference beam, directed on the base of the cantilever, and a sensing beam, focused on top of the tip of the sensor. The

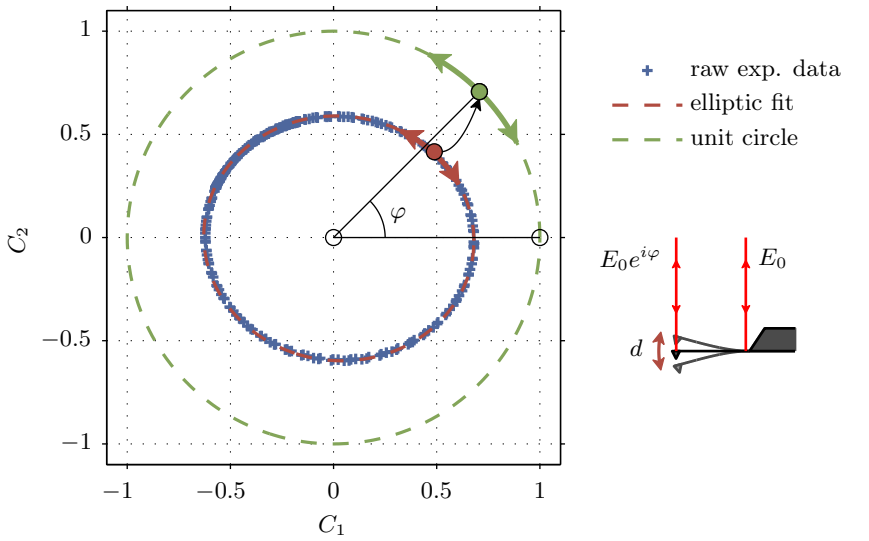

Figure 2.7 – *Calibration of the complex contrast: we drive the cantilever close to its first resonance with an amplitude of deflexion d of the order of the laser wavelength λ. The experimental data follow an ellipse in the $(\widetilde{C}_1, \widetilde{C}_2)$ plane. After a simple fit of this ellipse with equation 2.8, it is straightforward to project the measurement point on the unit circle, and identify its polar angle with the optical phase shift φ. Equation 2.2 eventually leads to a calibrated measurement of deflexion d.*

phase shift φ is a linear function of the deflexion d (equation 2.2). After reflection, the two rays of crossed polarization are recombined and processed with a quadrature phase technique: two output signals $\widetilde{C}_1$ and $\widetilde{C}_2$ are produced, with $\widetilde{C}_1 \sim \cos\varphi$, and $\widetilde{C}_2 \sim \sin\varphi$ (equation 2.8). Post-processing of these signals leads to a precise, calibrated and virtually unbounded value of the deflexion d. Figure 2.8 illustrate our experimental realization by a photograph of the setup with superposed optical scheme.

2.2.3 Performances of our experimental realization

In this section, we will present the main performances in terms of stability and precision of the two main configurations (bi-calcite and Wollaston) presented in section 2.2. The double-path technique, due to its complexity of

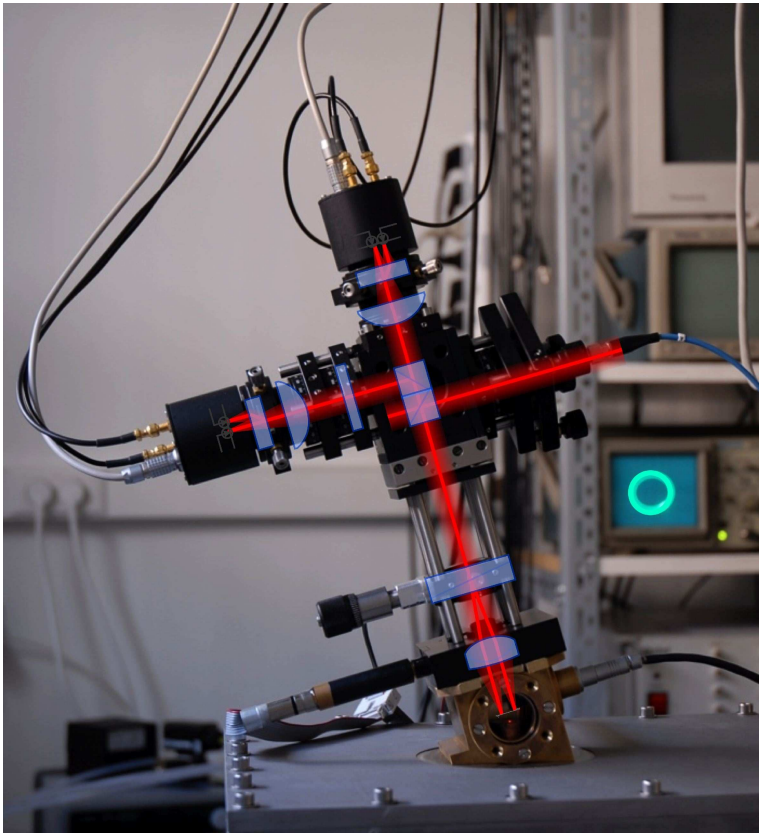

Figure 2.8 – *Photograph of our experimental realization of the quadrature phase interferometer for AFM measurement with superposed optical scheme. The laser light is fed into the setup with an optical fiber (blue cord on the right of the image). In the background, an oscilloscope in XY mode displays the elliptic trace of the outputs during the procedure of calibration of the complex contrast.*

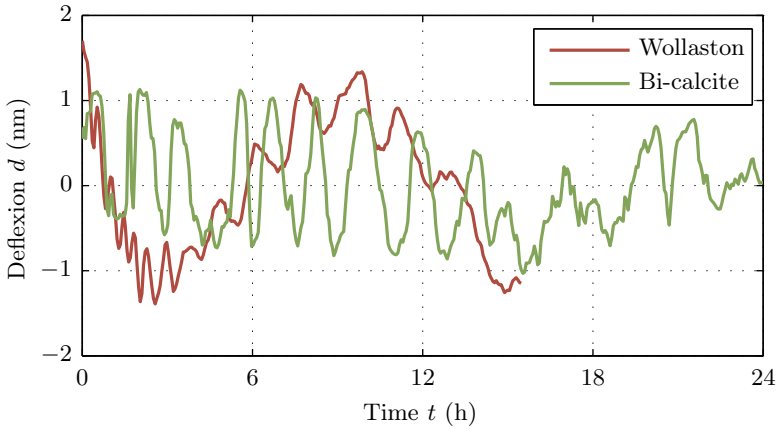

Figure 2.9 – *Long term stability of the interferometric measurement: after calibration, an acquisition of the deflexion of a cantilever at rest is performed. For both the bi-calcite and the Wollaston configuration, the drift after several hours is at most* 3 nm.

tuning, has mainly been used to deal with curved cantilevers, and was not systematically characterized.

Long term stability

We present in figure 2.9 the evolution over several hours of the deflexion measured on a cantilever at rest, far from any sample. Slow environmental changes (temperature drift...) have little influence on the measurement: the deflexion is stable within a ± 1.5 nm fluctuation range, for both sensing strategies. This long term stability is excellent: for most applications, there is no need for frequent calibrations of the interferometer.

Thermal noise measurement

This section on the thermal noise of a cantilever is just a quick illustration of the high precision of our interferometric measurement of the deflexion, an extensive study on this topic is presented in chapter 3.

We use our setup to record the equilibrium fluctuations of a cantilever at rest, far from any sample. Thermal noise acts as a white noise random forcing, exciting all resonant modes of the microscopic mechanical beam:

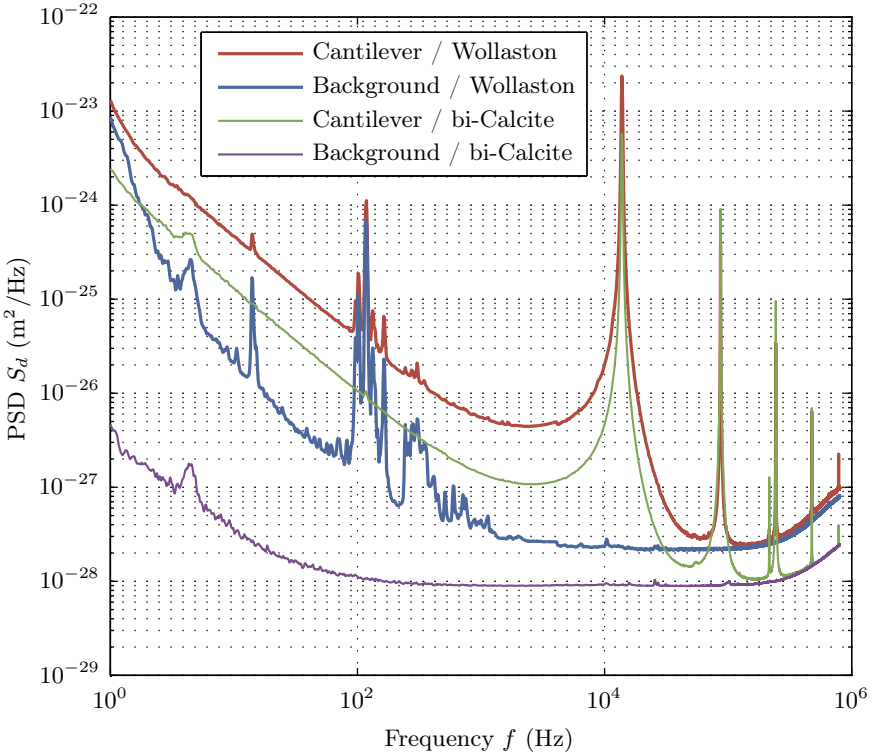

Figure 2.10 – *Power spectrum density of deflexion measured in the Wollaston and bi-calcite configurations of a golden coated cantilever and on a rigid mirror (background noise). The raw data plotted here demonstrate the high precision of the interferometer: the background noise is as small as* $10^{-14}\,\mathrm{m}/\sqrt{\mathrm{Hz}}$ *for the bi-calcite set-up, on a wide frequency range. This is only* 20 % *higher than the unavoidable shot noise due to the photodiodes, and a small increase can be noticed at low and high frequencies due to higher conditioning electronics noise. In the Wollaston configuration, the base line noise is slightly higher at* $1.4 \times 10^{-14}\,\mathrm{m}/\sqrt{\mathrm{Hz}}$ *(again within* 20 % *of the shot noise limit), and degrades faster at low frequency: the setup is more sensitive to external perturbations as the reference and sensing laser beams are separated on a longer distance. In both configuration however, the thermal noise of the cantilever is clearly visible, with 5 perfectly defined flexural modes in this* 1 MHz *frequency range. The* $1/f$ *like behavior at low frequency, 2 orders of magnitude larger than the background noise, is studied in part 3.3.2.*

as shown on figure 2.10, the first 5 structural resonances are visible on the Power Spectrum Density (PSD) S_d in the 1 MHz range in frequency explored here. The data was acquired on a gold coated cantilever *Budget Sensors* Cont-GB (data sheet in appendix D.1) in air far from any sample. The cleanness of the curves demonstrates the sensitivity of the detection method, down to low frequencies. The instrument noise for the bi-calcite configuration, recorded by replacing the cantilever by a rigid mirror while keeping intensities on the photodiodes unchanged, decreases from $10^{-13}\,\mathrm{m}/\sqrt{\mathrm{Hz}}$ at 1 Hz down to $10^{-14}\,\mathrm{m}/\sqrt{\mathrm{Hz}}$ for frequencies f above 100 Hz, before raising gently again above 300 kHz. The main contribution to this floor noise is the unavoidable shot noise due to the photodiodes. We can estimate this contribution from the light intensities recorded at each photodetector: the performance is close to optimal conditions, only 20% above the shot noise limit for a laser power around $100\,\mu$W per sensing beam. On top of this white noise, the conditioning electronic noise is added (raising the noise at low and high frequency), and some environmental vibration can be seen (bump in the 10 Hz region).

The Wollaston configuration is more sensitive to external perturbations, especially at low frequency where its background noise is not as low. Many more vibrations peaks can be noted below 1 kHz. However, the mechanical noise intrinsic to the cantilever is still almost everywhere much higher than this detection limit at low frequency. For f in the $1\,\mathrm{kHz} - 300\,\mathrm{kHz}$ range, the background fluctuations reach again the shot noise limit, at $1.4 \times 10^{-14}\,\mathrm{m}/\sqrt{\mathrm{Hz}}$.

We note a discrepancy between the two measurement methods: the amplitude of the spectrums are not equal, with a factor depending on the mode considered. Indeed, as the cantilever is $450\,\mu$m long, we have to correct the output of the bi-calcite configuration: the spots are only $140\,\mu$m distant, so the actual deflexion is not equal to the interferometer output. The multiplicative factor to consider is mode dependent: as illustrated on figure 2.11, the coefficient is about 2 for the first mode, but can be smaller than one for higher order modes. We therefore correct the power spectrums of figure 2.10 for the bi-calcite configuration considering those factors (we switch between coefficient at half way between resonance frequencies). The final curve presented in figure 2.12 matches closely the measurement with the Wollaston setup, except when the fluctuations are close to the background noise (between resonances).

This mode dependent correction is anyway a complex procedure, which has to be tuned for every specific geometry. The background noise, in absolute better for bi-calcite configuration, can eventually get worse than that

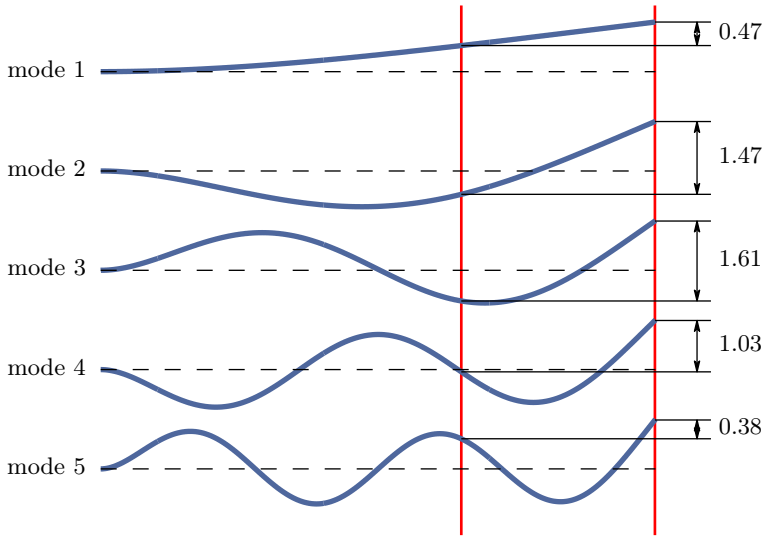

Figure 2.11 – *In the bi-calcite configuration, the distance between the two laser spots is smaller than the length of the cantilever, thus the measured deflexion does not correspond to the actual value. The correction to consider is mode dependent: according to the position of the spots with respect to the nodes and antinodes of the spatial shape, it can be smaller or larger than one. Using an Euler Bernoulli model for the mechanical beam, we estimate the coefficient noted on the figure for the measured amplitude normalized to the deflexion of the free end for the 5 first modes.*

of the Wollaston configuration. Moreover, in between resonances, where the noise of the modes are of equivalent amplitude, further assumptions would be required to extract information from the measured fluctuation. Finally, the study of torsional modes is difficult with this setup as it requires a perfect alignment between the cantilever and the two laser spots. On figure 2.10 for instance, a peak of small amplitude can be noticed just before the third flexural mode resonance, only in the bi-calcite configuration: we couldn't perfectly center both sensing beams, and the first torsional mode is visible on the spectrum. Unless the cantilever length is close to the laser spots distance, the bi-calcite configuration is thus not adapted to the simultaneous study of several modes, nor to the absolute characterization of the cantilever noise. However, its excellent performance at low frequency is ideal to study the low frequency behavior of thermal fluctuations, and this

configuration will be preferred over the Wollaston one in the study of the viscoelasticity of cantilever presented in part 3.3.2.

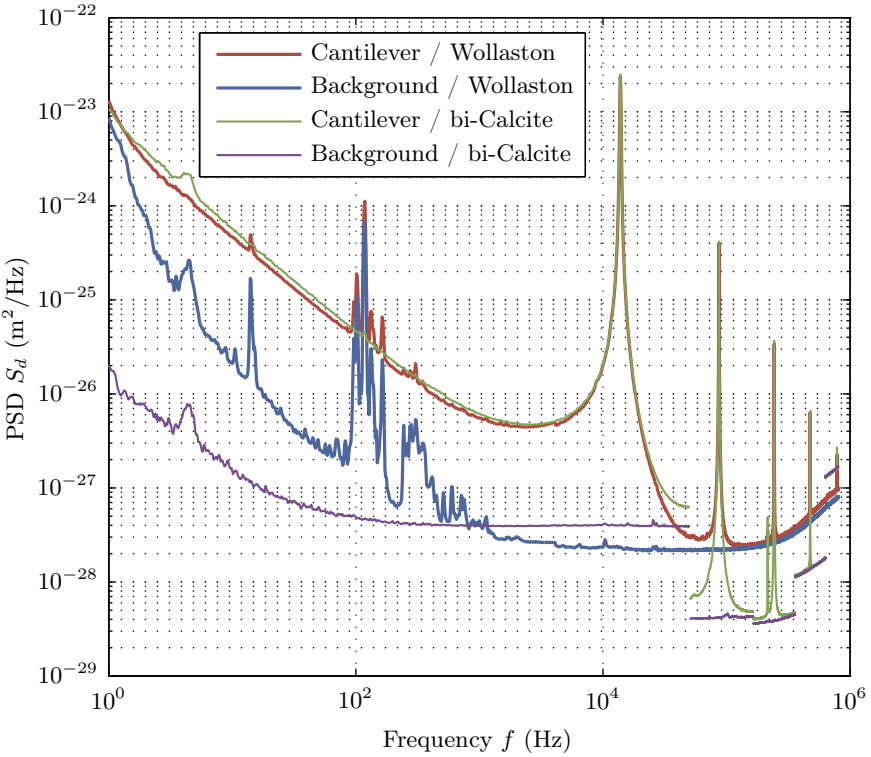

Figure 2.12 – *Power spectrum density of deflexion measured in the Wollaston and bi-calcite configurations of a golden coated cantilever and on a rigid mirror (background noise). The spectrums measured in the bi-calcite configuration have been corrected to take into account the real position of the laser beams on the cantilever: since the cantilever is longer (450 μm) than the beam separation (140 μm), the reference point is not static. A mode dependent correction has been considered.*

2.2.4 Comparison with other devices

To conclude this section on our deflexion measurement setup, we compare its performance to that of commercial AFMs and other interferometric detection systems in the literature.

Most commercial AFMs today use an optical lever configuration [97]: a laser beam is focused on the cantilever, and the reflected light is collected on a 4 quadrants photodiode. A deflexion changes the position of the spot on the detector, thus the relative intensities of each segment proportionally to the slope of the illuminated part of the cantilever. This method is very simple to implement, and achieves a high precision: using dedicated cantilever geometries, it can even be as sensitive as an interferometric approach [62, 112]. However, for common geometries and commercially available cantilevers, the shot-noise limit of the optical lever technique is around ten time higher than our interferometric approach[3]: the background noise for the cantilever of figure 2.10 is at best $10^{-13}\,\mathrm{m}/\sqrt{\mathrm{Hz}}$. Moreover, the electronic and environmental noise are most of the time not as low as in our experiment, making low frequency measurements of thermal noise impossible with commercial devices. Lastly, a calibration step is required to convert the output of the photosensor into the actual deflexion of the cantilever: during a contact with a hard surface, the sample is moved vertically of a known distance, leading to the calibration constant. This step can be undesirable, to prevent any alteration of the tip during the hard contact for instance, and can be avoided with interferometric approaches. Moreover, this calibration procedure is accurate only for static deflexions, and the correction to consider depends non trivially on the mode considered at higher frequency [126].

We present in figure 2.13 a comparison of noise measurements with our setup (Wollaston configuration) and three commercial devices, on the same cantilever. A mode dependent multiplicative factor has been applied to the three spectrums acquired on commercial apparatuses, so that the amplitude of each resonance matches our calibrated measurement. The background noise of the three detection systems is dominant everywhere except at the resonances, and is at least 10 time worse (in $\mathrm{m}/\sqrt{\mathrm{Hz}}$ units) than in our interferometer, though the laser spot intensity is 10 times higher (around 1.1 mW in the 3 devices). Low frequency information on the mechanical thermal noise is not accessible:

[3] A notable exception is the set-up developed by Fukuma [54], who reached $5 \times 10^{-15}\,\mathrm{m}/\sqrt{\mathrm{Hz}}$ accuracy thanks to a careful overall design and a high 2 mW laser power.

- for the 2 Veeco devices, the electronic $1/f$ noise is dominant. The spectrum below 1 kHz is not accessible in the Nanoscope V due to software limitation. It was acquired using a Signal Access Module and independent acquisition cards on the Nanoscope IIIa.

- for the Asylum AFM, the low frequency noise is processed with a high pass filter, cutting the electronic $1/f$ noise but also any physical information about the system.

Let us stress anyway that the high sensitivity of 4 quadrant detectors is more than sufficient for imaging purposes. Its simplicity drove its election in most commercial systems. With the applications we present in this work, we will demonstrate anyway that the higher resolution and intrinsic calibration of our approach leads to original results.

Before the optical lever technique became dominant, a bloom of various approaches to read the cantilever deflexion followed the invention of the AFM by Binnig, Quate and Gerber in 1986 [19]. Interferometric methods were and still are the most sensitive methods, and exist nowadays as home built systems in a few laboratories. We will focus only on homodyne interferometers, since heterodyne setups are limited to dynamic operation and cannot access the static information which is of interest for the applications we present in this work. They can be categorized into two main groups:

- *Fabry-Pérot like interferometers.* In its most simple realization, the fiber interferometer, the resonant cavity is composed by the cantilever and the cleaved end of an optical fiber [116, 117]. The finesse of the cavity in this case is close to 1, as multiple reflections are killed by the low reflectivity of the fiber end and the divergence of the optical beam reflected by the cantilever. The output of the interferometer is then a sinusoidal function of the deflexion. Background noise down to $5 \times 10^{-14}\,\mathrm{m}/\sqrt{\mathrm{Hz}}$ have been reported [117] for this arrangement for incident light power around $100\,\mu\mathrm{W}$. To increase the finesse of the interferometer and thus its sensitivity, a reflective coating covering the fiber end has been proposed in references [93, 98, 101, 108]. A drawback of this design is the coupling between deflexion and light intensity in the cavity: photothermal and radiation pressure bending the cantilever are function of the light intensity which is linked to the deflexion. This can result into a self oscillating as well as a self cooling cantilever [95, 139], eventually complicating the data analysis. Hoogenboom and coworkers [65, 66], in a convergent geometry where the cantilever is at the focal point of a concave semi-reflecting lens,

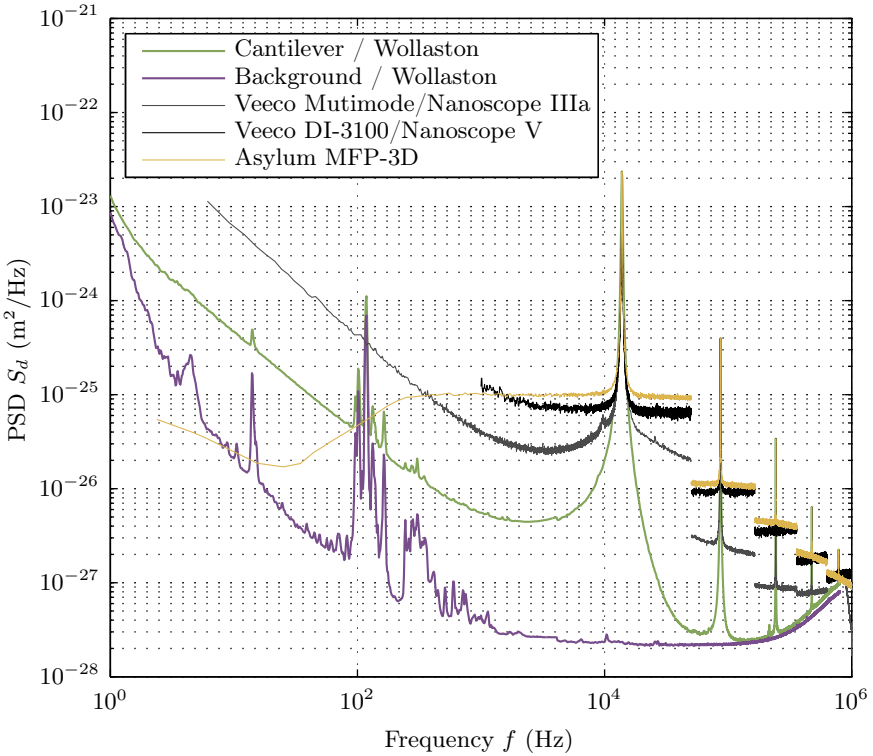

Figure 2.13 – *Power spectrum density of deflexion measured in the Wollaston configuration and on 3 commercial devices. The same golden coated cantilever is used, except for the background noise of our setup which is acquired on a rigid mirror. The spectrums measured with commercial devices have been corrected to convert the angular measurement into a deflexion measurement. The correction is mode dependent, and tuned so that the amplitude of each resonance matches the calibrated spectrum.*

reached a finesse of 20. The output is in this case highly non linear, but for deflexion much smaller than the wavelength around the optimum of sensitivity, a background noise of $10^{-15}\,\mathrm{m}/\sqrt{\mathrm{Hz}}$ at high frequency (1 MHz and higher) can be reached for an incident light power of 1 mW. The noise at lower frequencies (less than 250 kHz) is however at best comparable to the performance of our system.

- *Differential interferometers.* These interferometers [1, 37, 43, 59, 128] have inspired this work. They use birefringent elements to split an incident light into two beams of crossed polarization which are both focused on the cantilever (or on a reference mirror strongly connected to it [37, 59]). Those systems have shot noise limited performances, and as such are as good as our realization: the baseline for the background noise reached in these experiments is around $10^{-14}\,\mathrm{m}/\sqrt{\mathrm{Hz}}$ for comparable incident light power.

Our experimental device, described in details in this chapter, thus reaches one of the best precision one can hope for only $100\,\mu$W incident light power of the cantilever. It presents moreover a significant advantage over every other configuration: the deflexion range for which this performance is available is very wide, up to a few μm. The convergent Fabry-Pérot configuration [65] for example, reaching the best absolute performance, implies a cavity finesse of 20, limiting the linear deflexion range to 20 nm at best. With other interferometer design, the typical range available is smaller than $\lambda/4$, thus around 100 nm. High precision optical lever set-ups [54] also present a limitation around 100 nm for their linear deflexion range (and require an additional calibration step, as already mentioned).

To conclude this section, let us summarize the main properties of our interferometric measurement of AFM cantilever deflexion:

- A very high resolution, down to $10^{-14}\,\mathrm{m}/\sqrt{\mathrm{Hz}}$, on a very wide spectral range, equaling or out-performing the best results reported in the literature for equivalent light power, especially at low frequency.

- A huge deflexion range, up to several μm, much larger than any other high precision systems.

- An intrinsically calibrated measurement, thanks to the interferometric approach.

- A very stable sensor, with less than 3 nm drift over 24 h.

2.3 Imaging with quadrature phase detection

The quadrature phase interferometric approach described in the previous section is fine as long as we are interested in the deflexion itself, to measure force-distance curves for instance. The situation can be far more tricky if we want to include the deflexion signal in an analog retroaction loop to perform basic AFM tasks like imaging in constant force (contact) mode or in dynamic (tapping) mode. Indeed, we have two signals $\widetilde{C}_n$ $(n = 1, 2)$ whose sensitivity $\mathrm{d}\widetilde{C}_n/\mathrm{d}d$ can be very different according to the position of the working point on the unit circle. Choosing only one of these two as the retroaction signal would imply an optical tuning of the zero (to ensure best sensitivity) and limited drift tolerance of this working point. We present here a strategy to produce an optimal analog deflexion signal without tuning one of the contrasts to zero.

The basic idea is to use equation 2.5 for small variations of φ around φ_0: writing $\varphi = \varphi_0 + \delta\varphi$ and $C_n = C_n^0 + \delta C_n$, we have

$$\delta C_1 + i\,\delta C_2 = i\delta\varphi e^{i\varphi_0} = i\delta\varphi(C_1^0 + i\,C_2^0) \tag{2.9}$$

hence, since in this ideal case $|C_1^0 + i\,C_2^0| = |e^{i\varphi_0}| = 1$,

$$\begin{aligned} \delta\varphi &= C_1^0\delta C_2 - C_2^0\delta C_1 & (2.10)\\ &= C_1^0 C_2 - C_2^0 C_1 & (2.11) \end{aligned}$$

This last equation can be implemented with analog electronics, as it only implies basic operations (multiplications and subtraction). In the experimental realization, we have to take care about the various imperfections quantified with parameters $\mathcal{C}_n$, c_n and ψ in equation 2.8. The first step is to adjust the small offsets c_n to zero, using simple offsetting analog electronics: with a realtime fitting algorithm of the ellipse during calibration, we take care to tune the optics as centered as possible, and eventually correct the slight remaining error with the electronics. The residual offset can be made smaller than 1 %. Eq. 2.8 then reduces to

$$\widetilde{C} = \widetilde{C}_1 + i\,\widetilde{C}_2 = \mathcal{C}_1\cos(\varphi) + i\mathcal{C}_2\sin(\varphi + \psi) \tag{2.12}$$

Although very similar, the next steps are slightly different if we use a static (DC) or dynamic (AC) mode. We will first present the approach preserving the DC information, then describe the strategy to deal with AC signals.

2.3.1 Contact mode

In contact mode, we need to define the reference position of the cantilever, for example when the deflexion corresponds to the constant force we choose for imaging. We first perform a force curve, choose the working point and set the sample position to reach this deflexion set-point. We then trigger a numeric "sample and hold" device that freezes the contrasts to their values $\widetilde{C}_n^0$ in this reference state. Inspired by equation 2.11, we can further compute the following quantity with analog electronics:

$$U_{DC} = \widetilde{C}_1^0 \widetilde{C}_2 - \widetilde{C}_1 \widetilde{C}_2^0 \tag{2.13}$$

Using the expressions of $\widetilde{C}_n$ (eq. 2.12) and simple trigonometric calculations, it is straightforward to show that

$$U_{DC} = \mathcal{C}_1 \mathcal{C}_2 \cos(\psi) \sin(\varphi - \varphi_0) \tag{2.14}$$

where φ_0 is the optical phase corresponding to the reference point $\widetilde{C}_n^0$. The signal U_{DC} is finally a simple sine function of the deflexion of the cantilever, and can directly be used in an analog retroaction loop to image a sample in contact mode. As long as the deflexion of the cantilever (with respect to the set-point) is small compared to the wavelength, the sensitivity is always optimal with this technique, whatever the value of φ_0.

The analog circuitry implementing equation 2.13 in our experiment has been realized by F. Ropars from the electronic shop of our laboratory, it is based mainly on component AD734 for division (calculation of contrasts $\widetilde{C}_n$) and multiplications (calculation of U_{DC}). We present in figure 2.14 U_{DC} measured as a function of the input deflexion, for various values of φ_0. Although the complete curves are a bit different with respect to their maxima and minima, the central part is independent on the working point: the slope is 34 mV/nm with only a 6% variation when φ_0 explores the whole circle. U_{DC} is thus a good signal to feed the retroaction loop in contact mode, as long as the deflexion is kept close to the reference value.

The main advantage of this electronic tuning of the zero, compared to an optical tuning, is obviously its simplicity: a simple reset of the sample and hold output, remotely triggered. Moreover, except for the Wollaston configuration [43], optical tuning would require additional optical components and actuators, adding complexity and potential noise/drift sources to the setup.

It should be noted however that this strategy does not prevent an important issue of AFM imaging in contact with interferometric sensors: fringe

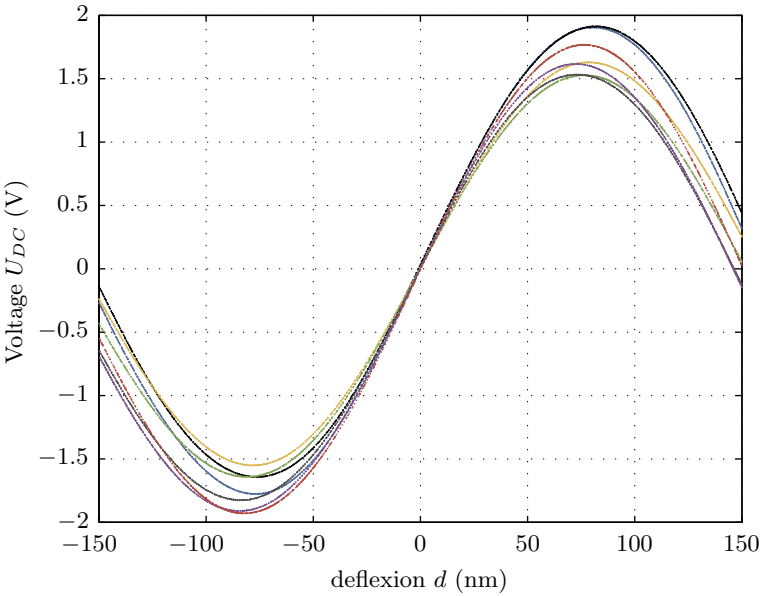

Figure 2.14 – *Retroaction signal in static mode: U_{DC}, implementing equation 2.13 with analog electronics, is measured as function of the input deflexion. The different curves correspond to seven different values of φ_0 exploring the whole $0 - 2\pi$ interval. The central part of the curves, where $d \ll \lambda$, is independent of the working point.*

hopping. Indeed, U_{DC} is a sinusoidal function of the deflexion d, so any set-point is only defined modulo $\lambda/4\pi$. If during a scan the deflexion d presents a large excursion (steep topography for instance), the retroaction loop may reach another stable point. This fringe hopping mechanism results in artificial steps in the topography image, and in non-constant force imaging. The problem is not present with classic 4 quadrants detectors, as their output is connected to the monotonous error function [103].

An analog circuitry has been recently designed to address this issue in our setup, using the quadrature phase information to produce an adequate retroaction signal. The basic idea is to use one of the contrast as the retroaction signal, but to saturate this signal to its maximum or minimum value when the measurement point leaves the half circle where it should stay. This is done using the electronic scheme of figure 2.15. The first ingredient is

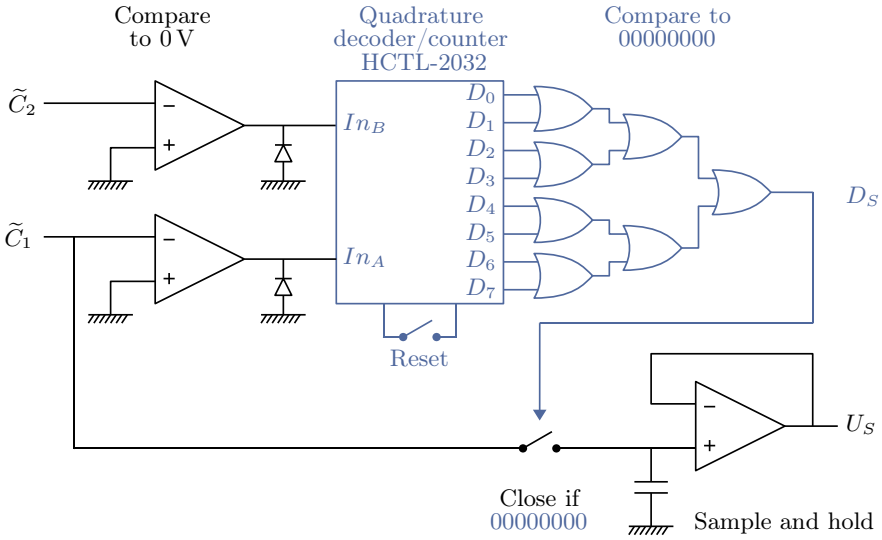

Figure 2.15 – *Alternative retroaction signal in static mode: U_S is equal to $\widetilde{C}_1$ when the quadrature decoder/counter output is zero, and keeps the latest value of $\widetilde{C}_1$ otherwise. Comparison of contrasts $\widetilde{C}_1$,$\widetilde{C}_2$ to 0 provides the logical inputs In_A and In_B of the counter. The* 8 bit *counter value is accessible through the D_0 to D_7 logical outputs, and compared to 0 with cascading logical OR gates to create logical line D_S: D_S is low if the counter output is 0, high otherwise. D_S drives the switch of the sample and hold circuit producing U_S from $\widetilde{C}_1$. Reset of the counter can be performed with a manual switch.*

a quadrature decoder/counter, a common circuitry used with optical choppers associated with rotating objects: a first logical signal is used to count the number of turns, a second one in quadrature to know the direction of the movement. We use a simple comparison to 0 of the measured contrasts $\widetilde{C}_1$ and $\widetilde{C}_2$ as the two inputs to this circuit, and read on its binary output the number of half turns on our measurement circle since last reset of the counter. We process this 8 bit parallel binary output to compare it to 0 with logical OR gates: output logical signal D_S is low when the half turns count is zero, high otherwise. D_S drives the switch of an analog sample and hold circuit. The final output, U_S is equal to $\widetilde{C}_1$ when D_S is low, but freezes to its last value when the counter is incremented or decremented. As a preliminary proof of validity of this strategy, we report in figure 2.16 the measurement of U_S with our experimental realization, when cycling the

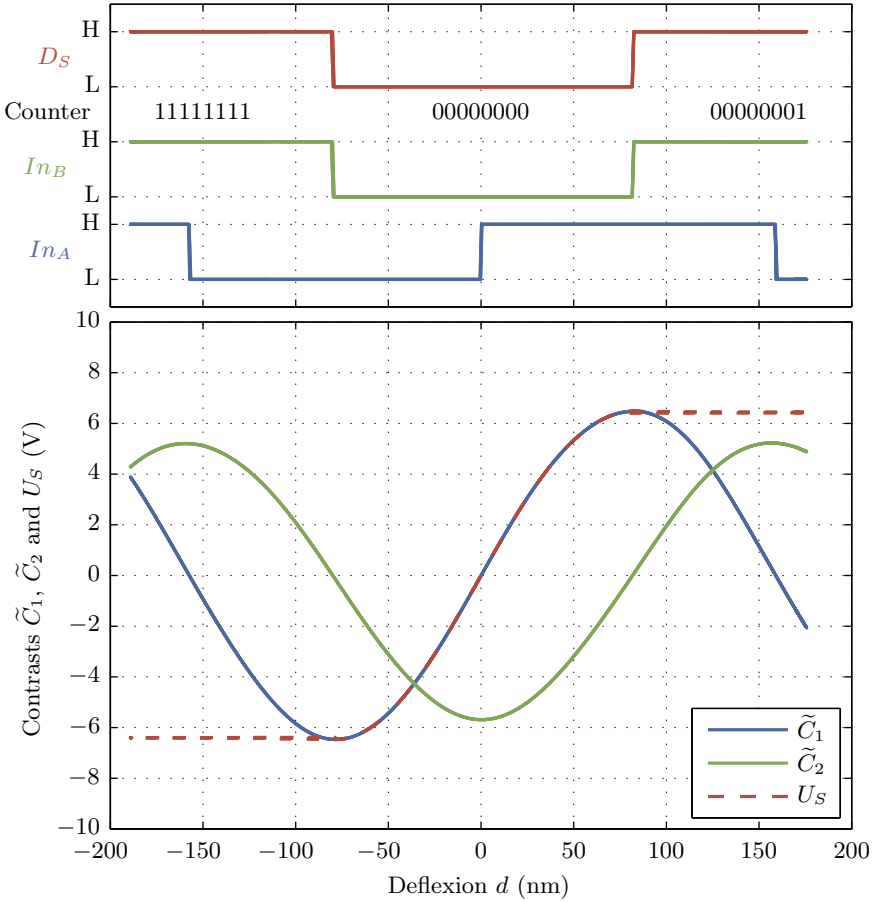

Figure 2.16 – *Alternative retroaction signal in static mode: U_S is equal to $\widetilde{C}_1$ around the deflexion set-point, and saturates to the maximum (minimum) value of $\widetilde{C}_1$ for too large (too small) deflexions d. The top graphics displays the logical values of the inputs In_A and In_B of the quadrature decoder/counter (L and H stand for low and high logical levels), the counter value, and D_S, its comparison to 0 .*

deflexion d over 350 nm. The observed behavior is very similar to that of the output of the position sensor of commercial AFMs, and can be used directly with classic controllers.

In this alternative method to produce the retroaction signal for imaging, we basically use one of the contrast only as the retroaction signal, the second being used only to saturate this signal if the deflexion is too far for the set-point. This implies an optical tuning of the zero, which we were able to avoid using the first strategy leading to U_{DC}. In order to keep the best of both worlds, we should have $U_S = U_{DC}$ around the set point, and a saturation of U_S when U_{DC} reaches its first maximum or minimum. This requires a signal in quadrature with U_{DC}, that is $\propto \cos(\varphi - \varphi_0)$. We could construct this signal using the relation $\cos(\varphi - \varphi_0) = C_1^0 C_1 + C_2^0 C_2$. However this relation is less robust to imperfections of the interferometer than equation 2.13 defining U_{DC}: if $\mathcal{C}_1 \neq \mathcal{C}_2$ and $\psi \neq 0$, the relation is not valid if we simply replace the ideal C_n by their measured equivalents $\widetilde{C}_n$. We therefore didn't spend energy in this direction, and rely on the optical tuning of the zero when we use U_S. Moreover, scanning probe microscopy controllers tend nowadays to be more and more "all digital", with an early digitization of the deflexion signal and a full digital retroaction loop to drive the sample vertical positioning while scanning. The next logical evolution of our quadrature phase interferometer will certainly follow this path, to take full advantage of the high precision and extended deflexion range of our optical system.

2.3.2 Dynamic mode

The approach adapted to dynamic modes is very similar to the one leading to U_{DC}, except that the reference position of the cantilever is now given by a low pass filtration of the contrasts, that will remove fast components in the signal (thus the oscillation of the cantilever). Let us denote by $\langle \ldots \rangle$ the filtration process, and write the optical phase as $\varphi = \langle \varphi \rangle + \delta\varphi$, with $\delta\varphi$ its oscillating part. As long as $\delta\varphi \ll 1$, it can easily be shown that eq. 2.11 still holds replacing contrasts and phase by their the low pass filtered values $C_n^0 = \langle C_n \rangle$ and $\varphi_0 = \langle \varphi \rangle$. We thus define U_{AC} by

$$U_{AC} = \left\langle \widetilde{C}_1 \right\rangle \widetilde{C}_2 - \widetilde{C}_1 \left\langle \widetilde{C}_2 \right\rangle \tag{2.15}$$

Using the expressions of $\widetilde{C}_n$ (eq. 2.12) and a computation similar to the static case, we immediately get

$$U_{AC} = \mathcal{C}_1 \mathcal{C}_2 \cos(\psi)\, \delta\varphi \tag{2.16}$$

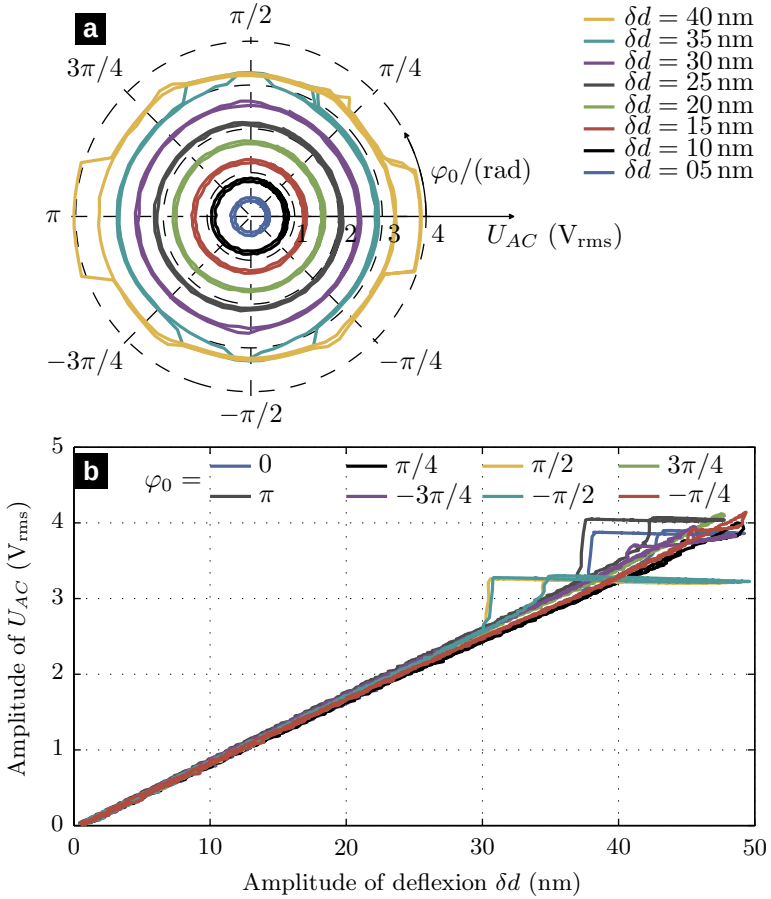

Figure 2.17 – *Retroaction signal in dynamic mode: the rms value of U_{AC}, implementing equation 2.15 with analog electronics, is measured as function of φ_0 (exploring the whole $0-2\pi$ interval) and of the amplitude of oscillation (δd is the peak-peak value of the deflexion). In (**a**), the polar plot highlights the independence of this signal on φ_0: for a given value of the amplitude of oscillation $\delta d < 30\,\text{nm}$, the rms value of U_{AC} is constant within a standard deviation of maximum 3%. An instability is visible at higher forcing. In (**b**), we demonstrate for 8 different values of φ_0 (every $\pi/4$) that the rms value of U_{AC} is linear in δd, at least in the initial part of the curve. The saturation present for $\delta d > 30\,\text{nm}$ is attributed to a slew rate limitation in the analog computation of the contrasts $\widetilde{C}_1$ and $\widetilde{C}_2$. The measurement has been performed on a cantilever driven at its resonance frequency around 250 kHz.*

Again, U_{AC} can directly be used in replacement of standard 4 quadrants deflexion signal in dynamic mode operation. A lock-in detection at the driving frequency is used to extract the root mean square (rms) value of U_{AC}, providing a low frequency signal that is used in the same retroaction loop that is used in contact mode. Sensitivity will always be optimal, whatever the value of φ_0, and is insensitive to any drift of the working point: the low pass filtering will simply follow slow variations of φ_0.

In appendix A.1, a more general computation shows that it is also possible to deal with oscillation amplitudes which are not small compared to the wavelength with a few precautions. Our setup is thus perfectly adapted to imaging in dynamic mode, with no specific restrictions due to the interferometric approach.

The analog circuitry implementing equation 2.15 in our experiment is equivalent to the one designed for DC operation, except that the reference position of the cantilever is obtained by analog low pass filtering (first order filter, cutoff frequency at 1 Hz) instead of the numeric sample and hold. To illustrate the performance of this device, we drive a cantilever at its resonance frequency (around 250 kHz) and measure the rms value of U_{AC} as a function of the amplitude of oscillation of the cantilever δd, for different working points on the measurement circle. The results are presented in figure 2.17: U_{AC} is indeed proportional to δd, the slope being constant with less than a 3% standard deviation when φ_0 describes the whole circle.

For oscillations δd larger than 30 nm peak to peak, a saturation of U_{AC} is observed. We identified this problem to arise from a slew rate limitation of the component AD734 used in the division to compute the contrast $\widetilde{C}_n$. We first observed that the problem is not present at lower frequencies. Moreover, if we slightly degrade the performance of the interferometer by lowering the diameters $\mathcal{C}_1$ and $\mathcal{C}_1$ of the experimental ellipse, we shift the saturation of U_{AC} to larger driving. As a last clue to link saturation to slew rate limitation, figure 2.17(**b**) demonstrates that the saturation is more pronounced along the horizontal and vertical direction of φ_0 than along the diagonals. Indeed, along the diagonals each contrast is $\sqrt{2}$ smaller than the maximum contrasts obtained along the horizontal and vertical directions, delaying apparition of slew rate limitations.

2.3.3 Retroaction loop and sample scanning

In our experimental realization, the retroaction signals U_{DC} and U_{AC} are used as direct replacement for the common 4 quadrants photodiode output in a conventional scanning probe microscope (SPM) arrangement. We use

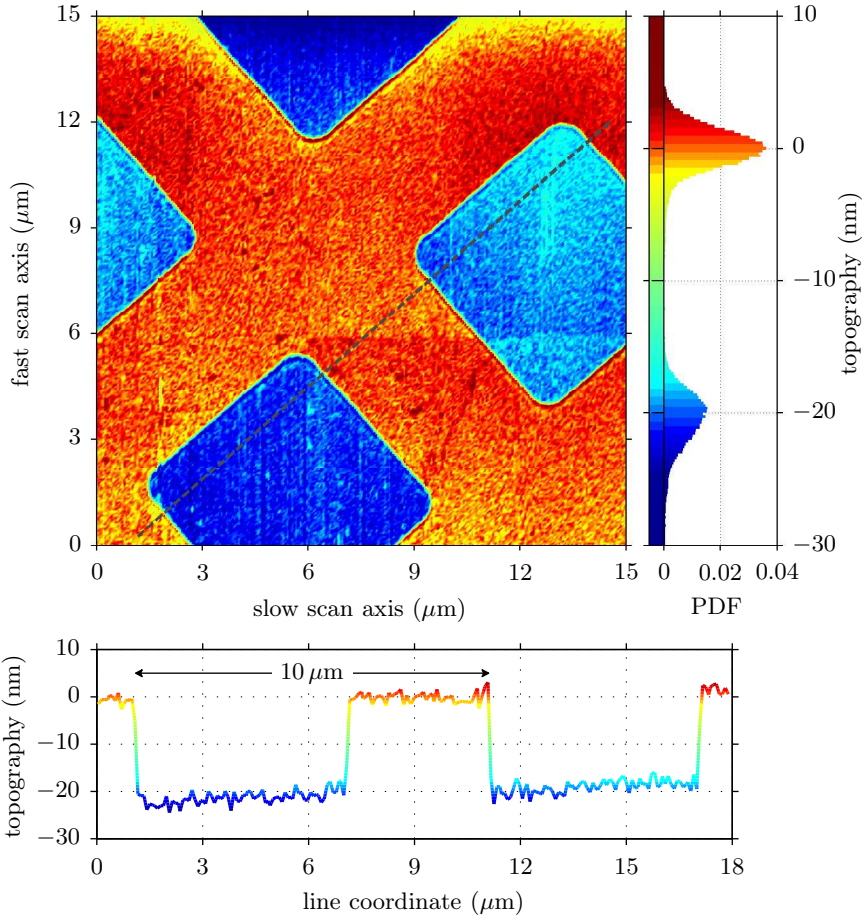

Figure 2.18 – ($15\,\mu\text{m} \times 15\,\mu\text{m}$) *topography image of a calibration sample* Budget Sensors *HS-20MG acquired in contact mode. A "smart" flatten filter has been applied to remove the mean slope of each line of the image. The color scale, along with the normalized histogram (PDF) of the topography is shown on the right, and in the bottom graph we plot a profile corresponding to the dashed line in the image. The geometric pattern of the sample (square holes,* 20 nm *deep, on a* $10\,\mu\text{m}$ *pitch grid) demonstrates the perfect calibration of the piezo translation platform. The rms roughness on each sample plane is around* 2 nm.

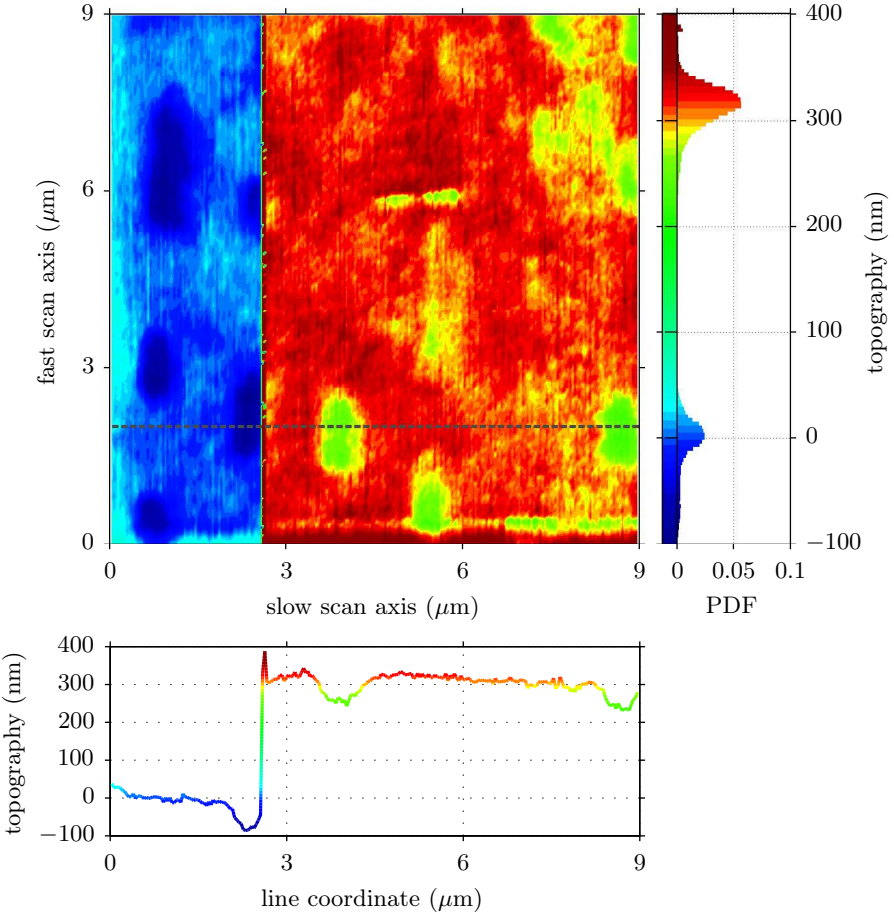

Figure 2.19 – $(9\,\mu\text{m} \times 9\,\mu\text{m})$ *topography image of a CD-R (recordable compact disk) sample acquired in contact mode. The mean plane on the sample has been subtracted to the raw image. The color scale, along with the normalized histogram (PDF) of the topography is shown on the right, and in the bottom graph we plot a profile corresponding the dashed line in the image. The artificial step, about* 315 nm *high, corresponds to an interference fringe hop during the scan.*

a SPM controller SPMagic from *Elbatech*, which drives a piezo translation stage (P-527.3 from PI – *Physik Instrumente*) supporting the sample. This positioning platform can be operated in closed loop, allowing 1 nm accurate horizontal displacement within a 200 μm range, and 0.1 nm precision on the 20 μm vertical range.

When designing the AFM head, we also worked carefully to allow a wide range of operating conditions: the environment can be controlled (vacuum down to 10^{-5} mbar, controlled gas atmosphere), the temperature of the sample can be regulated with 10^{-2} K stability in 200 K to 450 K range, allowing fast temperature changes (quenches for polymer studies for instance). Measurements in liquid environment are also possible in an open cell with a glass window covering a droplet of solvent.

2.3.4 First images

Imaging has been tested only very recently in our instrument, and we present here images of a calibration sample that has been used to validate our approach. In general, imaging quality in AFM is not limited by the precision of the deflexion sensor, but is dependent on many parameters, including the performance of the retroaction loop, the precision of the scanner, the adequacy of the probe, the experience of the operator, etc. Since many elements of our setup are made of standard commercial tools, we do not expect to reach better than average capability for standard imaging modes. The only potential benefit of the interferometer in this case is its calibrated output, that could be used afterwards to correct for tracking imperfections of the retroaction loop: in contact mode, the calibrated error image (difference between the actual deflexion and set-point) can be combined with the topography image (vertical extension of the piezoelectric scanner). We would simply need to acquire the 2 contrasts as auxiliary signals while imaging, and process then afterwards to compute the calibrated deflexion. However, this possibility has not been implemented yet, and we present here just classic topography images in contact and dynamic mode.

Contact mode

We display in figure 2.18 a 15 μm $\times$ 15 μm topography image of a calibration sample *Budget Sensors* HS-20MG (data sheet in appendix D.4), in a region presenting square holes in a 20 nm thick SiO_2 layer covering a silicon substrate. The squares are laid on a 10 μm pitch grid. This $(256\,\text{pixel})^2$ image was acquired with a *NanoWorld* Pointprobe CONTPt tip, in contact mode, using a 0.5 Hz scan speed. A "smart" flatten filter has been applied

to remove the mean slope of the sample: a linear fit on the top plane of the sample is subtracted from each line along the fast axis. The physical parameters we can read on this scan are in perfect agreement with the manufacturer specifications. Using the histogram of height, we measure a rms roughness of the silicon and SiO_2 surfaces of the sample around 2 nm, 10^4 smaller than the vertical range of our piezo translation platform.

As an illustration of the fringe hopping issue we mentioned in section 2.3.1, we present in figure 2.19 an image of a ($9\,\mu m \times 9\,\mu m$) scan of a CD-R (recordable compact disk) sample, where we clearly see an artificial step in the topography. The amplitude of this step, around 315 nm, correspond to a destabilization of the feedback loop during the scan and a jump to another stable mean deflexion, $\lambda/2$ smaller. The input of the retroaction loop is equivalent in the two parts of the image and matches the set-point, since U_{DC} is a periodic function of the deflexion. Although a flatten filter would partially solve the problem by presenting a reasonable topography, the constant force imaging condition would not be met and could be problematic for soft samples. A careful tuning of the retroaction loop together with a slow scan speed may be enough to avoid this issue, but we are currently probing a new approach (contrast saturation) to get rid of this problem, as described in paragraph 2.3.1.

Dynamic mode

We display in figure 2.20 a $10\,\mu m \times 10\,\mu m$ topography image of a calibration sample *Budget Sensors* HS-20MG, in a region presenting SiO_2 circular pillars, 20 nm high over a flat silicon substrate, on a $5\,\mu m$ pitch grid. This $(128\,\text{pixel})^2$ image was acquired with a *Veeco* TESP tip, in tapping mode, using a 0.3 Hz scan speed, and a "smart" flatten filter has been applied to remove the mean plane of the sample. The physical parameters we can read on this scan are in perfect agreement with the manufacturer specifications. The rms roughness of the silicon and SiO_2 surfaces of the sample is measured from the histogram around 2 nm, a performance equivalent to that of contact mode imaging.

2.4 Conclusions and perspectives

In this chapter, we have presented our experimental device: a home made atomic force microscope whose detection is based on a quadrature phase differential interferometer. Several strategies to sense the deflexion have

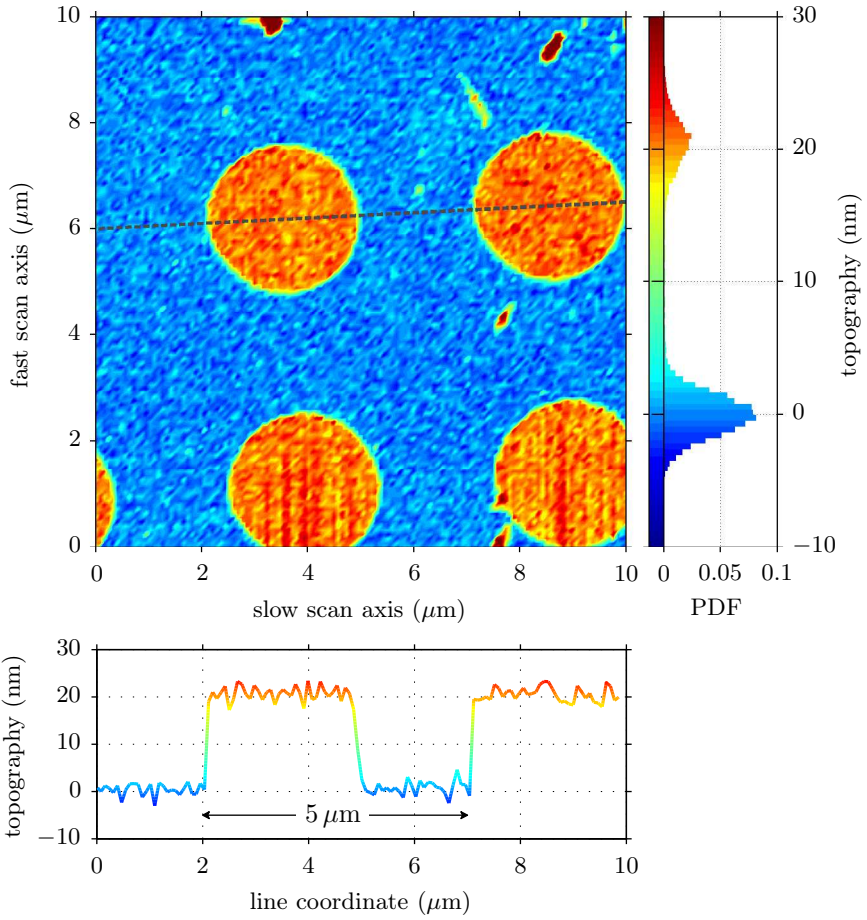

Figure 2.20 – ($10\,\mu\text{m} \times 10\,\mu\text{m}$) *topography image of a calibration sample* Budget Sensors *HS-20MG acquired in tapping mode. A "smart" flatten filter has been applied to remove the mean slope of each line of the image. The color scale, along with the normalized histogram (PDF) of the topography is shown on the right, and in the bottom graph we plot a profile corresponding to the dashed line in the image. The geometric pattern of the sample (circular pillars,* 20 nm *high, on a* 5 μm *pitch grid) is perfectly reproduced.*

been described: the bi-calcite setup features a small environmental susceptibility, and will be used for low frequency thermal noise studies, while the Wollaston configuration allows calibrated measurements on a wide spectral range. The quadrature phase design enables a very high resolution (down to $10^{-14}\,\mathrm{m}/\sqrt{\mathrm{Hz}}$), equaling or out-performing the best results reported in the literature for a much larger deflexion range (up to a few μm). The dual output of the interferometer implies a specific handling to interface common scanning probe microscope controllers. We developed analog circuitries to tackle static (contact mode) and dynamic (tapping mode) operations, and we demonstrated their performance by imaging a simple calibration sample.

Though implementing imaging functionality has been an important milestone to demonstrate the completeness of our device, our innovative setup will be mostly useful for its high force resolution. We will study in the next chapters some situations where the intrinsic thermal noise of the cantilever is our main tool to explore the mechanical properties of micrometer and nanometer sized objects.

As with any instrumental work, many open possibilities remain to keep on improving our setup. As already mentioned, we envision for example a full digital retroaction loop to drive the sample vertical positioning while scanning: it would allow us to take full advantage of the high precision and extended deflexion range of our optical system. We also plan in a short term to add an additional sensor to our AFM: an interferometer to precisely measure the tip-sample distance. Indeed, as in most AFM setups, we currently rely on the piezo translating the sample to infer this separation: a first approach till contact is performed to define the zero of the tip-sample distance, then the piezo is retracted to the desired separation. This technique suffers however from slow environmental drifts (temperature, pressure) which degrades its long time accuracy, a critical point in some of the studies we are planning. The current maximum drift is measured around $0.2\,\mathrm{nm/s}$. We thus need to measure independently the probe-surface distance, and if needed use this information as a retroaction signal to drive the sample position and keep the distance at the desired value. For this, we will build a second differential interferometer with performances similar to the one used for deflexion measurement. It will provide our experimental setup another unique feature with respect to commercial devices, and could open many research tracks beyond our current project.

Chapter 3

Thermal noise and dissipation of cantilevers

Partially in collaboration with Bruno Tiribilli
ISC-CNR Firenze

Abstract

In this chapter, we first present a simple theoretical framework to describe the mechanical response function and the thermal noise of a micro-cantilever in a viscous fluid. We use Sader's approach to describe the effect of the surrounding fluid (added mass and viscous drag), and the fluctuation dissipation theorem for each flexural mode of the system to derive a general expression for the power spectrum density of fluctuations. Equivalently, we demonstrate using Kramers-Kronig relation that we can reconstruct the mechanical response function of the cantilever from a thermal noise spectrum.
We then measure the mechanical thermal noise of AFM cantilevers. Using an interferometric setup, we obtain a resolution down to $10^{-14}\,\mathrm{m}/\sqrt{\mathrm{Hz}}$ *on a wide spectral range (*$3\,\mathrm{Hz}$ *to* $10^5\,\mathrm{Hz}$*). The low frequency behavior depends dramatically on the presence of a reflective coating: almost flat spectra for uncoated cantilevers versus* $1/f$ *like trend for coated ones. We show that this effect arise from a viscoelastic response associated with the coating. We also demonstrate the validity of Sader's model for viscous damping on the full frequency range.*
Finally, we present measurements of the spatial repartition of fluctuations. These thermal noise maps are compared with Euler-Bernoulli's description of the flexural modes, and Saint-Venant's of the torsional modes. The cantilever stiffness can be precisely measured from this approach, as well as the elastic coefficients E (Young's modulus) and S (shear modulus) of its constituting material. The correct description of the dispersion relation for torsional modes leads to the consideration of a refined model to account for observations at high mode numbers.

3.1 Introduction

Cantilevers of micrometer size are nowadays present in many applications, ranging from chemical and biological sensors [84] to scanning probe microscopy [96]. They are also ubiquitous as fundamental bricks of microelectromechanical systems (MEMS). Through Atomic force microscopy (AFM), they are currently used in a great variety of studies involving small forces measurement [27], including unfolding of proteins [29, 52], probing the structure of biological membranes [53] and monitoring the mechanical response of living cells [113, 125] as well as Micro-Electro-Mechanical Systems (MEMS) and other nanotechnological devices [17, 84]. Functionality of MEMS or cantilever based sensors relies on mechanical movements and deformation of the microscopic mechanical beam. Their thermal fluctuations represent one of the most important noise sources and finally determines the ultimate sensitivity of the sensor [26, 45, 84, 87, 88, 124, 146] or operating condition of MEMS. This mechanical-thermal noise can also be important in the study of macroscopic systems, and has been shown for instance to be a relevant term in the sensitivity limitations of interferometric detectors for gravitational waves [58, 76, 99, 115].

As shown by the fluctuation dissipation theorem (FTD) [28], these thermally induced fluctuations are linked to the mechanical response function of the system, and more specifically to the losses of energy occurring during deformations. Many models have been proposed to account for the numerous physical sources of dissipation: viscous damping in the surrounding fluid [119], clamping losses [146], thermoelastic dissipation [147–149], etc. The approach by Sader and co-workers [61, 119, 136] for instance provides a thorough study of viscous dissipation, predicting a frequency dependent damping coefficient. Focusing on structural damping, Saulson [124] proposed a model of mechanical-thermal noise for a simple harmonic oscillator with viscoelastic dissipation. In particular he showed that this mechanism leads to a power spectrum density (PSD) of fluctuations presenting a $1/f$ trend at low frequency. In general, a key difference between all these models is the frequency dependence of the noise or dissipation. It is however a great challenge to measure thermal noise or small damping on a wide range of frequency, and very few experiments [58, 76, 99, 145] have succeed so far in directly measuring fluctuations out of resonances, notably at low frequencies.

The thermal noise of micro-cantilevers, though presenting a limit to their operation, can also be used as a tool to explore their mechanical properties. A common procedure to calibrate the stiffness of AFM cantilevers, based

on thermal fluctuations [69], is for example proposed in most commercial devices: the equipartition theorem states that the energy stored in the spring is in average equal to the thermal energy, thus

$$\frac{1}{2}k\left\langle d^2\right\rangle = \frac{1}{2}k_B T \tag{3.1}$$

where k is the spring constant to calibrate, $\left\langle d^2\right\rangle$ the mean quadratic deflexion, k_B the Boltzmann constant and T the temperature. This calibration step is required if one wants to exploit the great accuracy in measuring the cantilever deflexion offered by AFM and convert this measurement in units of force. In principle, one could rely on the geometrical dimension of the probe and tabulated mechanical properties of its material to compute k, but in practice this is not possible. Indeed, the cantilever thickness lays in the sub micrometer to a few micrometers range, leading to a high incertitude on its actual value. Moreover, description of the system from its bulk mechanical properties only may start to loose some validity at this scale, where surface effects cannot be neglected anymore [34, 38, 88, 122]. Finally, commonly used coatings of cantilevers increase even more the complexity of their theoretical description. Thermal fluctuations supply therefore a useful insight to characterize experimentally those systems, provided the acquisition device is precise enough to perform clean noise measurements.

In this chapter, we perform direct measurements of the mechanical-thermal noise of micro-cantilevers with our high resolution interferometer. A main advantage of this setup is that it offers, thanks to its sensitivity, the possibility to resolve not only the resonances of the PSD as in the standard AFM optical lever technique, but the whole spectrum up to the second mode. Moreover, its calibrated output allows quantitative measurements. We extract from the thermal noise analysis valuable information about the dissipation processes, both from the surrounding fluid and from structural damping. We also demonstrate how we can perform a precise characterization of the mechanical properties of the cantilever and its constituting material.

The chapter is organized as follows: in a first section, we present a general theoretical framework to study the thermal noise of a cantilever, and some useful tools. The microscopic beam is modeled with an Euler-Bernoulli description, and Sader's approach is introduced for viscous dissipation. Using FDT and Kramers-Kronig relations, we demonstrate how to compare theoretical models and experimental data in terms of both noise spectra and mechanical response. In a second part, we focus on dissipative processes. We first validate Sader's model for viscous damping on a wide spectral

range. We then present a thorough examination of viscoelasticity in gold coated cantilevers, providing a quantitative phenomenological description of this effect. In a last part, we tackle the characterization of the mechanical properties of cantilevers from a mapping of the thermal noise on its surface. This analysis validate the description of the system in terms of its normal modes of oscillation, and lead to a quantitative evaluation of its stiffness and elastic moduli.

3.2 Theoretical description of cantilevers' fluctuations and dissipation

3.2.1 From mechanical response to thermal noise: FDT and Sader's model

Simple Harmonic Oscillator

In a first approximation, the AFM cantilever can be modeled by a damped spring-mass system. The displacement d of the punctual mass in the model will correspond to the deflexion of the cantilever, the spring constant k to the response of the sensor to the external force F acting on its tip, the mass m to the inertia of the mechanical beam, and the damping coefficient γ to the dissipation processes due to the surrounding atmosphere. This Simple Harmonic Oscillator (SHO) responds to the equation of motion:

$$m\ddot{d} = -kd - \gamma\dot{d} + F \tag{3.2}$$

where dotted variables are derivated with respect to time t. In Fourier's space this equation is used to define the mechanical response function G^{SHO} as:

$$G^{\mathrm{SHO}}(\omega) = \frac{F(\omega)}{d(\omega)} = k\left[1 - \frac{\omega^2}{\omega_0^2} + i\frac{\omega}{Q\omega_0}\right] \tag{3.3}$$

where we introduced the resonant pulsation $\omega_0 = \sqrt{k/m}$, the quality factor $Q = m\omega_0/\gamma$, and $\omega = 2\pi f$ is the pulsation corresponding to frequency f.

The force F and the displacement d are coupled by the Hamiltonian $\mathcal{H}$ of the system. Indeed, the infinitesimal work of F when the displacement changes by δd is $\delta W = F\delta d$, thus for a reversible transformation, $d\mathcal{H} = \delta W = F\delta d$, hence

$$\frac{\partial \mathcal{H}}{\partial d} = F \tag{3.4}$$

This last equation shows that d and F are coupled variables by the hamiltonian of the system. We can thus apply the Fluctuation Dissipation Theorem (FDT) [28, 39]: the Power Spectrum Density[1] (PSD) S_d^{SHO} of thermal fluctuations of d is

$$S_d^{\mathrm{SHO}}(f) = -\frac{4k_BT}{\omega}\mathrm{Im}\left[\frac{1}{G^{\mathrm{SHO}}(\omega)}\right] = \frac{4k_BT}{k\omega_0}\frac{1/Q}{\left(1-u^2\right)^2+(u/Q)^2} \qquad (3.5)$$

where k_B is the Boltzmann constant, T the temperature of the system, $u = \omega/\omega_0$ is the reduced frequency, and Im(.) is the imaginary part of its argument.

The use the fluctuation dissipation theorem thus allows us to predict the expected thermal noise from the mechanical model of the oscillator. We plot in figure 3.2 an example of response function and associated spectrum for a SHO model. The real part of the response is a parabola centered on $f = 0$, the value at the origin being the spring constant k, and the parabolic shape the signature of the inertial cutoff. The imaginary part is simply linear in frequency: dissipation is proportional to velocity, and thus frequency. The PSD computed from the FDT presents a characteristic Lorentzian shape, peaked at the resonance frequency $f_0 = \omega_0/2\pi$. The quality factor Q can be inferred from to the width of the resonance at half height, while the stiffness k can be computed from the integral of the curve: from the equi-repartition theorem we have $\int_0^\infty S_d^{\mathrm{SHO}}(f)\mathrm{d}f = \left\langle d^2\right\rangle = k_BT/k$.

Beyond SHO: the Sader model

This SHO model gathers the main points of the physics of the AFM cantilever, as long as we are only interested in its behavior around the first resonance. However, we need a more realistic description of the system to depict its various modes of oscillation, or to predict the mechanical behavior from the physical parameters (geometry, material) of the cantilever. For this spatially extended system, the application of the FDT is not trivial: the variable coupled to our observable (the deflexion of the cantilever free extremity) is not obvious, nor is the description of the coupling with the fluid. The first step is to describe the cantilever as a clamped-free beam in an Euler-Bernoulli framework [82]. This leads to characterize the system behavior in terms of normal modes, the amplitude of each mode being governed by

[1] In this document we will use one sided power spectrum density functions of frequency f, such that $\left\langle d^2(x)\right\rangle = \int_0^\infty S_d(f)df$, for easier comparison to experiments, whereas response functions G will be given as a function of the pulsation ω.

an harmonic oscillator equation [26]. The next ingredient to add is dissipation. In many cases, AFM are operated in a fluid environment (air or water for instance) which is the main source of dissipation: the viscosity of the medium will broaden the structural resonances. An added mass effect due to the fluid moving along with the cantilever can also shift their frequencies, especially in liquid environments. A few theoretical models have been proposed to account for these effects [4, 46, 50, 61, 91, 109, 110, 119, 120, 136], and validated experimentally [4, 25, 32, 50, 55, 91, 120] on the basis of the dependence of the quality factor on the surrounding fluid and the mode number (and thus the frequency).

Among the predictions of these approaches, we are interested here in the power spectrum of thermal noise induced fluctuations. We will focus only on the most complete analytical approach, by Sader and coworkers [61, 119, 136]. In reference [6], we derive a generic formula for the thermal noise using the fluctuation dissipation theorem for each mode, extending the work of Paul and Cross [109] in a simpler framework than Dorignac et al. [46]. This careful analysis is indeed incorrect in the original work of Sader and coworkers, as noted by Paul and Cross [109], Dorignac et al. [46] and Sader et al. themselves (see reference 44 of [61]). We refer the reader to reference [6] for the complete demonstration, and limit this paragraph to the main points of interest.

The rectangular cantilever is described in an Euler Bernoulli framework: its length l is supposed to be much larger than its width w, which itself is much larger than its thickness h. We will limit ourself in this study to the flexural modes of the cantilever: the displacement field is supposed to be only perpendicular to its main plane (along axis z of Fig.3.1) and uniform across its width. These deformations can thus be described by the deflexion $d(x,t)$, x being the spatial coordinate along the beam, and t the time. The equation of motion is:

$$\frac{k}{3}l^3\frac{\partial^4 d(x,t)}{\partial x^4} + \frac{m}{l}\frac{\partial^2 d(x,t)}{\partial t^2} = f_{\text{ext}}(x,t) + f_{\text{hydro}}(x,t) \tag{3.6}$$

or equivalently in Fourier's space:

$$\frac{k}{3}l^3\frac{\mathrm{d}^4 d(x|\omega)}{\mathrm{d}x^4} - \frac{m}{l}\omega^2 d(x|\omega) = f_{\text{ext}}(x|\omega) + f_{\text{hydro}}(x|\omega) \tag{3.7}$$

where k and m are the cantilever static stiffness and mass, and f_{ext} and f_{hydro} are the external and hydrodynamic forces per unit length. If those forces are zero, the solutions to this equation are the normal modes $\phi_n(x)$

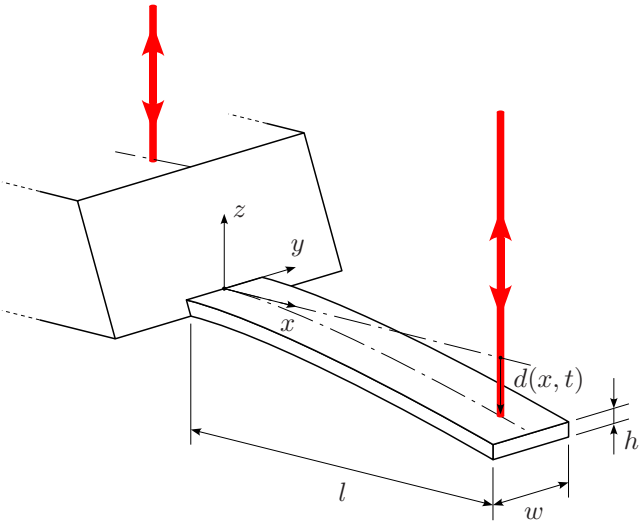

Figure 3.1 – *Schematics of the cantilever. In the Euler Bernoulli approach, the cantilever bending is modeled by a vertical deflexion $d(x,t)$ of its neutral axis, where x is the spatial coordinate along the beam length and t the time. The cantilever thickness h is supposed to be much smaller than its witdh w, itself much smaller than the length l.*

matching the boundary conditions of a clamped-free beam:

$$\phi_n(x) = (\cos\alpha_n \frac{x}{l} - \cosh\alpha_n \frac{x}{l}) + \frac{\cos\alpha_n + \cosh\alpha_n}{\sin\alpha_n + \sinh\alpha_n}(\sin\alpha_n \frac{x}{l} - \sinh\alpha_n \frac{x}{l}) \tag{3.8}$$

where the normalized spatial wave numbers $\alpha_1 = 1.875$, $\alpha_2 = 4.694$, ..., $\alpha_n = (n-1/2)\pi$ are the roots of $1+\cos\alpha_n \cosh\alpha_n = 0$. The normal modes form an orthonormal basis of functions of x on $[0-1]$. Figure 2.11 gives an illustration of the shape of these structural resonances. The pulsations ω_n of these normal modes are ruled by the dispersion equations:

$$m\omega_n^2 = \frac{\alpha_n^4}{3}k = k_n \tag{3.9}$$

In Sader's original model [119], the fluid motion is supposed to be bi-dimensional (in (y,z) planes): a segment dx of height h and width w at a position x along the cantilever is treated as if it had an infinite length along

x. $f_{\text{hydro}}(x|\omega)$ is thus vertical, and depends on $d(x|\omega)$ only:

$$f_{\text{hydro}}(x|\omega) = \frac{m}{l}\omega^2\tau(\omega)d(x|\omega) = \frac{m}{l}\omega^2\left[\tau_r(\omega) + i\tau_i(\omega)\right]d(x|\omega) \tag{3.10}$$

where $\tau = \tau_r + i\tau_i$ is the hydrodynamic function of a rectangular cantilever (to a geometric multiplicative factor). An explicit formula for this function is given in Sader's original work [119], and can be used to compute $\tau(\omega)$ for any specific cantilever dimension. To solve the differential equation 3.7 linking the deflexion d to the external force f_{ext}, we project those two quantities on the basis of normal modes ϕ_n:

$$d(x|\omega) = \frac{1}{\sqrt{l}}\sum_{n=1}^{\infty}\beta_n(\omega)\phi_n(x) \tag{3.11}$$

$$f_{\text{ext}}(x|\omega) = \frac{1}{\sqrt{l}}\sum_{n=1}^{\infty}\eta_n(\omega)\phi_n(x) \tag{3.12}$$

This decomposition is also valid in time space, where the amplitude $\beta_n(t)$ and forcing $\eta_n(t)$ of each mode are simply the inverse Fourier transform of $\beta_n(\omega)$ and $\eta_n(\omega)$. Those two variables are coupled by the Hamiltonian $\mathcal{H}$ of the system. Indeed, let us compute the infinitesimal work δW of f_{ext} when the deflexion changes by δd:

$$\delta W = \int_0^l \mathrm{d}x f_{\text{ext}}(x,t)\delta d(x,t) \tag{3.13}$$

$$= \sum_{n=1}^{\infty}\eta_n(t)\delta\beta_n(t) \tag{3.14}$$

For a reversible transformation $d\mathcal{H} = \delta W$, hence

$$\frac{\partial\mathcal{H}}{\partial\beta_n} = \eta_n \tag{3.15}$$

This last equation demontrates that the amplitude β_n and the forcing η_n of each mode are coupled variables, we can thus apply the FDT. Let us first compute the mechanical reponse function G_n of mode n by projecting equation 3.7 on the basis of normal modes ϕ_n:

$$\left(\frac{k}{3}\alpha_n^4 - m\omega^2\left[1+\tau(\omega)\right]\right)\beta_n(\omega) = \eta_n(\omega) \tag{3.16}$$

therefore

$$G_n(\omega) = \frac{\eta_n(\omega)}{\beta_n(\omega)} \tag{3.17}$$

$$= \frac{k}{3}\alpha_n^4 - m\omega^2\left[1 + \tau_r(\omega)\right] - im\omega^2\tau_i(\omega) \tag{3.18}$$

$$= k_n - m_{\text{eff}}(\omega)\omega^2 - i\gamma_{\text{eff}}(\omega)\omega \tag{3.19}$$

Each normal mode is thus equivalent to an oscillator of stiffness k_n, mass $m_{\text{eff}}(\omega) = m\left[1 + \tau_r(\omega)\right]$ (cantilever mass plus additive inertial term accounting for the fluid moving along with it), and damping coefficient $\gamma_{\text{eff}}(\omega) = m\omega\tau_i(\omega)$. Using the FDT, power spectrum density S_{β_n} of its amplitude fluctuations reads:

$$S_{\beta_n}(f) = \frac{4k_BT}{\omega}\text{Im}(\frac{1}{G_n(\omega)}) \tag{3.20}$$

$$= 4k_BT\frac{\gamma_{\text{eff}}(\omega)}{(k_n - m_{\text{eff}}(\omega)\omega^2)^2 + (\gamma_{\text{eff}}(\omega)\omega)^2} \tag{3.21}$$

For reasonably shaped cantilevers, $m_{\text{eff}}(\omega)$ and $\gamma_{\text{eff}}(\omega)$ are slow varying function of the frequency, each mode is thus around the resonance almost equivalent to an harmonic oscillator of stiffness k_n, mass $m_{\text{eff}}(\omega_n)$ and damping coefficient $\gamma_{\text{eff}}(\omega_n)$. However, the response and thermal noise spectrum show some deviations to the SHO model at low and high frequency, as illustrated in figure 3.2.

In Sader's model, dissipation is homogeneous along the cantilever, so the thermal noises acting on different modes are uncorrelated. The fluctuation of the deflexion measured at coordinate x is thus the sum of the contribution of each mode:

$$S_d(x, f) = \frac{1}{l}\sum_{n=1}^{\infty} S_{\beta_n}(f)|\phi_n(x)|^2 \tag{3.22}$$

We eventually have a complete model of the mechanical response of the cantilever in Fourier's space, and a description of its thermal fluctuations from the FDT applied to each normal mode. In section 3.3, we present some experimental results validating this approach.

3.2.2 From fluctuations to mechanical response: FDT and Kramers Kronig relations

Comparing the thermal noise spectrum of a measurement and a mechanical model is interesting as it can validate the pertinency of the model, but it

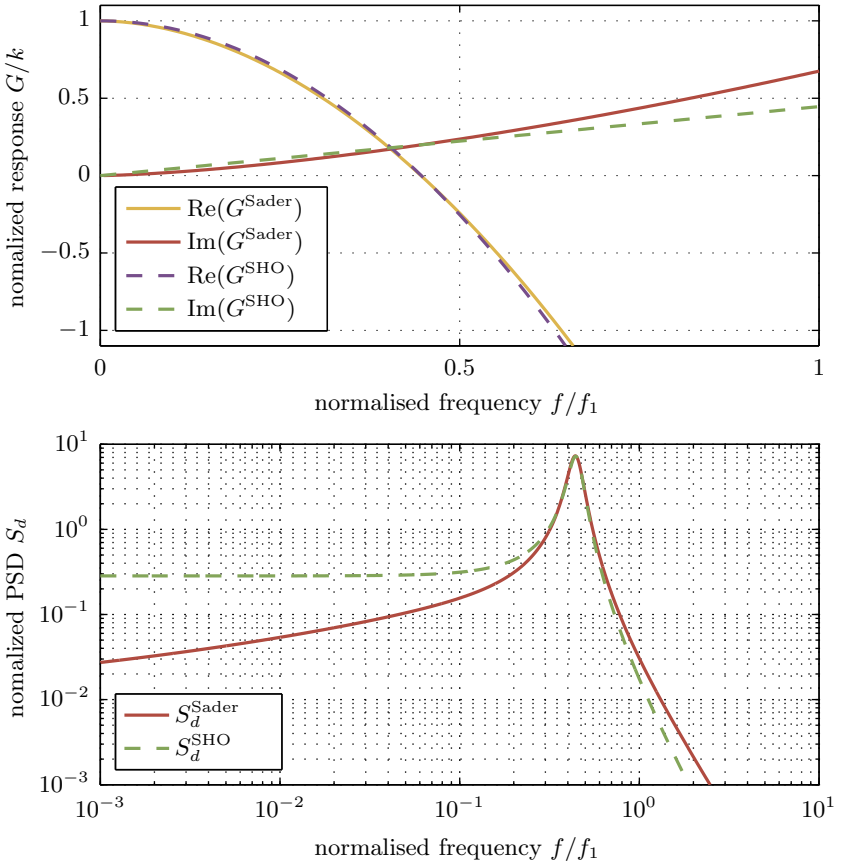

Figure 3.2 – *Mechanical response function (G, top) and thermal noise spectrum (S_d, bottom) versus frequency f for two different models of a cantilever. Sader's model for the first normal mode of a* 250 µm *long,* 35 µm *wide and* 4 µm *thick silicon cantilever in water is used as an example. A fit of this curve with the spectrum of a simple harmonic oscillator (*SHO*) is superposed. f is normalized to the vacuum resonance frequency f_1: the additional inertia due to the fluid moving around the cantilever shifts the resonance to a lower frequency. The deviation of* $\mathrm{Re}(G^{\mathrm{Sader}})$ *to the parabolic shape of the* SHO *model is a signature of the frequency dependence of this added mass effect. The dissipation of Sader's model also presents a specific frequency dependence that departs from the linear behavior of* $\mathrm{Im}(G^{\mathrm{SHO}})$*. It results in a thermal noise slowly decreasing when f goes to 0, instead of the plateau of the* SHO *model.*

would be even more interesting to reconstruct the response of the cantilever directly from the experimental data. We explicit in this section how our high precision enables this process. The first step is to realize that using FDT, the power spectra we measure are in fact a direct access to the imaginary part of $G^{-1}(\omega) = d(\omega)/F(\omega)$:

$$\mathrm{Im}[G^{-1}(\omega)] = -\frac{\omega S_d(f)}{4k_B T} \tag{3.23}$$

The second step comes from G^{-1} being the linear response function of deflexion d to an external force F in Fourier's space. It thus obeys the Kramers-Kronig relations [39]:

$$\mathrm{Re}[G^{-1}(\omega)] = \frac{1}{\pi}\mathcal{PP}\int_{-\infty}^{\infty}\frac{\mathrm{Im}[G^{-1}(\Omega)]}{\Omega-\omega}\mathrm{d}\Omega \tag{3.24}$$

$$\mathrm{Im}[G^{-1}(\omega)] = -\frac{1}{\pi}\mathcal{PP}\int_{-\infty}^{\infty}\frac{\mathrm{Re}[G^{-1}(\Omega)]}{\Omega-\omega}\mathrm{d}\Omega \tag{3.25}$$

where $\mathcal{PP}$ stands for the principal part of the integral. Using the first of these two equations, the knowledge of $\mathrm{Im}[G^{-1}(\omega)]$ can lead to $\mathrm{Re}[G^{-1}(\omega)]$, and thus to the full response function G. This approach is possible with our experimental data as we measure the PSD of fluctuations on a very wide spectral range, not limited to the resonance. Computing the integral relation 3.24 should therefore be possible. We detail in the following paragraphs the various tricks we use to ensure the good precision of our reconstruction algorithm.

Computing the integral

Relation 3.24 is hazardous to compute directly as the term inside the integral present a divergence in $\Omega = \omega$ (hence the principal part). However, inspired by the work of Schnurr [127], we show that this divergence can be avoided by a computation in the temporal space, using properties of the Hilbert transform. The Hilbert Transform (HT) of a function $g(\omega)$ is defined by:

$$\mathrm{HT}\left[g(\omega)\right] = \frac{1}{\pi}\mathcal{PP}\int_{-\infty}^{\infty}\frac{g(\Omega)}{\Omega-\omega}\mathrm{d}\Omega \tag{3.26}$$

We are in particular interested by a specific property of the Hilbert transform: for a function of complex value $g(\omega^\star)$ that is analytic (in at least half the complex plane), the inverse Fourier transform FT^{-1} of the Hilbert Transform obeys:

$$\mathrm{FT}^{-1}\left[\mathrm{HT}\left[g(\omega^\star)\right]\right](t) = \big(-i\,\mathrm{sign}(t)\big)\cdot\mathrm{FT}^{-1}\left[g(\omega^\star)\right](t) \tag{3.27}$$

where sign(t) function is -1 for $t < 0$, 1 for $t > 0$ and 0 for $t = 0$.

The first Kramers-Kronig relation (3.24) can be expressed using the Hilbert transform:

$$\mathrm{Re}\left[G^{-1}(\omega)\right] = \mathrm{HT}\left[\mathrm{Im}\left[G^{-1}(\omega)\right]\right] \tag{3.28}$$

The idea is then to use twice the Fourier transform to reconstruct the real part $G^{-1}(\omega)$:

$$\mathrm{FT}^{-1}\Big[\mathrm{Re}\left[G^{-1}(\omega)\right]\Big](t) = \big(-i\,\mathrm{sign}(t)\big)\cdot \mathrm{FT}^{-1}\Big[\mathrm{Im}\left[G^{-1}(\omega)\right]\Big](t) \tag{3.29}$$

Parity properties of the response function implies $\mathrm{FT}^{-1}\Big[\mathrm{Im}\left[G^{-1}(\omega)\right]\Big]$ is a purely imaginary function, thus we can rewrite equation 3.29 in:

$$\mathrm{FT}^{-1}\Big[\mathrm{Re}\left[G^{-1}(\omega)\right]\Big](t) = \mathrm{sign}(t)\cdot \mathrm{Im}\Big[\mathrm{FT}^{-1}\Big[\mathrm{Im}\left[G^{-1}(\omega)\right]\Big](t)\Big] \tag{3.30}$$

$$= \mathrm{sign}(t)\cdot G_i^{-1}(t) \tag{3.31}$$

where we introduce the notation $G_i^{-1}(t)$ for easier reading. All is left to do then is to use a direct Fourier transform to compute the real part of G^{-1}:

$$\mathrm{Re}\left[G^{-1}(\omega)\right] = \mathrm{FT}\Big[\mathrm{sign}(t)\cdot G_i^{-1}(t)\Big] \tag{3.32}$$

The 3 steps algorithm corresponding to equations 3.23, 3.30 and 3.32 is given in Appendix B.2, allowing us to reconstruct from the spectrum $S_d(f)$ the full mechanical response function $G(\omega) = 1/G^{-1}(\omega)$.

Handling finite spectral range

One of the common problem with Kramers-Kronig relations is the finite spectral range we have access to: since the reconstruction process of $\mathrm{Re}(G^{-1})$ is based on an integral relation, missing data at low and high frequency can limit the precision of the reconstruction. In our case, the problem arises from the high frequency part of the spectrum: the inertial cutoff for large f lowers the thermal noise below the background noise of our interferometer, where S_d is thus unknown.

To illustrate our demonstration, we will use a synthetic signal from a model experiment. We use Sader's model to compute the response function and the thermal noise (both limited to the first mode) of a silicon cantilever of length $l = 450\,\mu$m, width $w = 45\,\mu$m and thickness $h = 1.8\,\mu$m,

thermalized at $T = 295\,\mathrm{K}$ in air. We will then use this synthetic spectrum $S_d^{\mathrm{Sader}}(f)$ and try to recover the initial response function $G^{\mathrm{Sader}}(\omega)$ with the Kramers-Kronig algorithm. The frequency range considered is limited to $50\,\mathrm{kHz}$, since at higher f the mechanical noise is below $1.4 \times 10^{-14}\,\mathrm{m}/\sqrt{\mathrm{Hz}}$, taken as the background noise of the measurement. We plot in figure 3.3 this synthetic spectrum S_d^{Sader} and the dissipative part $\mathrm{Im}(G^{\mathrm{Sader}})$ of the response function to be recovered.

If we apply the Kramers-Kronig algorithm directly to the PSD limited to $50\,\mathrm{kHz}$, we have a very bad estimation of the actual dissipation, as illustrated in figure 3.3: the shape of the curve is completely different from the initial response function. The usual strategy adopted in this case is to use an ad hoc model to supplement the experimental data at high frequency, and compute the response from this hybrid data. We choose here to complement the data with a SHO model, tuned to have a similar spectrum below $50\,\mathrm{kHz}$ and a reasonable extrapolation above. If we apply the reconstruction algorithm to this padded spectrum, we have better and better accuracy when the padding reaches larger and larger frequency range. The reconstructed response matches the original one within 3 % if we expand the frequency range by a factor 8 (and only 10 % if we expand it by a factor 4). This method is however inelegant since it requires a huge amount of artificial data to reach a reasonable accuracy.

Differential Kramers-Kronig approach

We propose here a nicer method without the need of expanding the frequency range of the experimentally available spectrum. The idea is very simple and based on the linearity of the Kramers-Kronig relations: if we denote by KK the operations corresponding to the previously described algorithm, that is

$$\frac{1}{G(\omega)} = \mathrm{KK}\left(S_d(f)\right) \tag{3.33}$$

then we may write

$$\frac{1}{G^{\mathrm{Sader}}(\omega)} - \frac{1}{G^{\mathrm{SHO}}(\omega)} = \mathrm{KK}\left(S_d^{\mathrm{Sader}}(f) - S_d^{\mathrm{SHO}}(f)\right) \tag{3.34}$$

The nice outcome of this trick is that the input to consider for the Kramers-Kronig algorithm is now zero outside the frequency range experimentally available. Indeed, we extrapolated the original data with the SHO model outside this range, where the 2 spectra are strictly the same. The contribution of this high frequency data to the integral relation is thus zero, whether

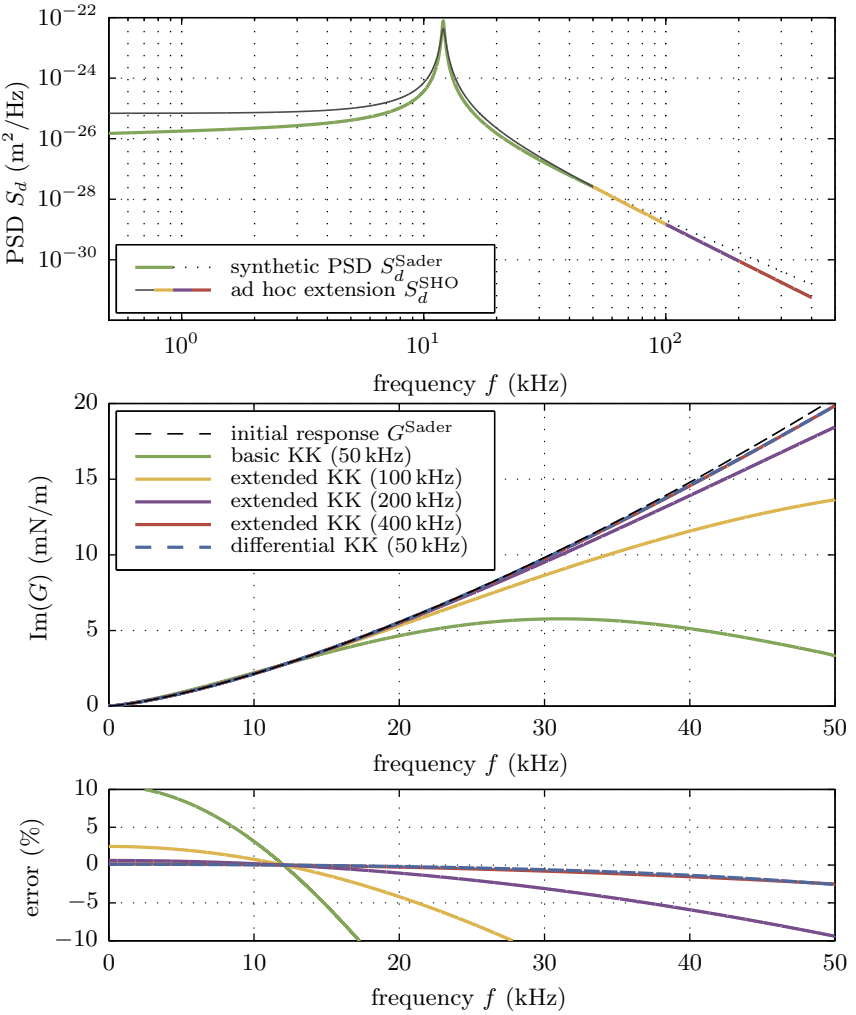

Figure 3.3 – *We create a synthetic thermal noise spectrum from the Sader model, and limit it to a* 50 kHz *range. We use an ad hoc SHO model to compensate for the missing high frequency data. The reconstructed response from the Kramers-Kronig algorithm is not accurate unless a long extrapolation of the spectrum to large frequencies is made, or a smart approach using the difference between the experimental data and a reference spectrum is conducted. The error on the dissipative part of the rescontructed mechanical response function is smaller than* 3% *in this last case.*

or not it is considered. G^{SHO} being known, equation 3.34 can easily be used to estimate the response function G^{Sader} from the power spectrum S_d^{Sader}. We plot in figure 3.3 the output of this strategy for the same synthetic spectrum, and demonstrate the high precision of this approach without expanding the frequency range at all. The accuracy is slightly better with this strategy than with an extrapolation of the spectrum to 400 kHz (8 times the accessible range) !

3.2.3 Thermal noise analysis toolbox: summary

In order to study the mechanical behavior of a cantilever from its thermal noise spectrum, we introduced in this section a few useful tools. The keystone of the analysis is the Fluctuation-Dissipation Theorem (FDT), relating the thermal noise spectrum to the dissipative part of the response. We may adopt two different approaches to deal with experimental spectra. The first one is to propose a model for the cantilever, and to check that the inferred PSD matches the measurement data. A simple oscillator model can be sufficient to describe one structural resonance, and a full model is provided by Sader's approach to deal with a large frequency range. The second way to handle experimental PSD is to use Kramers-Kronig relations, as soon as we access the spectrum on a wide spectral range. We have shown on a synthetic spectrum that with a few numerical tricks, we were able to reconstruct the full response function with a very good accuracy. We will now apply these approaches to measurements performed with our high precision interferometer on various AFM cantilevers.

3.3 Dissipation processes at low frequency

In this section, we will focus mainly on the mechanical properties of contact cantilevers around their first resonance and at lower frequencies. We will first deal with raw silicon cantilevers in air, presenting a nice concordance with Sader's model for viscous dissipation. Some of the data presented can also be found in reference [6]. In a second part, based on reference [104], we will study golden coated cantilevers, and show that another dissipation process has to be accounted for in such a case.

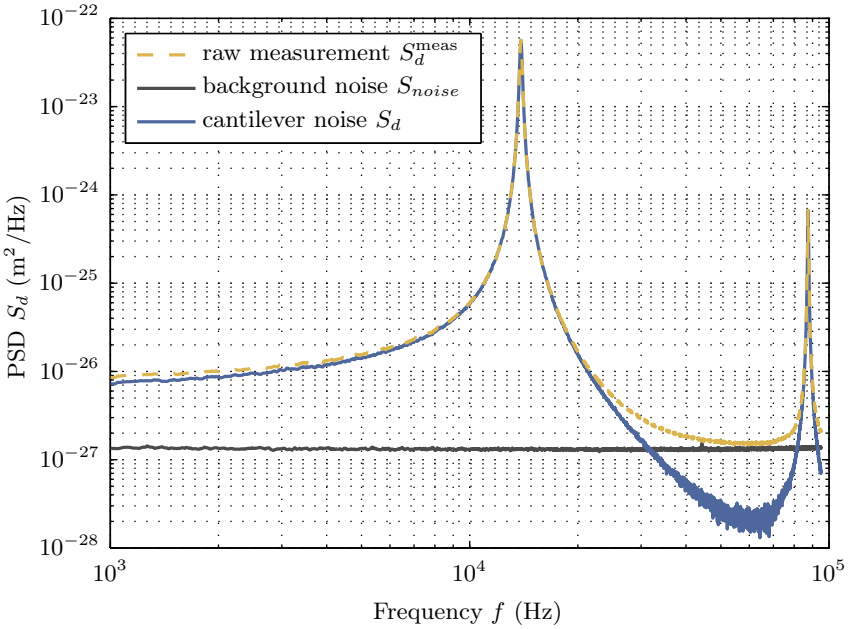

Figure 3.4 – *Power spectrum density (PSD) of deflexion of a* Budget Sensors *BS-Cont cantilever. The thermal noise at the free end of the cantilever is measured in a* 1 kHz *to* 100 kHz *range. We clearly see the two first flexural modes of the mechanical beam, well above the background noise of the apparatus acquired on a rigid mirror. The difference between the measurement and the background noise spectra gives a full view of the behavior of the thermal fluctuations of the cantilever in this frequency window.*

3.3.1 Viscous dissipation

Power spectrum density of deflexion

Using our differential interferometer in the Wollaston configuration (to have a perfectly calibrated measurement on the whole frequency range), we measure the PSD of thermal noise driven deflexion of the free end of a commercial AFM cantilever, *Budget Sensors* BS-Cont (data sheet is appendix D.2). We plot in figure 3.4 the measured PSD S_d^{meas}, and the background noise of the interferometer S_{noise}. We clearly see in this spectrum the two first modes of oscillation of the mechanical beam, around $f_1 = 14\,\text{kHz}$ and

$f_2 = 87\,\mathrm{kHz}$, but we also have a lot of information out of these resonances as S_d^{meas} is always strictly above S_{noise}. Since the actual mechanical thermal noise S_d is uncorrelated from the apparatus noise, we can simply subtract the latter to the measurement to estimate S_d:

$$S_d = S_d^{\mathrm{meas}} - S_{\mathrm{noise}} \tag{3.35}$$

Although the resulting spectrum is a bit noisy between the 2 first resonances (around 60 kHz), this trick allows us to fully resolve the mechanical thermal noise in the 1 kHz to 100 kHz range[2], with a resolution better than the background noise, down to $10^{-28}\,\mathrm{m}^2/\mathrm{Hz}$. The same measurement in a commercial AFM would yield much less information, as it would be limited to the resonances, and we would not have any information between them or at low frequency.

The nominal dimensions of the cantilever are: length $l = 450\,\mu\mathrm{m} \pm 10\,\mu\mathrm{m}$, width $w = 50\,\mu\mathrm{m} \pm 5\,\mu\mathrm{m}$, thickness $h = 2\,\mu\mathrm{m} \pm 1\,\mu\mathrm{m}$. It is made of monolithic silicon and is uncoated. In order to confront the experimental spectrum with Sader's model, we use tabulated values for the viscosity and the density of air, and for the density and Young's modulus of Silicon: $\eta_{\mathrm{air}} = 1.85 \times 10^{-5}\,\mathrm{kg{\cdot}m^{-1}s^{-1}}$, $\rho_{\mathrm{air}} = 1.19\,\mathrm{kg{\cdot}m^{-3}}$ (both at 25 °C), $\rho_{\mathrm{Si}} = 2340\,\mathrm{kg{\cdot}m^{-3}}$ and $E_{\mathrm{Si}} = 169\,\mathrm{GPa}$ (for the <110> crystalline orientation along the length of the AFM cantilever). The length and width of the cantilever were checked with an optical microscope, and the thickness is adjusted to match the first resonance frequency of the cantilever, which eventually leads to $l = 450\,\mu\mathrm{m}$, $w = 48\,\mu\mathrm{m}$, $h = 2.07\,\mu\mathrm{m}$.

The PSD computed from Sader's model, plotted in figure 3.5, agrees perfectly with the measurement. Both resonances are accurately reproduced, and low frequency and intermediate region are as well closely matched by the model. We stress here that the only parameter we have adjusted in the model is the thickness of the cantilever h, to match the actual frequencies of resonance. The Sader approach to describe the effect of the embedding fluid (air in our case) on the behavior of the cantilever turns out to be very good on the whole frequency range that is probed here. For comparison with a simpler model, we also fit both resonances with a SHO model and add the resulting spectra to provide an estimation of the full thermal noise spectrum. In figure 3.5, we see that the result is pertinent around the resonances, but departs from the measurement at low frequency and between

[2]The upper limit of the frequency range is due to physical limitation of our acquisition card at the time of the experiment (our current bound is several MHz), while the lower limit is chosen to avoid any low frequency environmental noise that may disturb the Wollaston configuration.

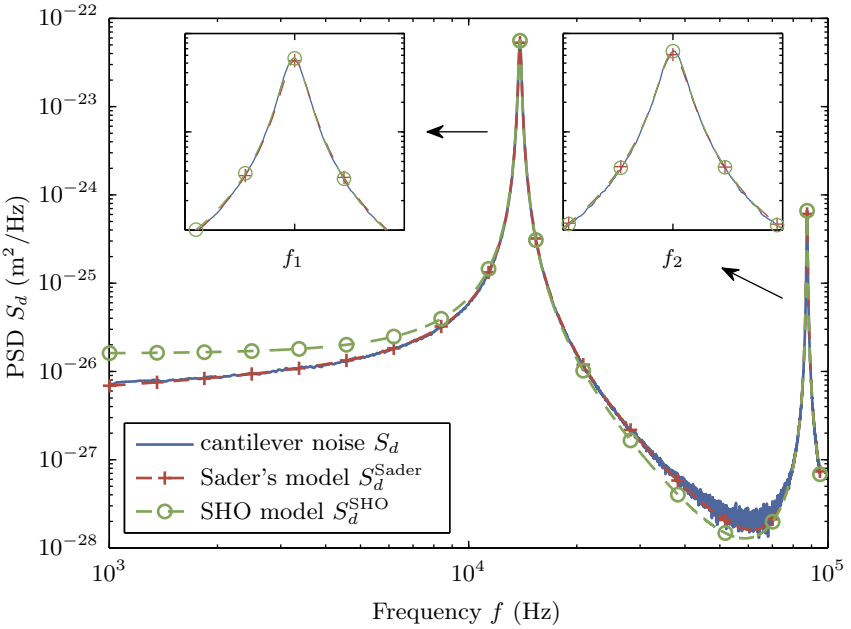

Figure 3.5 – *PSD of mechanical thermal noise of a* Budget Sensors *BS-Cont cantilever versus two different models: Sader's and the sum of the spectra of SHO fits for each resonance. The insets present zooms around the resonances. The thickness of the cantilever is the sole adjustment parameter in Sader's model, which matches the measurement on the full frequency range that is explored in this experiment.*

the resonances. It lacks the frequency dependence of inertial and viscous effects due to the fluid.

To emphasize the pertinency of the model for even higher order modes, we report in figure 3.6 a measurement up to 500 kHz on a similar cantilever, except for a gold coating that enhances its reflectivity and thus lowers the background noise. With Sader's approach (slightly modified to take into account the added mass due to the coating), we are able to closely match the experimental spectrum on the 4 modes that are visible in this frequency range.

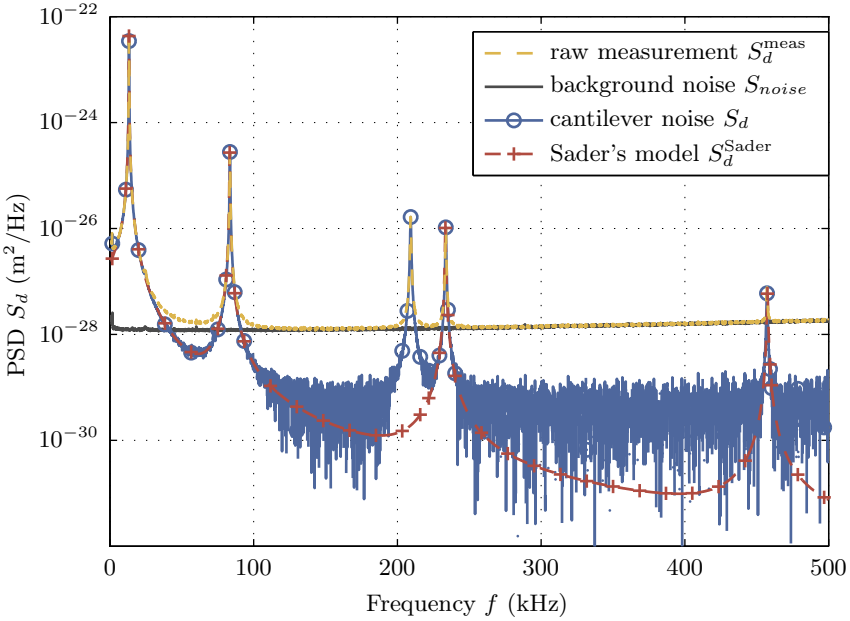

Figure 3.6 – *Power spectrum density (PSD) of the thermal noise driven deflexion at the free end of a BudgetSensors BS-Cont-GD cantilever. In the wide frequency range of this measurement, 4 flexural resonances are visible. Once the background noise has been subtracted, Sader's model does a very good job at reproducing the whole spectrum, except for an additional peak that corresponds to a resonant torsional mode.*

Mechanical response

We now use the bi-calcite configuration to measure precisely the low frequency spectrum of the thermal noise of the same AFM cantilever. This allows us to apply the Kramers-Kronig algorithm to the PSD limited to the first resonance, and reconstruct the mechanical response function G with a few Hz resolution. We plot in figure 3.7 the result of this process. The conservative part of the response function, $\mathrm{Re}(G)$, present the characteristic parabolic shape of an harmonic oscillator: the additional inertia due to the fluid is negligible in air. However, the dissipative part, $\mathrm{Im}(G)$, cannot be simply modeled with a frequency independent damping term. Indeed, it presents a non linear shape that is well described by Sader's model. The

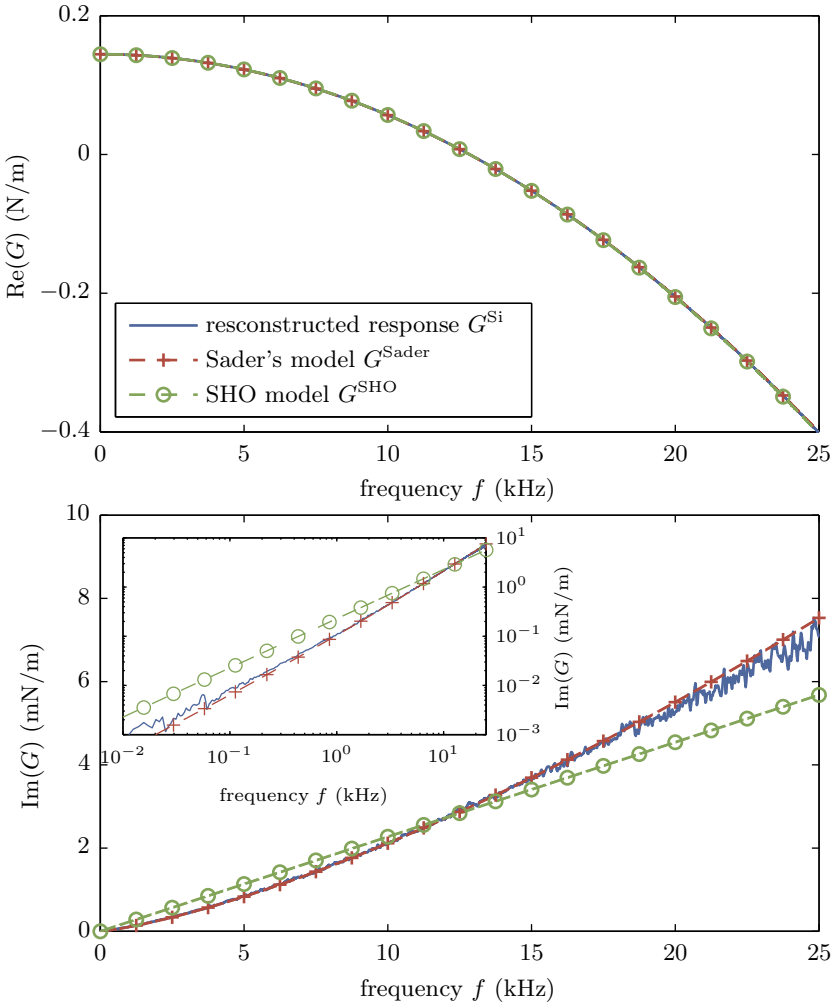

Figure 3.7 – *Mechanical response function of an uncoated AFM cantilever.* G^{Si} *is reconstructed from the thermal noise measurement with the Kramers-Kronig algorithm. It is accurately described by Sader's model, whereas a SHO approach fails to reproduce the non-linear frequency dependence of the dissipative part of the response. The log-log scale in the inset emphasize the pertinency of Sader's description down to low frequencies.*

log-log scale of the inset demonstrate the quality of the model down to low frequencies.

The reconstruction of the response using the Kramers Kronig algorithm leads to very interesting physical data: the mechanical behavior is easy to interpret knowing the response function. For instance, experiments on this simple silicon cantilever in air allow us to validate Sader's model with a great precision on a large frequency range, that is not limited to resonance frequencies on the system. Our high sensitivity interferometer is a key tool to enable this approach: the input measurement data is a wide frequency range thermal noise spectrum, not limited by the instrument intrinsic noise. We use this innovative approach to present in the next section an original study of a low frequency dissipation process in coated cantilevers.

3.3.2 Viscoelastic dissipation

We published the results presented in this section in reference [104], and refer the reader to this article for the complete presentation of our results. We will present here the main findings, focusing on viscoelastic dissipation.

In chapter 2, we presented as an illustration of the high precision of our interferometer the thermal noise spectrum of a golden coated cantilever (figure 2.10). A striking difference between this measurement and that of the previous part on raw silicon cantilevers is the low frequency behavior: a slow decrease of noise for an uncoated beam versus a $1/f$ like increase for a coated one. In figure 3.8, we plot the PSD of such a measurement on a *Budget Sensors* Cont-GB (data sheet in appendix D.1), acquired with our apparatus operating in the bi-calcite configuration to lower any external disturbances at low frequency. We limit the displayed frequency range to the first resonance only. The background noise of the interferometer is far below the measured spectrum at low frequency. We carefully checked that the low frequency trend was not due to any artifact linked to the experimental process, namely the interaction of the sensing light with the reflective coating:

- We measured the frequency response function $\chi_{dI}(f)$ of the deflexion d to the light intensity I by modulating by a few percent the laser power [130]. In standard measuring conditions, I is kept constant but presents small fluctuations around its mean value, which will thus trigger some motion of the cantilever. This light induced deflexion noise $S_d^{\text{light}}(f)$ can be estimated using the PSD S_I of light intensity and the response function χ_{dI}: $S_d^{\text{light}} = |\chi_{dI}|^2 S_I$. It is at least 3 orders of magnitude smaller than the observed thermal noise.

- On coated cantilevers, if we decrease the interferometer light intensity by a factor of 10, the shot noise will rise, but will still be much lower than the measured thermal noise of the cantilever at low frequency. Except for the rise of the background noise, the PSD $S_d(f)$ is not affected by such a drastic change in the laser power, notably at low frequency.

- We measured the thermal noise of some cantilevers which were coated on one side only. Except for a lower background noise when measuring on the coated surface (due to a higher reflectivity and thus a lower shot noise), the PSD $S_d(f)$ does not change when the cantilever is turned upside down.

- The $1/f$ like behavior is reproducible with cantilevers from various manufacturers and with various metallic coatings, although the stronger effect is obtained with gold.

The $1/f$ like behavior of the thermal noise thus appears to be a robust characteristic of coated cantilevers. We know from the FDT that this extra noise with respect to uncoated cantilevers points towards an additional dissipation process in the mechanical response. To increase the relative importance of this phenomenon, we performed a series of measurements in vacuum: when dissipation due to the surrounding atmosphere vanishes, damping comes only from internal processes in the cantilever. The thermal noise spectrum in vacuum is superposed with the one in air on figure 3.8. The resonance is much sharper in vacuum, corresponding to a 40 time increase of the quality factor. The $1/f$ like trend is preserved and even more visible close to the resonance thanks to the absence of dissipation in air.

We apply the Kramers Kronig algorithm to reconstruct the cantilever mechanical response function G^{air} and G^{vacuum} from the measured spectra S_d^{air} and S_d^{vacuum} in air and vacuum environments. Figure 3.9 reports the result of this process. The dissipative part of the response $\text{Im}(G^{\text{vacuum}})$ is almost frequency independent: it decreases only by a factor 3 when the frequency spans more than 3 decades. It can be fitted by a power law with a small exponent: $\text{Im}\left[G^{\text{vacuum}}(\omega)\right] = \mathcal{G}_i\omega^{\alpha}$, with $\alpha = -0.11$. At atmospheric pressure, dissipation at low frequency is unchanged, but increases strongly above 500 Hz to recover a classic viscous profile, well described by Sader's model. The full shape of the curve is perfectly fitted by the sum of the power law $\mathcal{G}_i\omega^{\alpha}$ and of the viscous contribution, even in the transition between the two regimes.

To interpret this measurement, let us recall the expression of the ex-

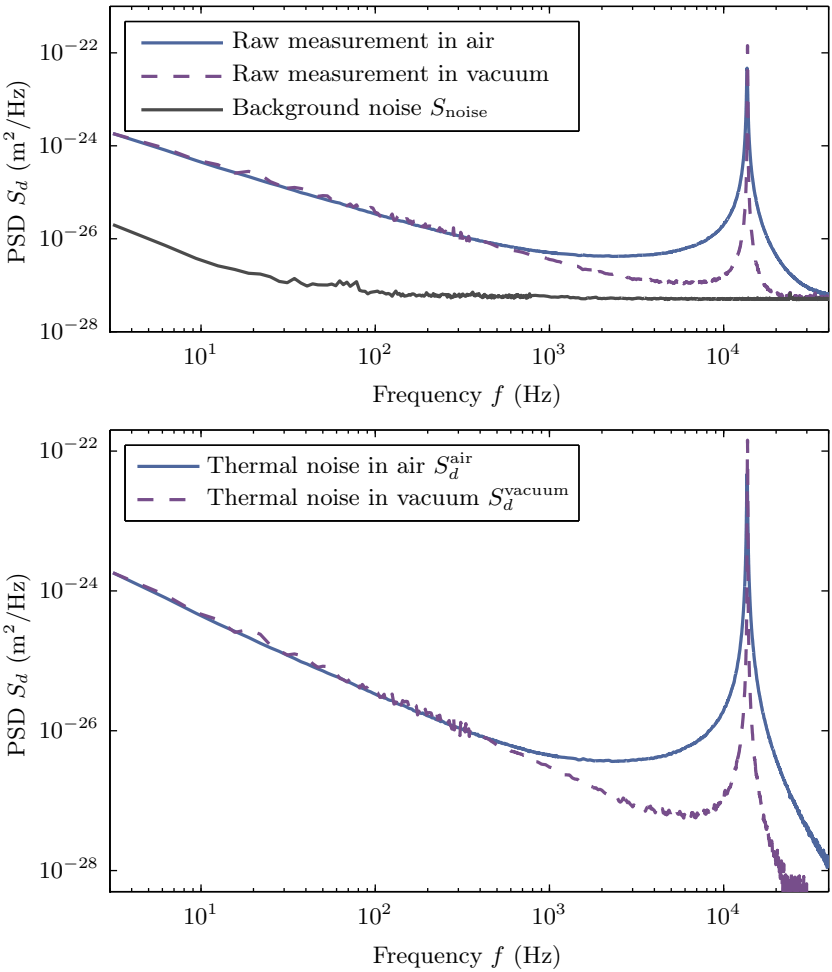

Figure 3.8 – *Power Spectrum Density (PSD) of thermal noise induced fluctuations for a golden coated cantilever at atmospheric pressure and in vacuum. The raw measurements, plotted on the top graph, are well above the background noise of the interferometer. In the bottom plot, this background noise has been subtracted to estimate the actual mechanical thermal noise. The low frequency behavior is exactly the same. This part of the spectrum doesn't depend on the viscous damping due to the surrounding atmosphere, and is therefore related to a dissipation in the cantilever itself.*

pected mechanical response for the amplitude of the first flexural mode

$$G_1(\omega) = k_1 - m_{\text{eff}}(\omega)\omega^2 - i\gamma_{\text{eff}}(\omega)\omega \tag{3.36}$$

In vacuum, $m_{\text{eff}}(\omega) = m$ and $\gamma_{\text{eff}}(\omega) = 0$, therefore $\text{Im}\,[G^{\text{vacuum}}(\omega)] = \text{Im}(k_1)$. The simplest interpretation of the observation is thus to suppose that the stiffness has a non zero imaginary (dissipative) part, that we directly measure with our technique. A complex Young's modulus, frequency independent, is commonly used to describe dissipation in solids [78, 124, 140], with a loss angle[3] that is usually very small for metals (of order 10^{-3} or less). We measure here $\arg(G^{\text{vacuum}}) \sim 5 \times 10^{-4}$. However, our wide frequency range allows us to refine the model and observe the small frequency dependance of $\text{Im}(k_1) = \mathcal{G}_i\omega^\alpha$.

We know from Kramers-Kronig relations that if k_1 has an imaginary part, it has to be frequency dependent. The power law dependence observed for the imaginary part leads to the full knowledge of the real part as well, with no adjustable parameters (except the static spring constant κ_1): from Kramers-Kronig relations, we compute

$$k_1(\omega) = \kappa_1 - \kappa_J \left(i\frac{\omega}{\omega_0}\right)^\alpha \tag{3.37}$$

where κ_J is real. The detailed derivation is given is appendix B.1. In dielectric measurements, such a frequency dependence has been introduced by Jonscher [74] and is used to describe a pseudo-conductivity (divergence of the dissipative part of the dielectric constant as $\epsilon'' \propto \omega^\alpha$ with $-1 < \alpha < 0$, pure conductivity corresponding to $\alpha = -1$). The two parameters describing the frequency behavior are extracted from the fit on the imaginary part of the vacuum measurement $\text{Im}\,[G^{\text{vacuum}}(\omega)]$: for this particular cantilever, we measure $\kappa_J = 7 \times 10^{-4}\,\text{N}\cdot\text{m}^{-1}$ and $\alpha = -0.11$.

The zoom at low frequency in the inset of Fig. 3.9 shows an unexpected behavior of $\text{Re}(G)$ as f goes to 0: instead of the constant trend predicted by the SHO or Sader's models, it presents a maximum and a steep decrease (of small amplitude though). At low frequency inertial effects are negligible, thus the real part of G is directly the real part of the spring constant: $\text{Re}(G(\omega)) \simeq \text{Re}(k_1(\omega)) = \kappa_1 - \kappa_J \cos(\alpha\pi/2)(\omega/\omega_0)^\alpha$. κ_J and α are already fixed by the fit on the imaginary part of the reconstructed function $\text{Im}(G(\omega))$, hence we do not need to introduce any new adjustable parameters to closely match the observations on the real part as illustrated in the inset of Figure 3.9.

[3]The loss angle or loss tangent is defined by the argument of the complex Young's modulus.

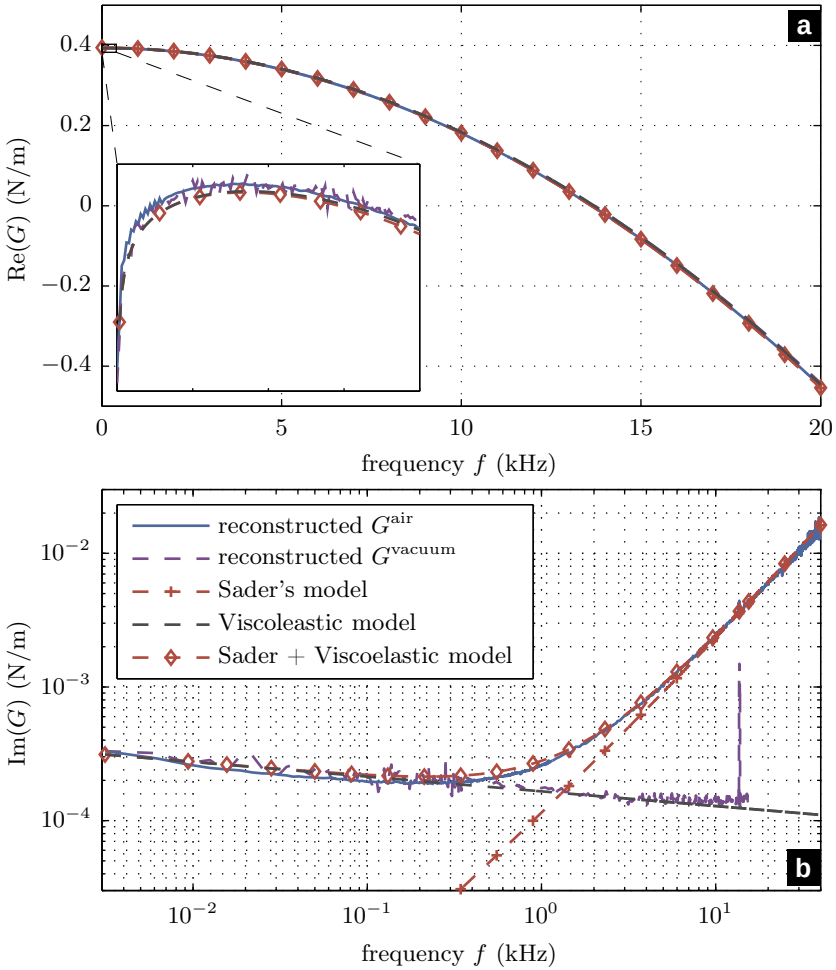

Figure 3.9 – *Reconstructed mechanical response function of a golden coated cantilever in air and in vacuum. (**a**) Real part. The inset is a zoom around $f = 0$ (400 Hz wide and $10^{-3}\,\mathrm{N{\cdot}m^{-1}}$ high). (**b**) Imaginary part. The viscoelastic damping in the cantilever is evidenced by the vacuum measurement, and can be fitted by a power law of frequency with a small exponent $\alpha = -0.11$. The low frequency behavior of $\mathrm{Re}(G)$ for the viscoelastic model is deduced from Kramers-Kronig relations applied to the fit of $\mathrm{Im}(G)$, it matches well the experimental data. Sader's model describes accurately the dissipation in air for large f, and the sum of the two damping processes matches the measurements in air on the whole frequency window.*

3.3.3 Dissipation processes: summary

We have measured the power spectrum density (PSD) of thermal noise induced deflexion of coated and uncoated micro-cantilevers at atmospheric pressure and down to 10^{-5} mbar. Thanks to the sensitivity of our apparatus, we resolve the spectrum completely from very low frequencies to beyond the resonance. The common simple harmonic oscillator model with viscous damping is clearly inadequate to describe the off resonance fluctuations, especially of coated cantilevers. At low frequency, the thermal noise of those shows a $1/f$ like trend, which can be seen as the signature of a viscoelastic dissipation in the cantilever. To go further than simple observations, we use the Fluctuation-Dissipation Theorem and the Kramers-Kronig relations to rebuild the complete response function of the cantilever from the measured PSD. A simple power law is found to describe accurately the frequency dependence of the viscoelastic dissipation, and a consistent model can be proposed to fit tightly all the experimental data: beyond the simple harmonic oscillator approximation, it includes Sader's approach to describe the coupling with the surrounding atmosphere and a mechanical Jonscher like term to account for viscoelasticity.

Let us emphasize a important point here: the use of FDT and Kramers-Kronig relations to rebuilt the mechanical response function of the system is based on very general hypotheses (linear response, causality, thermal equilibrium). Our measurements are thus free of any hypothesis on the dissipation processes in the cantilever, and the viscoelastic model we eventually propose is purely phenomenological. Although viscoelasticity or anelasticity had already been used in several models to account for observations, it has mostly been limited to the resonances of oscillators and to their quality factors. Our experiment offers a complete determination of the viscoelastic properties of a coated micro-cantilever, with quantitative measurement of its amplitude and frequency dependence on a wide spectral range.

The use of thermal noise is a key point of our approach, since we don't need to determine exactly the transfer function of the external forcing method which is usually necessary to measure a response function. We get an excellent resolution with measurements of mechanical loss tangents smaller than 10^{-3}. Even such a small dissipation has some consequences on the operation of micro-cantilevers, notably when they are used in vacuum: it gives an upper bound to the quality factor of the resonances. Even if we don't explain the physical origin of the viscoelasticity due to the coating, we can quantify it and our measurements should be useful in the perspective of testing models of internal friction, eventually leading to improved coating

procedures and better performance of cantilever based sensors. Our method would also be suited to study other type of coatings, such as those implied in chemical or biological sensors, alone or linked to target molecules.

3.4 Beyond first flexural mode: thermal noise mapping

When translating laterally the focusing lens L_0 of the interferometer, we change the position of both reference and sensing laser beams over the sensor. In the Wollaston configuration of the interferometer, the reference laser beam is reflected by the chip holding the cantilever. This reference mirror is very large, we can therefore safely explore the cantilever surface without bothering about the reference beam precise position. At each point on the cantilever, we are thus able to calibrate our interferometer and then acquire a thermal noise spectrum. It results in a calibrated measurement of deflexion fluctuations both in space and frequency, that we can confront to the Euler-Bernoulli predictions.

We first performed a manual scan close to the main axis of a cantilever, to compare the thermal noise spatial and spectral distribution to the expected behavior of the normal modes. This work, conducted in association with Bruno Tiribilli (invited professor by the ENS Lyon in 2008), has been published in reference [107]. It can be used as a base to precisely measure the spring constant of a cantilever. After automating the translation of the focusing lens L_0, we were recently able to map the thermal noise over the full surface of the sensor, and will present in a second part the first outcome of these experiments.

3.4.1 Flexural modes and stiffness calibration

We use a contact cantilever from *Budget Sensors* with gold coating (Cont-GB, data sheet in appendix D.1), and record 30 calibrated noise spectra, every $15\,\mu$m along the $450\,\mu$m long mechanical beam. The background noise is as low as $3 \times 10^{-28}\,\mathrm{m^2/Hz}$ in the frequency range from 1 kHz to 800 kHz. The focused beam size on the cantilever is around $10\,\mu$m, ensuring a good spatial resolution along the cantilever length. At every position x we measure the deflexion $d(x,t)$ produced by the thermal excitation of the cantilever and we evaluate the PSD $S_d(x,f)$. The complete set of results is reported in figure 3.10 as a 3D representation. The first four oscillation modes can be clearly seen with their respective number of nodes. Two

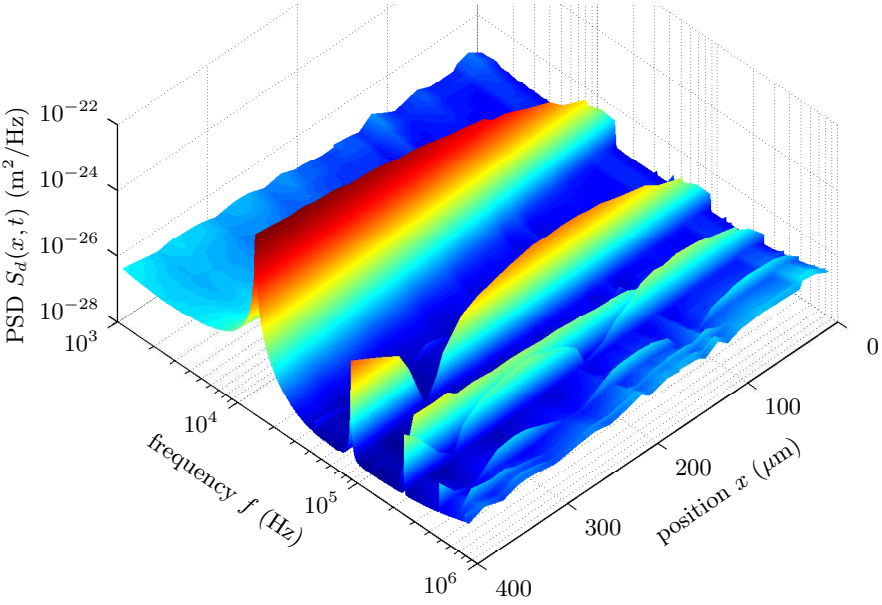

Figure 3.10 – *Power Spectrum Density (PSD) $S_d(x, f)$ of thermal noise induced deflexion as a function of frequency f and position x along the cantilever. The first 4 normal modes are clearly visible, with a vanishing amplitude toward the clamped extremity of the mechanical beam and the nodes of each mode. Another vibration peak with no nodes is also visible close to the third mode, it is attributed to the first mode in torsion.*

further peaks can be noted, the first at about 220 kHz and a second, of smaller amplitude, at 790 kHz, that we attribute to the first and second torsional modes.

For a quantitative characterization of the shape of the modes we determine the rms amplitude of each resonance $\langle d_n^2(x)\rangle$ as a function of the position x, by integrating the PSD in a convenient frequency interval $2\Delta f$ around each peak:

$$\langle d_n^2(x)\rangle = \int_{f_n-\Delta f}^{f_n+\Delta f} S_d(x,f)\mathrm{d}f \tag{3.38}$$

This quantity is computed directly from the experimental spectra, without any fitting process of the resonances. We anyway take care to subtract the

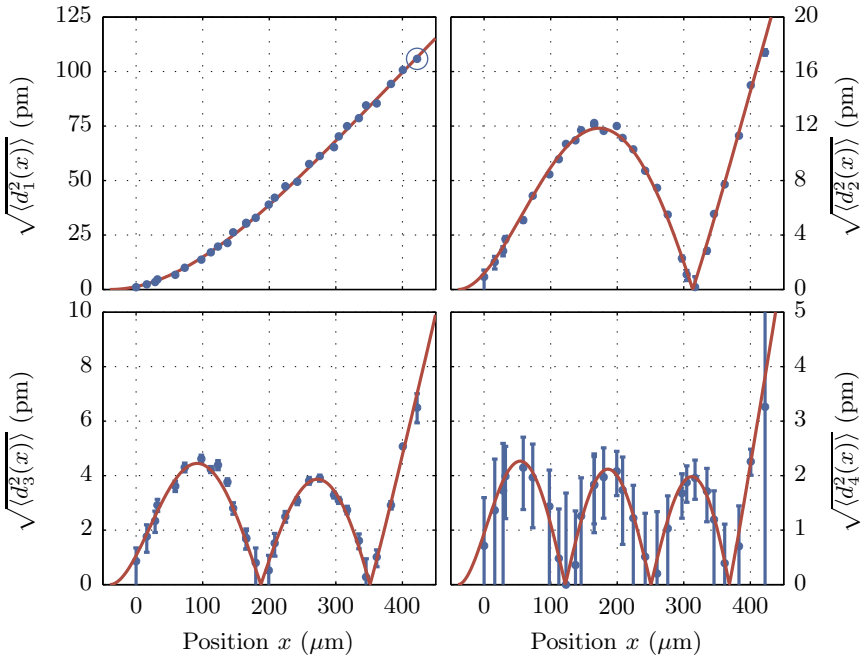

Figure 3.11 – *Amplitude of thermal noise for the first 4 flexural modes along the cantilever. Errors bars correspond to the equivalent noise of the detection system in the bandwidth chosen around each resonance (a very conservative estimation of uncertainty). The simultaneous fit (red curves) of the 4 resonances with the normal modes shapes is excellent and leads to a precise measurement of the stiffness of the cantilever. The common calibration method for the spring constant considers only the value of $d_1^2(l)$, the circled point in the upper graph.*

contribution of the background noise of the interferometer. We also compensate for the finite integration range in frequency. This last correction is done by supposing that the ratio of the noise in the considered interval to the total noise is equal to that of an equivalent simple harmonic oscillator [105]. Experimental data computed this way is plotted on figure 3.11. Error bars correspond to the equivalent noise of the detection system in the bandwidth chosen around each resonance (a very conservative estimation of uncertainty).

According to equation 3.22, we should have

$$\left\langle \mathrm{d}_n^2(x) \right\rangle = \left\langle \beta_n^2 \right\rangle \frac{1}{l} \left| \phi_n(x) \right|^2 \tag{3.39}$$

where β_n and ϕ_n are respectively the amplitude and spatial shape of mode n, and l the length of the cantilever. Using the equipartition theorem for each mode of stiffness $k_n = \alpha_n^4 k/3$, we know that $\left\langle \beta_n^2 \right\rangle = k_B T/k_n$, we thus should have

$$\sqrt{\langle d_n^2(x) \rangle} = \sqrt{\frac{3}{\alpha_n^4} \frac{k_B T}{kl}} \left| \phi_n(x) \right| \tag{3.40}$$

where α_n are the spatial eigenvalues of the Euler-Bernoulli clamped-free beam (see equation 3.8). We fit the data with this functional form using 3 adjustable parameters: the clamping position (origin of x), the length l and the static spring constant k of the cantilever. We realize the fit on the rms amplitude *simultaneously* on the 4 modes. The red curves in figure 3.11 represent the result of this adjustment, in good agreement for all modes. The best fit values are: $l = (450 \pm 5)\mu$m and $k = (0.376 \pm 0.015)$N/m. These length and stiffness are compatible with the values provided by the manufacturer ($l = (450 \pm 10)\mu$m and k from 0.07 N/m to 0.4 N/m).

It is worth noting that the accuracy of our instrument provides a precise measurement of the thermal noise driven deflexion along the cantilever length and allows to verify the Euler-Bernoulli model for the micro-lever. Furthermore this multi-mode approach provides a more reliable way to estimate the spring constant of a cantilever with respect to the standard thermal noise calibration method [26], which is limited to the integral of the first mode only and just at the cantilever free end (circled point in Fig. 3.11). Actually a precise measurement of stiffness could be obtained from the first 3 modes only, the presence of the nodes providing a favorable constraint to the fitting process. Moreover, the use of the interferometric set-up allows one to avoid the calibration of the segmented photodiode response as in the classical optical lever readout scheme: this step implies a contact between the AFM tip and a hard sample which is translated of a known amount, a process that may be undesirable to preserve the probe's sharpness or its coating. Our calibration method leaves only a small 4 % uncertainty on the spring constant value for the cantilever used here (confidence interval corresponding to one standard deviation estimated during the linear least square fitting process).

Using the integration step around resonance (equation 3.38), we hide any information concerning the dissipation of each mode. In reference [107], we

also compute the quality factor of each resonance, and compare the data with the prediction of Sader's model. A good agreement is reached for the first three resonances, but at the highest frequency a deviation is observed: dissipation is lower than foreseen by Sader's model. This behavior was already observed by Maali and co-workers [91]. This deviation is expected since the original Sader model neglects the 3D nature of the fluid flowing around the cantilever, an effect increasing with the mode number [119]. In an extended model by Sader and co-workers [136], such a correction is also observed in the same direction as in our observation. We refer the reader to reference [107] for further details.

3.4.2 Thermal noise maps to measure elastic moduli

In order to explore torsional modes as well as longitudinal modes, we choose a larger cantilever to enhance the relative lateral precision of the measurement. We use two *NanoWorld* Arrow TL cantilevers, one with and one without gold coating. Their nominal geometry is: length $l = 500\,\mu$m, width $w = 100\,\mu$m and height $h = 1\,\mu$m, and for the coated one, top side layers of 5 nm of titanium and of 30 nm of gold (manufacturer datasheet in appendix D.3). The surface of the cantilever is scanned by a $16\,\mu$m wide sensing beam[4], with $3\,\mu$m lateral and $5\,\mu$m longitudinal steps. At each position, we calibrate the interferometer (using a lateral driving of the Wollaston prism), then record a power spectrum density of thermal noise up to 1 MHz. Up to 16 mechanical resonances can be noticed in this spectrum for the raw cantilever, and 14 for the gold coated one (see example on figure 3.12). Following the procedure of previous part, we integrate the PSD around each resonance to access its rms amplitude $\langle d_n^2(x,y)\rangle$. We take care to subtract the contribution of the background noise and to account for the finite integration range. We plot the resulting map of thermal noise for the resonances in figure 3.13 for the raw cantilever, and in figure 3.14 for the coated one. We easily identify 8 flexural modes and 6 torsional modes from theses maps, plus two high frequency resonances of more complex spatial shape for the raw lever. The high precision of the interferometer allows once again to access extremely small fluctuations, with rms amplitudes of only a few pm.

We will use theses measurements to extract the mechanical properties of the cantilever, namely its Young's modulus E and shear modulus S. Our thermal noise maps are very similar to results obtained from vibrometry experiments, where one drives the system at its resonance frequencies and measure the deformation field. The small difference is that we access only

[4] The $1/e^2$ radius of the gaussian beam is 8 nm

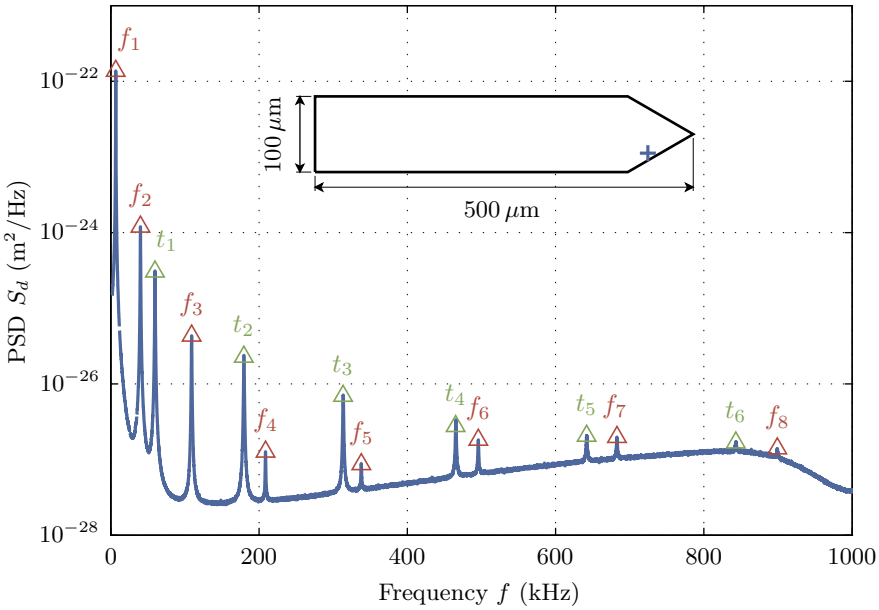

Figure 3.12 – *Power spectrum density of thermal noise induced fluctuations on a* NanoWorld *Arrow TL-Au cantilever. This measurement corresponds to the sensing position indicated by a blue cross on the cantilever sketch. We notice 8 flexural (f_1 to f_8) and 6 torsional (t_1 to t_6) mechanical resonances that we study as a function of the spatial position on the cantilever.*

the rms value of the deflexion with thermal noise. Anyway, we can conduct an analysis of the dispersion relations linking the spatial wavelengths to the resonance frequencies, as is usually done in vibrometry to infer the mechanical properties of the cantilever.

Measuring E through flexural modes

Let us first focus on the flexural modes, the noise of which is described in the Euler-Bernoulli framework by equation 3.39. Fitting the spatial shape of the noise with eigenmodes $\phi_n(x)$, we extract the spatial wave number $\kappa_n = \alpha_n/l$ for each mode. Due to the triangular end of the cantilever, the boundary condition at the free extremity of the cantilever is more complex than in the classic case of a rectangular cantilever. This leads to an effective length

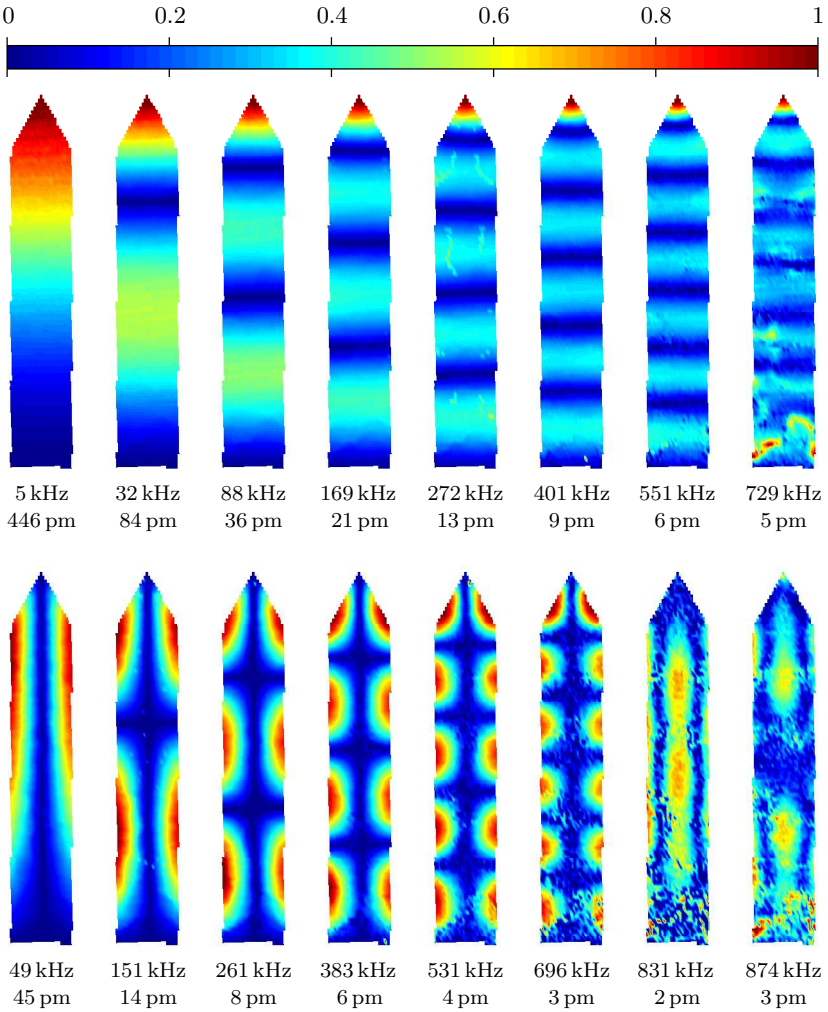

Figure 3.13 – *Thermal noise mapping on a* $100\,\mu\text{m} \times 500\,\mu\text{m}$ *raw silicon cantilever. We extract from the PSD measured at each point the rms amplitude of 16 different modes, and plot those using a color coded amplitude map (color bar on top of the figure). The resonant frequency and full scale amplitude is given below each map. We easily identify 8 flexural modes and 6 torsional modes from theses maps, plus two high frequency resonances of more complex spatial shape.*

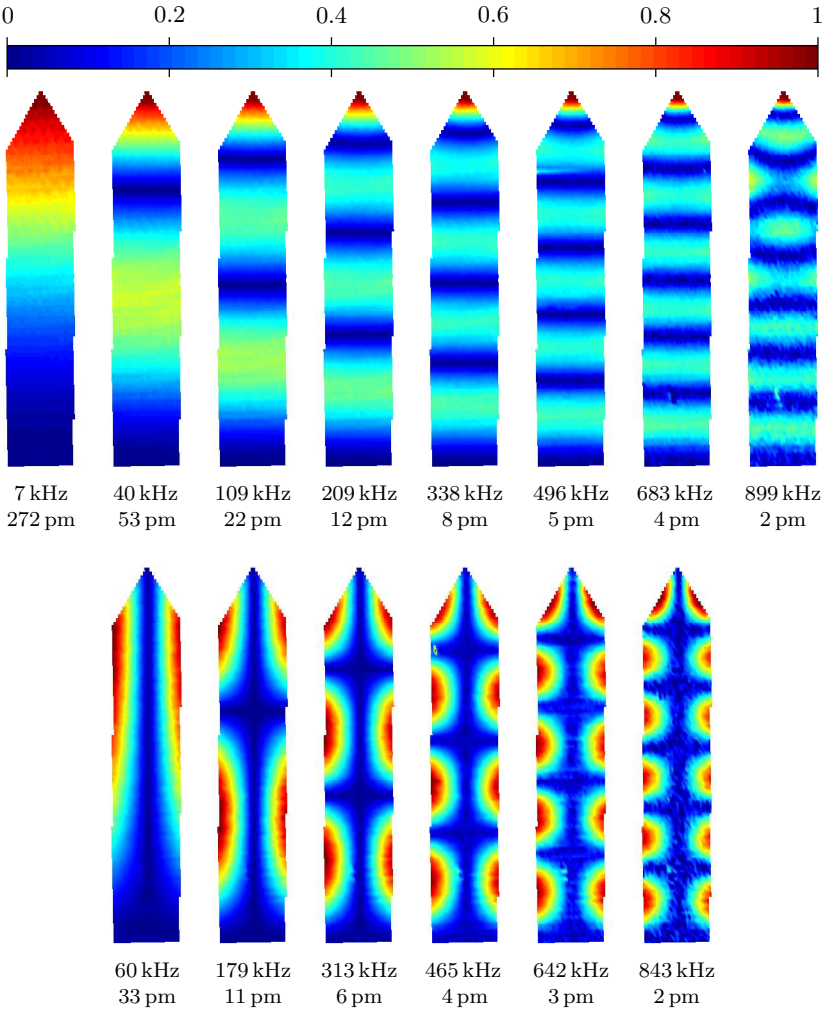

Figure 3.14 – *Thermal noise mapping on a* $100\,\mu\text{m} \times 500\,\mu\text{m}$ *golden coated silicon cantilever. We extract from the PSD measured at each point the rms amplitude of 14 different modes, and plot those using a color coded amplitude map (color bar on top of the figure). The resonant frequency and full scale amplitude is given below each map. We easily identify 8 flexural modes and 6 torsional modes from theses maps. The highest order flexural mode measured show evidence of a non uniform deflexion across the width close to the triangular free end of the cantilever.*

$l_{\text{eff}}(n)$ that is slightly mode dependent: using independent fits for each resonance, $l_{\text{eff}}(n)$ is found to grow from 455 μm to 490 μm while the mode number n rises from 1 to 8. The spatial wave number κ_n (or equivalently the effective length $l_{\text{eff}}(n)$) is linked to the resonance frequency by the dispersion relation (equation 3.9), that we rewrite here as a function of the cantilever geometrical and physical parameters:

$$m\omega_n^2 = k_n \tag{3.41}$$

$$\rho\omega_n^2 = E\frac{h^2}{12}\kappa_n^4 \tag{3.42}$$

with ρ the density of the cantilever. This dispersion relation is valid on the rectangular section of the cantilever, and thus does not suffer from the ill known boundary condition at the triangular end. The wave number κ_n is measured from a fit on this rectangular part only and is therefore robust to this boundary condition issue (except for the first mode which has no nodes). Using tabulated value of density for silicon (or an adequately weighted average of material density for the coated cantilever), and measured values of κ_n and ω_n, this relation enables measurement of E, provided the cantilever thickness h is known.

Our measurement provides an extra information with respect to classic vibrometry: the amplitude of the modes. Indeed, the coupling between the driving force and the deflexion of the cantilever is unknown in vibrometry, thus the amplitude is not relevant. Driving is just tuned for oscillations to be in the useful range of the device. In contrast, thermal noise driving leads to predictable mode amplitudes thanks to the FDT. Let us rewrite equation 3.39 using the normalization of the eigenmode ϕ_n:

$$\frac{1}{wl}\iint \mathrm{d}x\mathrm{d}y\,\left\langle d_n^2(x,y)\right\rangle = \left\langle \beta_n^2\right\rangle = \frac{k_B T}{k_n} \tag{3.43}$$

This quantity can easily be evaluated from our measurement data, leading to an experimental measurement of the stiffness k_n of each flexural mode. The resonances frequencies being precisely known, the relation $m\omega_n^2 = k_n$ directly leads to the measurement of m, the oscillator mass. This evaluation leads to a slightly mode dependent effective mass $m_{\text{eff}}(n)$, in contrast to prediction of the Euler-Bernouilli model. The contribution of the fluid, evaluated with Sader's model, cannot account for this observation. We interpret this as an effect of the ill defined boundary condition at the triangular end, and that the effective length $l_{\text{eff}}(n)$ should be considered: $m_{\text{eff}}(n) = \rho l_{\text{eff}}(n) wh$. The width w of the cantilever can be measured with a good precision using an optical microscope, thus the thickness

h can be inferred from the thermal noise amplitude: we finally measure $h = (0.78 \pm 0.03)\,\mu$m for the raw cantilever, and $h = (1.08 \pm 0.06)\,\mu$m for the coated one (mean value and incertitude correspond to the mean and standard deviation of the first 6 resonances). Using this value of h and dispersion relation 3.42, we eventually reach an estimation of Young's modulus E of our cantilevers, that we plot in figure 3.17. Within the experimental incertitude, E is not frequency dependent and its value is $E = (168 \pm 7)$ GPa (raw cantilever) or $E = (169 \pm 11)$ GPa (coated cantilever). These results are in perfect agreement with the tabulated value of 169 GPa for Si <110>, the crystalline orientation along the length of AFM cantilever.

Measuring S through torsional modes

We now study the torsional modes, using a very similar approach. The torsion of the cantilever can be described by the angular deflexion $\theta(x)$ of the cantilever around its longitudinal axis, the deflexion simply being $d(x, y, t) = y\theta(x, t)$. In the classic theory attributed to Saint-Venant [40], the equation of motion is [82, 89]:

$$I\frac{\partial^2\theta(x,t)}{\partial t^2} + Cl^2\frac{\partial^2\theta(x,t)}{\partial x^2} = l\left(\mathcal{M}_{\text{ext}}(x,t) + \mathcal{M}_{\text{hydro}}(x,t)\right) \tag{3.44}$$

where $I = mw^2/12$ is the inertial moment of the beam, $C = Swh^3/3l$ its torsional stiffness (S is the shear modulus), and $\mathcal{M}_{\text{ext}}$ and $\mathcal{M}_{\text{hydro}}$ are the external and hydrodynamic twisting moments per unit length. All moments are defined around the longitudinal axis. The expression of I and C are given in the limit $h \ll w$. If right hand side term of equation 3.44 is zero, the solutions are the sinusoidal normal modes $\phi_n^t(x)$ matching the boundary conditions of a clamped-free beam:

$$\phi_n^t(x) = \kappa_n^t l \sin\left(\kappa_n^t x\right) \tag{3.45}$$

where the wave number κ_n^t of mode n is $\kappa_n^t = (2n-1)\pi/2l$. The pulsations ω_n^t of these normal modes are ruled by the dispersion equations:

$$I{\omega_n^t}^2 = C\left(\kappa_n^t l\right)^2 = C_n \tag{3.46}$$

$$\rho w^2 {\omega_n^t}^2 = 4Sh^2\left(\kappa_n^t\right)^2 \tag{3.47}$$

From the measured thermal noise maps of torsional modes $\left\langle d_n(x,y)^2\right\rangle$, we first compute the torsion noise $\left\langle \theta_n(x)^2\right\rangle$ from a fit of the slope along y, for each mode n and each longitudinal position x. This first step is illustrated in figure 3.15. Then, fitting the spatial shape of the torsion noise

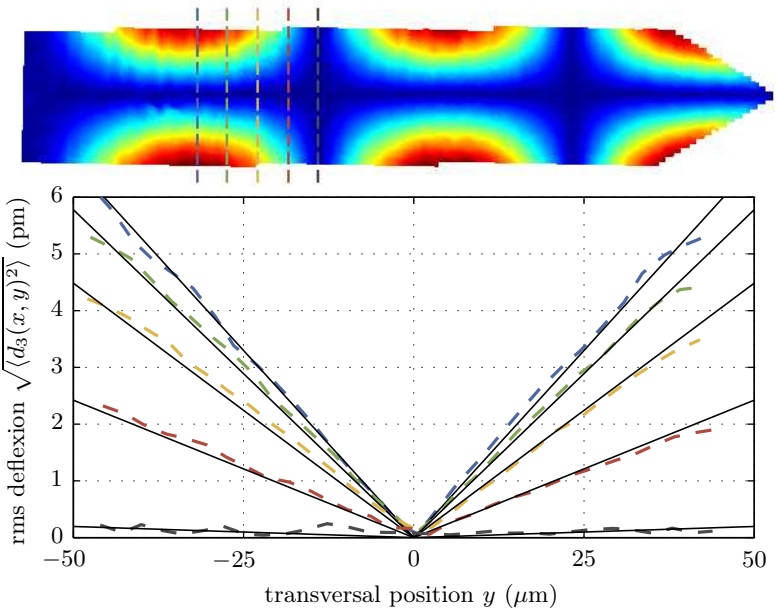

Figure 3.15 – *From the thermal noise maps of torsional modes, we extract at each position x along the cantilever the torsion rms noise $\langle \theta_n(x)^2 \rangle$ from a fit of the slope along the transversal coordinate y. We illustrate this process in this figure with 5 transversal cuts of the map of a third mode (the colored dashed curves correspond to the transversal lines plotted on the top thermal noise map), superposed with the linear fits leading to the slope (thin black lines).*

with eigenmodes $\phi_n^t(x)$, we extract the spatial wave number κ_n^t for each mode. This second step, illustrated in figure 3.16, validates Saint-Venant's mode shape for torsional modes: the sine function of the modes $\phi_n^t(x)$ perfectly matches the experimental data, except at the triangular end of the cantilever. Again, the boundary condition at the free extremity of the cantilever is more complex than in the classic case of a rectangular cantilever, leading to an effective length $l_{\text{eff}}^t(n)$ that is slightly mode dependent: using independent fits for each resonance, $l_{\text{eff}}^t(n)$ is found to grow from 415 μm to 435 μm while the mode number n rises from 1 to 6. The dispersion relation 3.47 is valid on the rectangular section of the cantilever, and thus does not suffer from the ill known boundary condition at the triangular

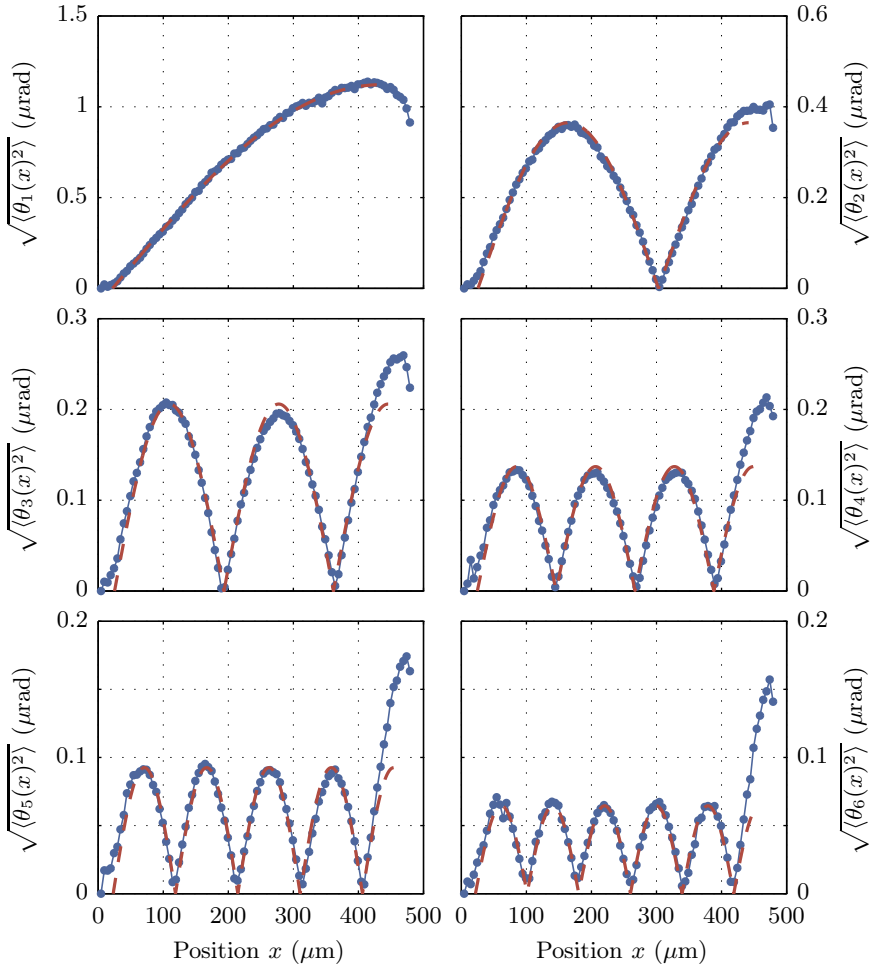

Figure 3.16 – *Amplitude of thermal noise for the first 6 torsional modes along the raw silicon cantilever. Fits with Saint-Venant's prediction for the mode shape $\phi_n^t(x)$ (red) match closely the experimental data (blue) in the rectangular part of the cantilever ($x < 410\,\mu$m), and only depart from it at the triangular extremity.*

end. The wave number κ_n^t is measured with a fit on this rectangular part only ($x < 410\,\mu$m) and is therefore robust to this boundary condition issue (except for the first mode which has no nodes). Using the tabulated value of density for silicon, and the measured values of κ_n^t and ω_n^t, this relation enables the measurement of the shear modulus S, provided the cantilever thickness to width ratio h/w is known.

Just as for the flexural modes, the amplitude of torsional modes provides an additional information about the system. Let us decompose $\theta(x,t)$ and $\mathcal{M}_{\text{ext}}(x,t)$ on the basis of the normal modes:

$$\theta(x,t) = \frac{1}{\sqrt{l}} \sum_{n=1}^{\infty} \beta_n^t(\omega)\phi_n^t(x) \tag{3.48}$$

$$\mathcal{M}_{\text{ext}}(x,t) = \frac{1}{\sqrt{l}} \sum_{n=1}^{\infty} \eta_n^t(\omega)\phi_n^t(x) \tag{3.49}$$

It can easily be shown that the amplitude β_n^t and the forcing η_n^t are coupled variables by the Hamiltonian of the system, and that the equipartition theorem leads to the following expression of the rms thermal noise in θ:

$$\left\langle \theta(x)^2 \right\rangle = \frac{1}{l} \sum_{n=1}^{\infty} \left\langle {\beta_n^t}^2 \right\rangle |\phi_n^t(x)|^2 \tag{3.50}$$

with

$$\left\langle {\beta_n^t}^2 \right\rangle = \frac{k_B T}{C_n} \tag{3.51}$$

We combine those two equations using normalization of torsional modes ϕ_n^t:

$$\frac{1}{l} \int_0^l \mathrm{d}x \left\langle \theta_n(x)^2 \right\rangle = \frac{k_B T}{C_n} \tag{3.52}$$

This quantity can easily be evaluated from our measurement data, leading to an experimental measurement of the torsional rigidity C_n of each torsional mode. The resonances frequencies being precisely known, the relation $I\omega_n^2 = C_n$ directly leads to the measurement of I, the inertial moment of the oscillator. We use the effective length $l_{\text{eff}}^t(n)$ inferred from the wave number and the width w measured with an optical microscope to evaluate again the thickness h from the torsional noise amplitude: we finally measure $h = (0.87 \pm 0.04)\,\mu$m for the raw cantilever, and $h = (1.19 \pm 0.14)\,\mu$m for the coated one (mean value and standard deviation on the first 6 torsional modes). These values are in reasonable agreement with the flexural evaluation.

We have demonstrated that thermal noise maps can be used to determine 2 geometrical parameters of the cantilever: from the wavelength of the modes we access its length l (a mode dependent effective length in the case of our triangular ended cantilever), and from the amplitude of the thermal noise we access its thickness h. Using cross information from flexural and torsional modes we may even evaluate the width w of the cantilever. Indeed with the flexural noise amplitude we measure the mass m of the cantilever, while the torsional mode noise leads to its inertial moment $I = mw^2/12$. The ratio I/m thus directly gives the width w. We estimate with this method $w = (100 \pm 4)\,\mu$m for both levers, is perfect agreement with the measurement with the optical microscope. We eventually use the following width and thickness to estimate the elastic moduli: $w = 97\,\mu$m, $h = 0.8\,\mu$m (raw cantilever), $w = 98\,\mu$m, $h = 1.08\,\mu$m (coated cantilever).

Using those geometrical values and dispersion relation 3.47, we finally reach an estimation of the shear modulus of our cantilevers, that we plot in figure 3.17. S presents a strong frequency dependence, in contrast to Young's modulus behavior. The tabulated value for silicon to consider for the torsion of our cantilever is $S_{xy} = 51\,$GPa (with x and y corresponding to the <110> to <1-10> crystallographic axes of the crystal) [90, 143]. The lowest frequency measurements of S are in good agreement with this value, but the curves strongly departs from it at higher frequency. Note that even if the width and thickness were wrongly evaluated, the increase of S by a factor 2 would still be present. This behavior is unexpected in the classic model we have used for the analysis. The effect of the air around the cantilever can be evaluated from Sader's model for torsional modes [60], and cannot account for the observations. It would furthermore lead to a decrease of the resonances frequencies, when we observe the contrary: for a given wavelength, the system is stiffer than expected (higher S), thus vibrate at a higher frequency.

The failure of Saint-Venant's classic theory at high mode numbers for rods of rectangular cross-section has already been observed in macroscopic experiments, and a refine theory has been proposed by Barr [3]. It accounts both for the normal stresses and inertial forces in the axial direction that are neglected is the classic description. According to this refined theory, the equation of motion for a thin cantilever is

$$\mu^2 \frac{\partial^4 \theta}{\partial x^4} - \left(\frac{\rho}{S} + \frac{\mu^2 \rho}{E} \right) \frac{\partial^4 \theta}{\partial x^2 \partial t^2} - \frac{12}{E h^2 w^2} \left[4Sh^2 \frac{\partial^2 \theta}{\partial x^2} - \rho w^2 \frac{\partial^2 \theta}{\partial t^2} \right] + \frac{\rho^2}{ES} \frac{\partial^4 \theta}{\partial t^4} = 0 \tag{3.53}$$

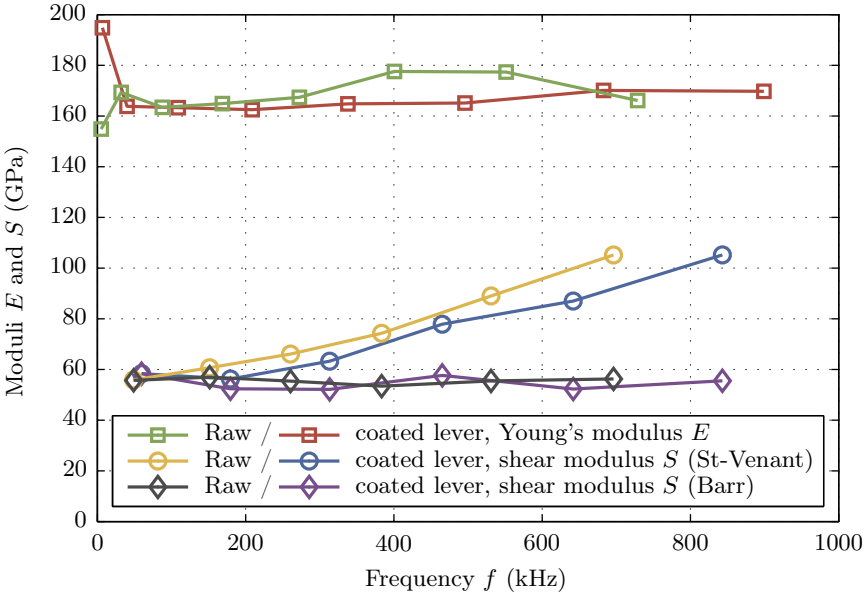

Figure 3.17 – *Young's modulus E and shear modulus S as a function of frequency. These quantity are evaluated through dispersion relations corresponding to flexural and torsional modes respectively, on two different cantilevers. Saint-Venant's classic model for torsional modes leads to an awkward frequency dependent shear modulus: its predictions should be limited to the first mode only. Using a refined model [3], the flat frequency dependence of S is recovered, and leads to a reliable measurement of the shear modulus.*

which leads to the relation dispersion

$$\mu^2\kappa^4 - \left(\frac{\rho}{S} + \frac{\mu^2\rho}{E}\right)\kappa^2\omega^2 + \frac{12}{Eh^2w^2}\left[4Sh^2\kappa^2 - \rho w^2\omega^2\right] + \frac{\rho^2}{ES}\omega^4 = 0 \quad (3.54)$$

where μ^2 is a dimensionless adjustable parameter tuning the phase velocity of torsional waves in the limit of large wavenumber κ. Choosing for this limit the Rayleigh wave velocity, Barr provides an implicit value for μ^2 as a function of Poisson's ratio ν in reference [3]: $\mu^2 \lesssim 1$. The classic dispersion relation 3.47 corresponds to the term between brackets in this last equation, and is recovered at low wavenumber $\kappa \ll 1/w$. Though Barr's derivation has been conducted for isotropic materials, the recent work of Ekel'Chik [49] demonstrates that it is valid for an orthotropic crystal if a plane normal to

cantilever axis is also a symmetry plane of the material. Equation 3.54 can thus be applied to our experiment.

The refined dispersion equation 3.54 is a second order equation in S, and can thus be solved easily. For each resonance, it leads to an expression of S as a function of the wavenumber κ_n^t and the resonance pulsation ω_n^t (that are both measured), and of other known properties of the cantilever: its density ρ, Young's modulus E, width w and thickness h. μ^2 is the only remaining unknown parameter, but it is constrained to values close to 1 [3] and has very little influence on the final estimation of S. We plot in figure 3.17 the final result of this evaluation (with $\mu^2 = 0.95$). The frequency dependence of S has completely disappeared using Barr's model, and its value is $S = (55 \pm 3)\,\mathrm{GPa}$ (raw cantilever) or $S = (55 \pm 2)\,\mathrm{GPa}$ (coated cantilever). These results are in very good agreement with the tabulated value $S_{xy} = 51\,\mathrm{GPa}$.

3.4.3 Thermal noise mapping: summary

We have measured the power spectrum density (PSD) of thermal noise induced deflexion on the whole surface of micro-cantilevers. Thanks to the sensitivity of our apparatus, we can identify many flexural and torsional modes from this noise mapping technique. The spatial shape of the normal mode corresponding to each resonance has been successfully compared to Euler-Bernoulli's prediction for flexural modes of a clamped-free beam, and to Saint-Venant's prediction for torsional modes. The amplitude of those modes are linked to the cantilever stiffness and torsional rigidity, which can be precisely estimated from these measurements. Finally, the dispersion relations linked to these modes are used to separate the mechanical properties of the material (Young's modulus E and shear modulus S) from the geometrical parameters of the cantilever (length l, width w, thickness h). The accurate description of torsional resonant frequencies led to the consideration of a refined model for torsional modes.

The cantilevers probed in this section were made of silicon, and provide an academic bench test for our measurement strategy. We could recover the expected geometrical parameters of the cantilever and the elastic moduli of the material with an excellent precision. The protocol may now be applied to other systems where those parameters are not a priori known. It is expected for example that as the thickness of MEMS component reaches the sub-micrometer scale, mechanical bulk properties could be altered by surface effects (surface tension, defects, etc.) and require specific metrological approaches for their characterization. Our tool can be of valuable interest

in this area. It may also be useful to probe the influence of the environment: functionalized cantilevers used as chemical or biological sensors, alone or in presence of the target molecules, may be precisely characterized with our approach.

3.5 Conclusion

In order to study the mechanical behavior of a cantilever from its fluctuations, we first introduced in this chapter a few useful tools. The keystone of the analysis is the Fluctuation-Dissipation Theorem (FDT), relating the thermal noise spectrum to the dissipative part of the response. Using Kramers-Kronig relations, we showed that we can compare theoretical models and experimental data in terms of both noise spectra and mechanical response. We applied this strategy to confront Sader's model for viscous dissipation with measurements on raw silicon cantilevers in air, demonstrating an excellent agreement. When a gold coating is present on the cantilever, the low frequency behavior is strongly modified, the thermal noise presenting a $1/f$ like trend. We demonstrated this behavior to be the signature of a viscoelastic dissipation process in the cantilever. We were able to provide a quantitative phenomenological description of this effect : a simple power law is found to describe accurately the frequency dependence of the viscoelastic dissipation.

In a last section, we tackled the characterization of the mechanical properties of cantilevers from a mapping of the thermal noise on its surface. This analysis validated the description of the system in terms of its normal modes of oscillations in an Euler-Bernoulli framework for flexion and in Saint-Venant's approach for torsion. The correct description of the dispersion relation for torsional modes however led to the introduction of Barr's refined model [3] to account for observations at high mode numbers. The cantilever stiffness can be precisely measured from this approach, as well as the elastic coefficients E (Young's modulus) and S (shear modulus) of its constituting material.

The low noise of our interferometer, as well as its intrinsic calibration, are obviously central in these experiments : none of the results we presented in this chapter could have been characterized with the classic optical lever scheme of commercial AFMs. The access to the thermal noise spectrum outside resonances is for instance a key point in the evaluation of the dissipation processes. The use of thermal noise is in itself very important, since we don't need to determine exactly the transfer function of the external forc-

ing method which is usually necessary to measure a response function. We get an excellent resolution with measurement of dissipative to conservative force ratio smaller than 10^{-3}.

The characterization methods through thermal noise presented in this chapter could be applied to all kind of cantilever based sensors or MEMS, providing helpful insight on their mechanical behavior in various environment. Our interferometric setup could thus find a very useful place next to the scarce tools for dynamic metrology at nanoscale.

Chapter 4

Adhesion of carbon nanotubes

Collaboration with Julien Buchoux, Sophie Marsaudon and Jean-Pierre Aimé, CPMOH Bordeaux

Abstract

In this chapter, we present peeling experiments of single wall carbon nanotubes (SWNT). Using our AFM, the nanotube is pushed almost perpendicularly against a substrate of graphite or mica. We measure the quasi-static force as a function of the compression, and we simultaneously estimate the dynamic stiffness using a time frequency analysis of thermal noise during this process. The most striking feature of these two observables is plateau curves for a large range of compression, the values of which are substrate dependent.

We then introduce a simple framework to describe the observed behavior: the nanotube is modeled as an Elastica interacting via a simple energy of adhesion per unit length with the substrate. A natural length R_a is defined using this approach, corresponding to the radius of curvature at the point where the nanotube separate from the substrate when a non zero length is adsorbed. A complete analytical resolution of this problem is proposed in the limit of nanotubes that are long with respect to R_a, backed by a numerical simulation for intermediate situations.

The analysis of the experimental data within this simple framework naturally leads to every quantity of interest in the problem: the force plateau is a direct measurement of the energy of adhesion per unit length E_a on each substrate, and we easily determine R_a from the dynamic stiffness plateau. Mechanical properties of the nanotube itself (its bending stiffness EI) can be extracted from those values. We finally compare our results and experimental protocol to the few publications tackling the adsorption of carbon nanotubes.

4.1 Introduction

Due to their unique mechanical and electrical properties, carbon nanotubes (CNT) are foreseen as a major material in a huge range of applications, from fillers in high-strength composites to components of nanoscale electronics and mechanics [5, 22, 81]. They are also widely used as a bench system to study fundamental physical phenomena on the mesoscopic scale, and represent as such an archetype of nano-objects. Whatever exceptional their properties may be, CNT need to interact with the rest of the world in order to be useful. Thus beyond their own behavior, the physics of their interactions should be of major interest too. Due to the stiff sp2-hybridized in-plane bonds of the rolled graphene sheets composing the nanotubes, they mainly interact through Van der Walls (VdW) forces with their environment. In practical cases, they will easily stick on many surfaces, which can be a problem if one wants to use them as shafts, pilars or any other suspended mechanical structures [81]: if for some reason they get too close to a surface, they will stick to it, and loose their functionality. On the contrary, one may seek this strong interaction between the nanotube and the surface, for instance to create a rigid clamping or a good electrical contact, or to build up a bigger object (like a nanotube rope) that will retain the unique mechanical properties of its basic bricks [79]. The efficiency of nanotubes or nanoscale fibers as nanoreinforcements in polymer composites [2, 22, 68] is undoubtedly driven by this surface interaction. Whether desirable or not, it is thus of prime interest to measure and understand the adhesion of carbon nanotubes, and more generally of nanowires and other nanoscopic objects.

Up to now, this phenomenon has been mostly probed by various smart but indirect measurements. Hertel and coworkers [63, 64], for instance, imaged by AFM the shape of crossed CNT adsorbed on a silicium substrate. The profile of the top nanotube balances the deformation energy and the surface energy lost in this configuration, providing an estimation of the adhesion energy if the CNT mechanical properties are assumed. Kis and coworkers [80] performed a direct measurement using an AFM tip to pull the inner core of a telescopic multi wall CNT. Their experiment demonstrated a friction free interaction between the concentric layers, and provides an estimation of the adhesion for this very specific geometry and material. Other experiments designed to measure the mechanical properties of CNT use the adhesion to attach the object to be probed: Young modulus can for example be measured by pushing a nanotube hanging over a hole in the substrate [121]. The deformation data is analyzed under the hypothesis of a double clamped mechanical beam, thus assuming a very strong adsorption

of the nanotube on the surface on each side of the hole. In most experiment, one usually access either intrinsic properties of the nanotubes, or its interaction with its environment, using hypotheses on the other properties. Direct measurement of force of interaction can solve this issue and provide quantitative measurement of several properties in single experiments, as we will demonstrate with this chapter.

Recently, peeling tests at nanoscale have emerged as a potentially powerful technique to characterize adhesion properties of carbon nanotubes or nanowires with various substrates. A few experiments have been conducted [70, 71, 77, 134, 135, 144], along with theoretical/numerical modeling [102, 123]. However, quantitative measurements have not yet been easily achieved, and experimental data analysis relies of complex comparison with numerical simulations. We propose here a simpler protocol to perform peeling tests, which allows direct and quantitative characterization of adhesion. In these experiments, performed in collaboration with Julien Buchoux, Sophie Marsaudon and Jean-Pierre Aimé, a soft CNT is attached to the tip of an AFM cantilever and simply pushed almost perpendicularly on a surface. When the induced bending is strong enough, the VdW interaction causes part of the nanotube to be adsorbed on the substrate, and the analysis of the force curve leads both to quantitative information on the adhesion process and on the nanotube itself.

In this chapter, we first present the experimental protocol (nanotubes, substrates, force and dynamic stiffness measurements) and the most significant features of the measured force-compression curves. We then introduce a simple framework to describe the observed behavior : the nanotube is modeled as an Elastica interacting via a simple energy of adhesion per unit length with the substrate. A complete analytical resolution of this problem is proposed in the limit of long nanotubes, backed by a numerical simulation for intermediate situations. A fine analysis of experimental data is then conducted, before comparing our results and protocol to existing experiments.

4.2 Experiments

4.2.1 Carbon nanotube tip and substrate

The nanotube has been grown directly at the tip apex of an AFM probe, as shown by the SEM (Scanning Electron Microscopy) image of figure 4.1. The synthesis uses the Hot Filament assisted Chemical Vapor Deposition (HFCVD) method [94], and has been performed by Anne-Marie Bonnot in Grenoble, in collaboration with Sophie Marsaudon and Jean-Pierre Aimé in

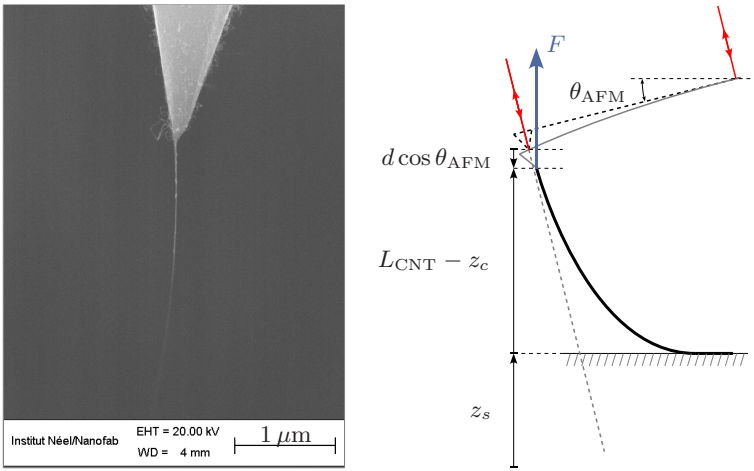

Figure 4.1 – *Scanning electron micrograph of a single wall carbon nanotube grown directly on a AFM tip (left). The CNT length is* $L_{\mathrm{CNT}} \approx 2\,\mu\mathrm{m}$. *In the experiments (right sketch), it is pressed almost perpendicularly against a flat surface* ($\theta_{\mathrm{AFM}} = 15^\circ$)*, and we record the AFM cantilever deflexion* d *as a function of the substrate position* z_s*, or equivalently, of the nanotube compression* z_c*. The force* F *acting on the nanotube is computed from the cantilever deflexion.*

Bordeaux. The probes used in this experiment are contact silicon cantilevers (MikroMasch CSC38), with nominal spring constant in the $10^{-2}\,\mathrm{N/m}$ to $10^{-1}\,\mathrm{N/m}$ range.

High resolution Transmission Electron Microscopy (TEM) observations demonstrate the formation of predominantly single wall (SWNT) and double walled carbon nanotubes. Diameters are mostly found to be between $(1.2 - 2.1)\,\mathrm{nm} \pm 0.3\,\mathrm{nm}$ [51]. Raman spectroscopy studies are also strong indications of the excellent crystalline property and purity of the grown CNT [41].

We probe the interaction of such nanotubes with 2 different substrates: graphite and mica. Both samples are cleaved just before the experiments, and are kept in a closed chamber during the measurement process. The atmosphere is either air or dry nitrogen (with no noticeable difference), and the experiments are performed at ambient temperature.

4.2.2 Measurement protocol and data analysis

CNT compression

In the experiment, we press the CNT against a flat surface, and record the deflexion d of the AFM cantilever as a function of the sample vertical position z_s. A key difference with existing peeling tests in the literature is the orientation of the nanotube: here it is initially almost perpendicular to the substrate, while other experiments use a parallel configuration [70, 71, 134, 135].

The experimental facility as been presented in chapter 2, but we will briefly review its key characteristics for this experiment. The translation of the substrate is performed with a piezo translation platform operated in closed loop, featuring an accuracy of 0.3 nm rms. The measurement of the deflexion d is performed with our home made interferometric deflexion sensor. The intrinsic background noise of our detector is only $10^{-13}\,\mathrm{m}/\sqrt{\mathrm{Hz}}$ for the cantilevers used in this experiment (see figure 4.3). Beyond this very low noise, a key advantage of the technique is that it offers a calibrated measurement of the deflexion, without conversion factor from Volt to meter as in the standard optical lever technique common in AFM. z_s and d being both calibrated, we can therefore compute at any time the CNT compression $z_c = z_s - d\cos(\theta_{\mathrm{AFM}})$. In this formula, $\cos(\theta_{\mathrm{AFM}})$ accounts for the 15° inclination of the AFM cantilever with the substrate, and positive values of d, z_s are directed upward. We set the origin of z_c at the last contact point between the nanotube and the surface: for strong adhesion, this situation reasonably corresponds to a fully extended nanotube, thus to a zero compression.

Static force measurement

We calibrate the spring constant k of the cantilever with a thermal noise measurement far from the sample [26], as presented in chapter 3: the thermal excitation operates like a random force (white noise) on the cantilever, and we measure the resulting power spectrum density (PSD) of deflexion fluctuation. As illustrated in figure 4.3, the PSD of the first resonance of the cantilever is well described by a simple harmonic oscillator model. From this fit, we determine the dynamic spring constant k_1 of the first mode of the cantilever: $k_1 = (84 \pm 5).10^{-3}\,\mathrm{N/m}$. The static stiffness k is deduced from the dynamic one k_1 with a small correction coefficient computed for an Euler Bernoulli description of the cantilever [26]: $k = 0.97k_1 = (81 \pm 5).10^{-3}\,\mathrm{N/m}$. In quasi-static operation, supposing that the force acting on the nanotube

is only vertical, it can be computed by $F = -kd/\cos(\theta_{\mathrm{AFM}})$.

All signal are acquired at 200 kHz with high resolution acquisition cards to determine the force compression curves F vs z_c when cycling the CNT against the substrate at low ramping speed (typically 500 nm/s). Due to the finite stiffness of the cantilever, a classic mechanical instability occurring with attractive forces prevents continuous operation in equilibrium, and part of the force compression curves $F(z_c)$ cannot be accessed during the approach-retraction cycle. To exclude data that do not correspond to quasi-static operation of the cantilever, we discard any point presenting a deflexion speed $\dot{d}$ greater than 3 standard deviations of its equilibrium fluctuations.

Dynamic stiffness

If the ramp is sufficiently slow, we stay long enough around any compression z_c to measure a spectrum of deflexion fluctuations driven by the thermal noise. The force acting on the AFM tip is no longer due to the deflexion of the cantilever alone, since the nanotube touching the surface has to be considered as well. The mechanical oscillator (cantilever first mode) experience an effective stiffness $k_1 + k_{\mathrm{CNT}}$, shifting its resonance frequency from f_0 to f_{CNT}, as illustrated in the inset of figure 4.2. In first approximation, the dynamic stiffness of the cantilever (around the resonance frequency of the oscillator) can be computed by [23]

$$k_{\mathrm{CNT}} = k_1 \left[\left(\frac{f_{\mathrm{CNT}}}{f_0} \right)^2 - 1 \right] \tag{4.1}$$

Taking into account the 15° inclination of the AFM cantilever with the substrate, this formula is slightly modified into:

$$k_{\mathrm{CNT}} = \frac{k_1}{\cos^2 \theta_{\mathrm{AFM}}} \left[\left(\frac{f_{\mathrm{CNT}}}{f_0} \right)^2 - 1 \right] \tag{4.2}$$

We perform a time-frequency analysis of the deflexion signal, to access at each time to the PSD of the thermal noise driven deflexion. As long as the quasi-static approximation is valid and the resonance has a high enough quality factor, the maximum of the spectrum directly gives f_{CNT}, so we can use equation 4.2 to estimate k_{CNT}. Figure 4.2 present a spectrogram of the deflexion signal during an approach-retract cycle. Each spectrum $S_d(t, f)$ has been computed in a 5 ms time window, corresponding to a 2.5 nm translation of the sample.

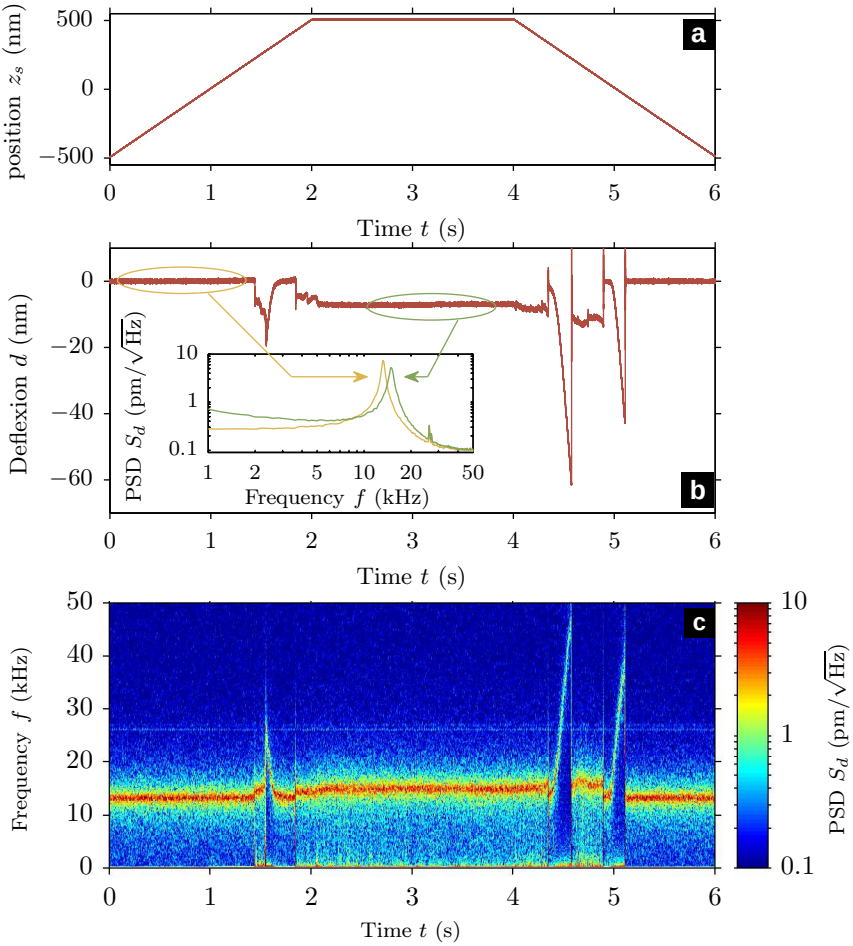

Figure 4.2 – *Time frequency analysis of the deflexion. Time trace of the substrate position z_s (**a**) and of the cantilever deflexion d (**b**) during an approach-retract cycle. In the inset, a power spectrum density (PSD) of the deflexion signal is shown before (yellow) and during (green) contact: thermal noise excites the first resonance of the mechanical oscillator composed by the AFM cantilever and the CNT connecting the surface and the AFM tip. The dynamic stiffness k_{CNT} of the nanotube can be computed from the observed frequency shift of the resonance. We generalize this technique with a time frequency analysis: every* 5 ms, *we compute a PSD of the deflexion and plot the result in the color coded spectrogram (**c**). We extract from this plot the time evolution of the resonance frequency, and thus of the dynamic stiffness.*

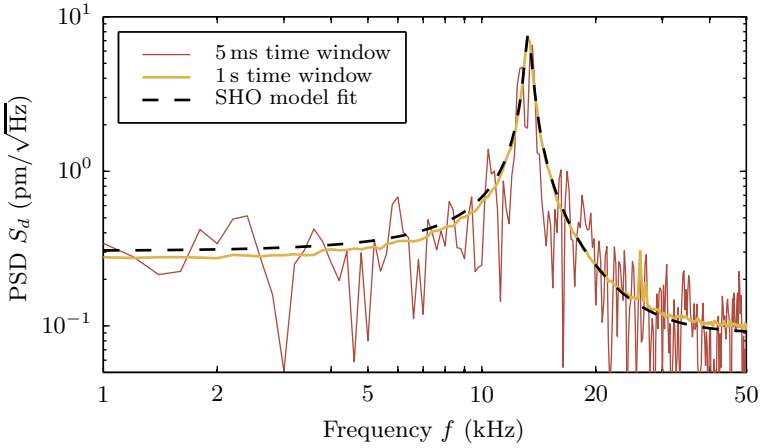

Figure 4.3 – *"Instantaneous" power spectrum density $S_d(t, f)$, computed in a* 5 ms *time window are much noisier than the averaged PSD presented in the inset of figure 4.2 (yellow curve is averaged for* 1 s*). The resonance frequency of the mechanical oscillator can however be computed using a frequency average weighted by $S_d(t, f)$ (equation 4.3), and match with a good precision the one deduced from the fit on the average curve with a simple harmonic oscillator (SHO) model.*

The spectrums in the inset of figure 4.2 have been averaged on a longer time window (1 s), they present a smooth shape that is easy to fit with a simple harmonic oscillator model. However, "instantaneous" spectrum are much noisier, as illustrated in figure 4.3. Due to the short 5 ms time window, the frequency resolution is only 200 Hz, and data is too noisy too be fitted easily. However, the maximum of power spectrum density $S_d(t, f)$ can be measured with the following estimator:

$$f_{\text{CNT}}(t) = \frac{\int_{\Delta f} f S_d(t, f) \mathrm{d}f}{\int_{\Delta f} S_d(t, f) \mathrm{d}f} \tag{4.3}$$

Where Δf is an adequate frequency interval centered on f_{CNT} (self adapting procedure). For example, using this estimator on a 1 s interval around $t = 3$ s for the deflexion signal plotted in figure 4.2, we estimate $f_{\text{CNT}} - f_0 = (1610 \pm 250)$ Hz (the incertitude corresponds to one standard deviation), to be compared to $f_{\text{CNT}} - f_0 = 1680$ Hz estimated with a fit of the average power spectrum density on the same time interval. The thermal noise exci-

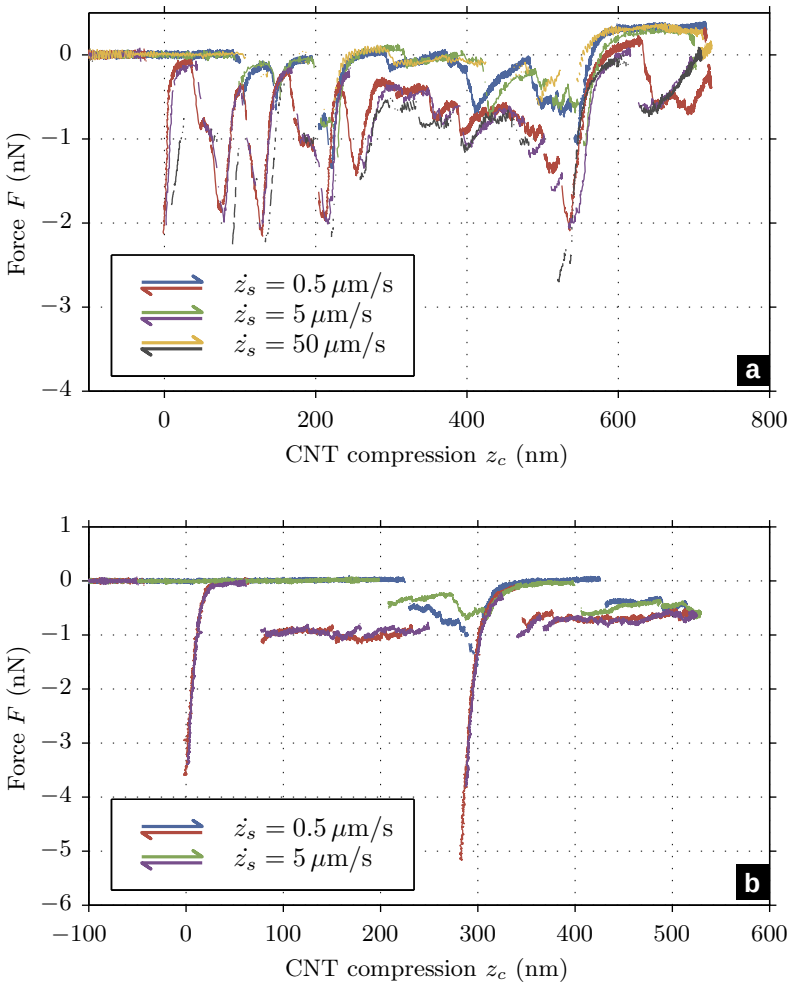

Figure 4.4 – *Force-compression curves for 2 different nanotubes on a substrate of graphite. Three different cycles are plotted for first nanotube in (**a**) and two for the second in (**b**), each corresponding to different landing positions on the substrate and different ramping speeds $\dot{z}_s$ from* $0.5\,\mu$m/s *to* $50\,\mu$m/s. *Although complex, the response is very reproducible, hinting at a nanotube specific signature rather than spurious effect such as stick-slip of the surface. Approach and retraction curves present a strong hysteresis in some portions, and a perfect overlap in others. The force is mostly attractive, with two types of behavior: diverging like events ending with a jump, or plateaux around* 0 *and* -1 nN.

tation is clearly strong enough to determine the resonance frequency shift, and thus k_{CNT}.

4.2.3 Force and stiffness versus compression curves

In the experiments, the CNT is pushed against a flat surface, and we measure the force-compression profile $F(z_c)$ of the nanotube during an approach-retract cycle. We present the result of such measurements in figure 4.4 for a substrate of graphite and 2 different nanotubes. The shape of the curve can be rather complex, but is very reproducible for a single nanotube: it is independent on the landing position and on the ramping speed, for $\dot{z_s}$ varying on two orders of magnitude. A strong hysteresis between approach and retraction can be noticed, although a perfect overlap of both force-compression profiles is retrieved in some part of the curves. The interaction is everywhere attractive ($F < 0$) or marginally repulsive, hinting at adhesion to be the most pertinent process to consider. Two types of behavior can be distinguished: diverging like events ending with a jump, or plateaux around 0 (mainly during approach) and $-1\,\mathrm{nN}$ (mainly during retraction). The signature of the second nanotube (figure 4.4-**b**) is easier to read, since it presents only two "accidents" during retraction and large force plateaux. We will therefore focus our analysis on this sample, but the conclusions are applicable to others as well.

We present in figure 4.5 the force and dynamic stiffness versus compression curves. The shape of k_{CNT} is strongly connected to that of F: diverging values of k_{CNT} in parallel to force accidents, and plateaux around zero and $0.3\,\mathrm{N/m}$ in correspondence to the force plateaux. As previously mentioned, this behavior is very robust and the measurement is reproducible for different landing position of the substrate, ramping speeds, surrounding atmosphere (air or dry nitrogen). The behavior is even robust if we change the nature of the substrate, as illustrated in figure 4.6 for a surface of mica. However, the values of the force and stiffness plateaux are lower than those of graphite in this case. A direct comparison of force-compression curves for the 2 different substrates is given in figure 4.7, which reports the results of 80 compression cycles, half on mica and half on graphite, using different ramping speeds.

To interpret those observations, let us simply model the nanotube by an elastic line, incompressible along its axis. The shape of the force-compression curves, with two similar patterns (force plateaux, jumps and divergences) occurring reproducibly at about 300 nm distance for that specific nanotube, suggests that it is not integer on its whole $2\,\mu\mathrm{m}$ length. On other nanotubes,

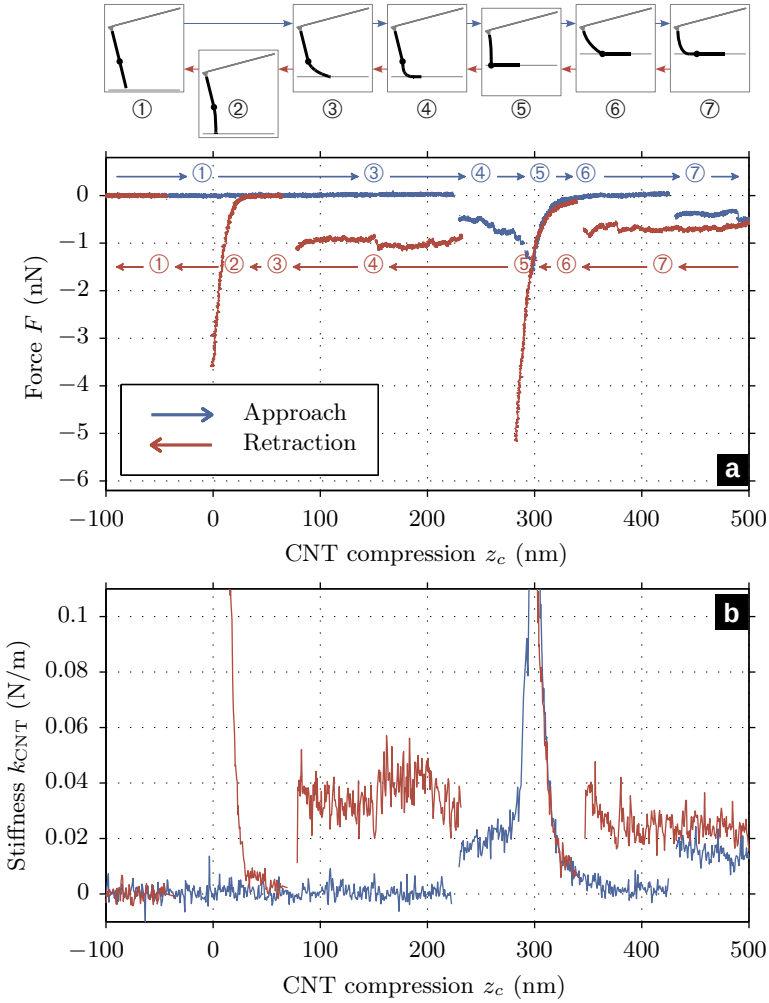

Figure 4.5 – *Force F and dynamic stiffness k_{CNT} of a nanotube as a function of its compression on a* graphite *substrate. A strong hysteresis, due to adhesion, can be noted between approach (blue) and retraction (red). Well defined plateaux of force (around* 0.98 nN*) and stiffness (around* 0.036 N/m*) allow one to estimate the energy of adhesion of the CNT on graphite ($E_a^{\mathrm{HOPG}} = 0.98$ nJ/m*), as well as the nanotube mechanical properties. The jumps and steep peaks of the curves are signature of transitions between contact and adhesion shapes of various portions of the nanotube, as suggested by the scenario of numbered sketches. Off scale data for k_{CNT} climb up to* 1 N/m.

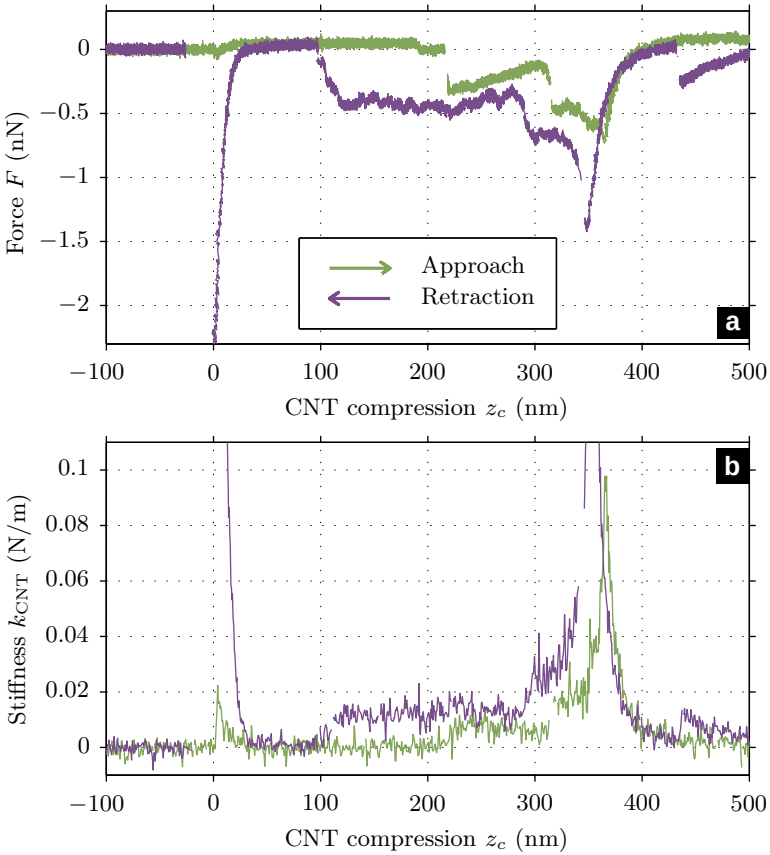

Figure 4.6 – *Force F and dynamic stiffness k_{CNT} of a nanotube as a function of its compression on a* mica *substrate. The curves are very similar to those of figure 4.5 with a graphite surface, except for the vertical scale: the energy of adhesion is estimated at $E_a^{\mathrm{mica}} = 0.42\,\mathrm{nJ/m}$, about half of that with graphite. Similarly, the dynamic stiffness of a nanotube adsorbed on mica is one third of that on graphite: $k_{\mathrm{CNT}}^{\mathrm{peeling}} = 0.013\,\mathrm{N/m}$.*

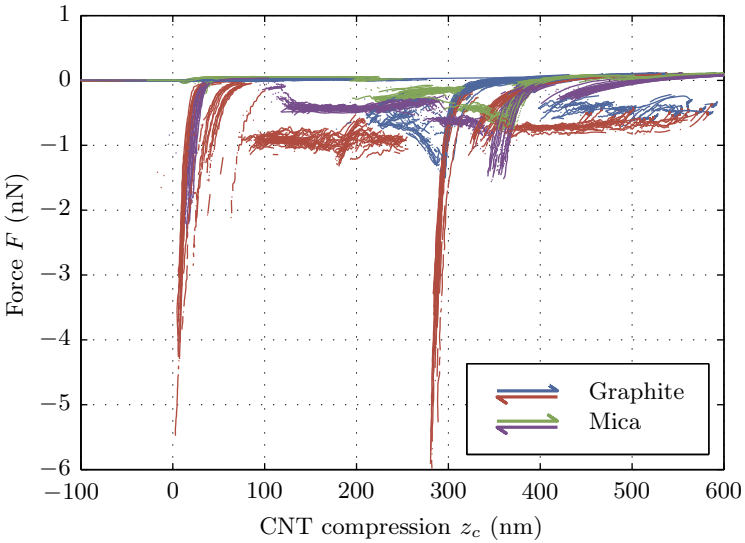

Figure 4.7 – *Comparison of force-compression curves for graphite and mica: 40 independent measurements are plotted for each substrate, half with a ramping speed* $\dot{z_s} = 0.5\,\mu$m/s *and half with* $\dot{z_s} = 5\,\mu$m/s. *The reproducibility of force plateaux is excellent, and characteristic of the nature of the sample.*

such as the one presented in figure 4.4-**a**, similar reproducible patterns can be observed, with distances from few tens of nanometers up to 400 nm. Spurious effects as stick-slip phenomenon can be discarded as the observed behavior is independent on ramping speeds. The few peeling tests found in the literature on other nanotubes also present similar discontinuities in the force curves [70, 71, 133, 134, 144]. A sound hypothesis is that the nanotube is composed of several ideal segments linked by defects presenting higher flexibility (kink like defects for example). The equilibrium shape of each segment can thus be described by the Elastica, as will be detailed in part 4.3.

Let us denote by E_a the energy of adhesion per unit length of the nanotube on the substrate. As soon as part of the nanotube is adsorbed, the systems tends to minimize its energy by maximizing the absorbed length. However, this process increases the bending of the free standing part of the nanotube and the associated curvature energy. The adsorbed length will thus be a balance between adhesion and bending, leading to a given radius

of curvature R_a at the contact point . If the free standing part of the nanotube is long compared to R_a, its shape does not change much when it is being peeled from the substrate. The vertical displacement δz needed to peel a small length δl is in first approximation $\delta z \simeq \delta l$. As we are pulling with a force F, the work produced is $F\delta z$ while the energy released is $-E_a\delta l$, leading to $F \simeq -E_a$: *peeling the nanotube results in a flat force-compression curve.* This is indeed what is observed in our experiments, the value of the plateaux giving direct access to the value of the energy of adhesion per unit length: $E_a^{\mathrm{HOPG}} \simeq 0.98\,\mathrm{nJ/m}$ for graphite substrate, and $E_a^{\mathrm{mica}} \simeq 0.42\,\mathrm{nJ/m}$ for mica. The complete analysis of this behavior will be presented in section 4.7.2.

Flat force-compression curves should lead to zero stiffness, since is implies $\mathrm{d}F/\mathrm{d}z = 0$. However, it is clear on figures 4.5 and 4.6 that k_{CNT} does not vanish when the force presents a plateau. This dynamic stiffness is measured in the $(10 - 50)\,\mathrm{kHz}$ range through thermal noise fluctuation. The discrepancy between k_{CNT} and $\mathrm{d}F/\mathrm{d}z$ can be explained by the simple assumption that adhesion is a slow process: in such a case, high frequency thermal fluctuations will only probe the response of the free standing part of the nanotube, the adsorbed length acting like a rigid clamping condition at fast time scales. We will show in the next sections that the measured value of this dynamic stiffness can be related to the mechanical properties of the nanotube.

4.3 A tool to describe the shape of a carbon nanotube: the Elastica

In this section, we will present a simple model to analyze experiments where a carbon nanotube (CNT) is pushed (more or less) perpendicularly against a substrate. This CNT is attached to an AFM tip, so that we can experimentally measure the force versus distance dependance. The nanotube is modeled by an elastic line, incompressible along its axis. We will restrict our analysis to deformations in a single plane $(\mathbf{e_x}, \mathbf{e_z})$, as sketched in figure 4.8. The shape of the CNT is described by the coordinates $x(s)$, $z(s)$ of a parametric curve, where s is the arc length abscissa along the line. At each point, $\theta(s)$ is the angle between the local slope and the vertical (along $\mathbf{e_z}$) direction. By convention, we will put the origin $\mathbf{O}$ of the coordinates at the first extremity ($s = 0$) of the CNT (the one we are holding). The final point of the CNT ($s = L$, where L is the length of the free standing part of the

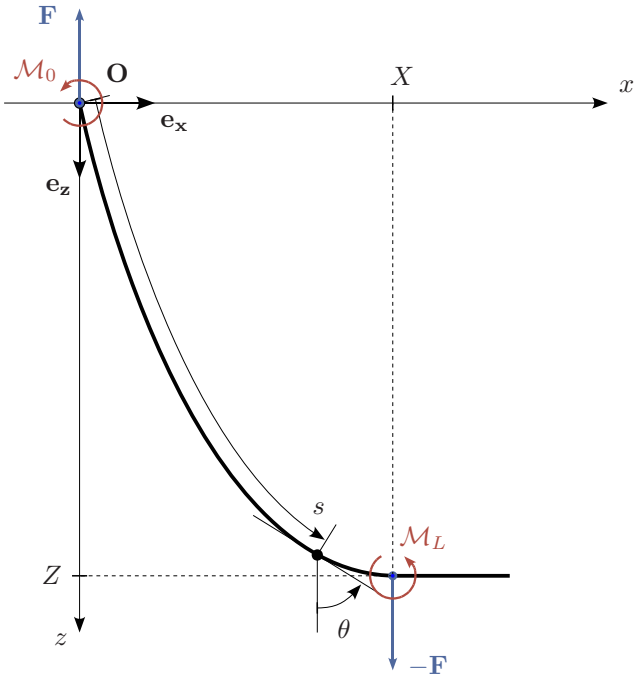

Figure 4.8 – *The shape of the nanotube is described by the coordinates $x(s)$, $z(s)$ of a parametric curve, where s is the arc length along the line. $\theta(s)$ is the angle between the local slope and $\mathbf{e_z}$. $\mathcal{M}_0$ and $\mathcal{M}_L$ are the bending moments applied at the origin* **O** *and at the free end of the CNT, and* **F** *is the force applied at the origin. The length L of the free standing part of the nanotube may be smaller than its whole length L_{CNT}, if part of it is adsorbed on the surface.*

nanotube) has coordinates X and Z, with

$$X = \int_0^L \sin\theta \, \mathrm{d}s \tag{4.4}$$

$$Z = \int_0^L \cos\theta \, \mathrm{d}s \tag{4.5}$$

If some part of the nanotube is adsorbed on the surface, the length L of this free standing part will be smaller than the total length of the nanotube L_{CNT}. Using these notations, the CNT compression z_c used in the previous

part is

$$z_c = L_{\mathrm{CNT}} - Z \tag{4.6}$$

To ease direct comparison with experimental results, we will use z_c in the figures, but will mainly use Z during calculation.

We will make the hypothesis that the CNT is not submitted to any external forces along its length, except at its two extremities. In equilibrium, these two forces will simply be opposite so that the total force acting on the nanotube is zero. In fact, the same argument holds at any point along the line, so that the force $\mathbf{F}$ of the upper part acting on the lower part is a constant along the curve. Moreover, we will suppose that it is only vertical[1]: $\mathbf{F} = F\mathbf{e_z}$. $F > 0$ corresponds to a compression force on the nanotube, previously measured as a repulsive force on the cantilever, while $F < 0$ corresponds to a pulling force (attractive for the cantilever).

The bending moment $\mathcal{M}$ at each point along the line can be related to its local curvature:

$$\mathcal{M} = EI\frac{\mathrm{d}\theta}{\mathrm{d}s} = EI\theta' \tag{4.7}$$

where E is the Young's modulus and I the quadratic moment of the CNT. At equilibrium, the sum of the moments acting on an infinitesimal element should be zero, which leads to the expression of the Elastica [82]:

$$EI\frac{\mathrm{d}^2\theta}{\mathrm{d}s^2} = EI\theta'' = -F\sin\theta \tag{4.8}$$

Note that this equation is analog to the equation of motion of a pendulum, where s, F and EI play respectively the role of time, gravity and length of the pendulum. $F < 0$ (pulling forces, equivalent to attractive forces of previous part) corresponds to a gravity field directed towards $\theta = \pi$, $\theta = 0$ is thus an unstable equilibrium in this analogy. A solution to this equation is a minimum of the energy of curvature of the line:

$$E_c = \frac{1}{2}EI\int_0^L \left(\frac{\mathrm{d}\theta}{\mathrm{d}s}\right)^2 \mathrm{d}s \tag{4.9}$$

Direct integration of equation 4.8 leads to a first invariant of the Elastica:

$$EI\left(\theta'(s) - \theta'_0\right) + Fx(s) = 0 \tag{4.10}$$

[1]The horizontal force $F_x\mathbf{e_x}$ acting on the line is zero if the contact of the nanotube with the surface can freely slide, or if the holding point can freely move laterally

This equation can also be read as the expression of the equilibrium of moments at the origin for the portion of the nanotube between 0 and s. Multiplying equation 4.8 by θ' and integrating, one finds a second invariant in s:

$$\frac{1}{2}EI\theta'(s)^2 - F\cos\theta(s) = \text{Invariant} \tag{4.11}$$

The Elastica is a second order differential equation thus we need to express two boundary conditions to solve it. F is in general also unknown, but is fixed by the integral constraint (4.5) which fixes the distance between the origin of the nanotube and the substrate. Classic boundary conditions that can be found are θ fixed (clamped extremity) or $\theta' = 0$ (torque free extremity). We will study briefly 2 cases of interest for our experiment:

- **Absorbed nanotube**: a strong interaction with the substrate tends to adsorb the nanotube on the surface. In this case, the continuity of the slope of the elastic line sets the slope of the curve for the last point of the free standing part :

$$\theta_L = \frac{\pi}{2} \tag{4.12}$$

  The length of this free standing part will then be tuned by an energy balance between adsorption and curvature. The second boundary condition, at the origin, will prove to be of low importance in the limit of large Z, as soon as the nanotube is long enough. We will show that it should be treated as torque free extremity:

$$\theta'_0 = 0 \tag{4.13}$$

- **Point contact**: if the nanotube end is not adsorbed on the surface (i.e. $\theta_L \neq \pi/2$) and can freely slide, the origin cannot be treated as a pivot point any more (or the equilibrium shape will just be a straight line). In this case, a clamped origin is a sound hypothesis, while the final point is simply free of any torque:

$$\theta_0 = \theta_{\text{AFM}} \tag{4.14}$$

$$\theta'_L = 0 \tag{4.15}$$

  θ_{AFM} is the angle imposed by the way the CNT is attached to the AFM tip, and adding the effect of the classic 15° inclination of the cantilever with respect to the surface. Reasonable values for θ_{AFM} thus lie in the $[0° - 30°]$ range.

A way to unify these two different boundary conditions at the origin would be to consider a "weak" torque spring, for which we can write $\theta'_0 = -\kappa(\theta_0 - \theta_{\mathrm{AFM}})$. If κ is small in some sense, we tend to the boundary condition of first case (eq. 4.13), while in the other limit we tend to that of the second case (eq. 4.14).

4.4 Absorbed nanotube

In this section, we compute the equilibrium force corresponding to an adsorbed Elastica, and its equivalent vertical stiffness. The attraction force can be modeled by a Van der Waals interaction between the nanotube and the sample. However, this short range force drops to zero as soon as the nanotube is a few nanometers away from the surface, a distance comparable to its diameter. We already dropped any description of phenomenon at this scale for the nanotube when modeling it as an elastic line, we therefore study the limiting case where the interaction is restricted to pure contact only. The adhesion is then simply described by E_a, the adsorption energy per unit length. The substrate is also supposed to be infinitely stiff and not to deform due to its interaction with the nanotube. The interested reader may refer to [102, 123] for more complete approaches where the full Van der Waals interaction is considered.

4.4.1 Force plateau

Let us start from the expression of total energy E_{CNT} of the nanotube, which is the sum of the curvature energy $E_c(L)$ of its free standing part of length L (described by eq. 4.9), and of the adhesion energy of its adsorbed length:

$$E_{\mathrm{CNT}} = E_c(Z, L) - (L_{\mathrm{CNT}} - L)E_a \tag{4.16}$$

where L_{CNT} is the total length of the nanotube, and E_a its adsorption energy per unit length. For a given distance Z between the origin and the substrate, the free standing length L adjusts itself so as to minimize this total energy, so that in equilibrium we have [100, 129]:

$$E_a = -\left.\frac{\partial E_c}{\partial L}\right|_Z = -\frac{1}{2}EI\frac{\partial}{\partial L}\int_0^L \left(\frac{\mathrm{d}\theta}{\mathrm{d}s}\right)^2 \mathrm{d}s = \frac{1}{2}EI{\theta'_L}^2 \tag{4.17}$$

A derivation of this relation can be found in Appendix C.1. Let us define the natural radius of curvature R_a corresponding to this balance between

adsorption and curvature by:

$$\frac{1}{R_a^2} = \frac{2E_a}{EI} = {\theta'_L}^2 \tag{4.18}$$

Injecting boundary condition $\theta_L = \pi/2$ into equation 4.11, and substituting the value of θ'_L just computed, one immediately gets

$$F\cos\theta = -E_a(1 - R_a^2{\theta'}^2) \tag{4.19}$$

We will now demonstrate that $F \simeq -E_a$ in the limit of large separation with respect to the natural radius of curvature ($Z \gg R_a$). We adapt the calculation of the period of a pendulum to our problem, starting from last equation:

$$\left(\frac{\mathrm{d}\theta}{\mathrm{d}s}\right)^2 = {\theta'}^2 = \frac{1}{R_a^2}\left(1 + \frac{F}{E_a}\cos\theta\right) \tag{4.20}$$

hence

$$\mathrm{d}s = R_a\left(1 + \frac{F}{E_a}\cos\theta\right)^{-1/2}\mathrm{d}\theta \tag{4.21}$$

$$L = \int_0^L \mathrm{d}s = R_a\int_{\theta_0}^{\pi/2}\left(1 + \frac{F}{E_a}\cos\theta\right)^{-1/2}\mathrm{d}\theta \tag{4.22}$$

$$\frac{L}{R_a} \leqslant \int_{\theta_0}^{\pi/2}\left(1 - \left|\frac{F}{E_a}\right|\right)^{-1/2}\mathrm{d}\theta \tag{4.23}$$

$$\frac{L}{R_a} \leqslant \left(\frac{\pi}{2} - \theta_0\right)\left(1 - \left|\frac{F}{E_a}\right|\right)^{-1/2} \tag{4.24}$$

$$0 \leqslant 1 - \left|\frac{F}{E_a}\right| \leqslant \left[\left(\frac{\pi}{2} - \theta_0\right)\frac{R_a}{L}\right]^2 \leqslant \left(\pi\frac{R_a}{L}\right)^2 \tag{4.25}$$

We see that in the limit $R_a \ll Z < L$, $|F|$ converges to E_a. F being negative (pulling force), we have

$$\lim_{Z/R_a\to\infty} F = -E_a \tag{4.26}$$

When pulling the nanotube from the surface, as soon as its length is greater than R_a, we have thus demonstrated that the force F should present a plateau whose value is precisely $-E_a$, the energy of adhesion per unit length. This result is robust to any reasonable boundary condition chosen at the origin. We present in figures 4.9 and 4.10 a numerical integration of the Elastica illustrating this behavior, for a ratio $L_{\mathrm{CNT}}/R_a = 5$: the force plateau spans about half of the force-extension curve.

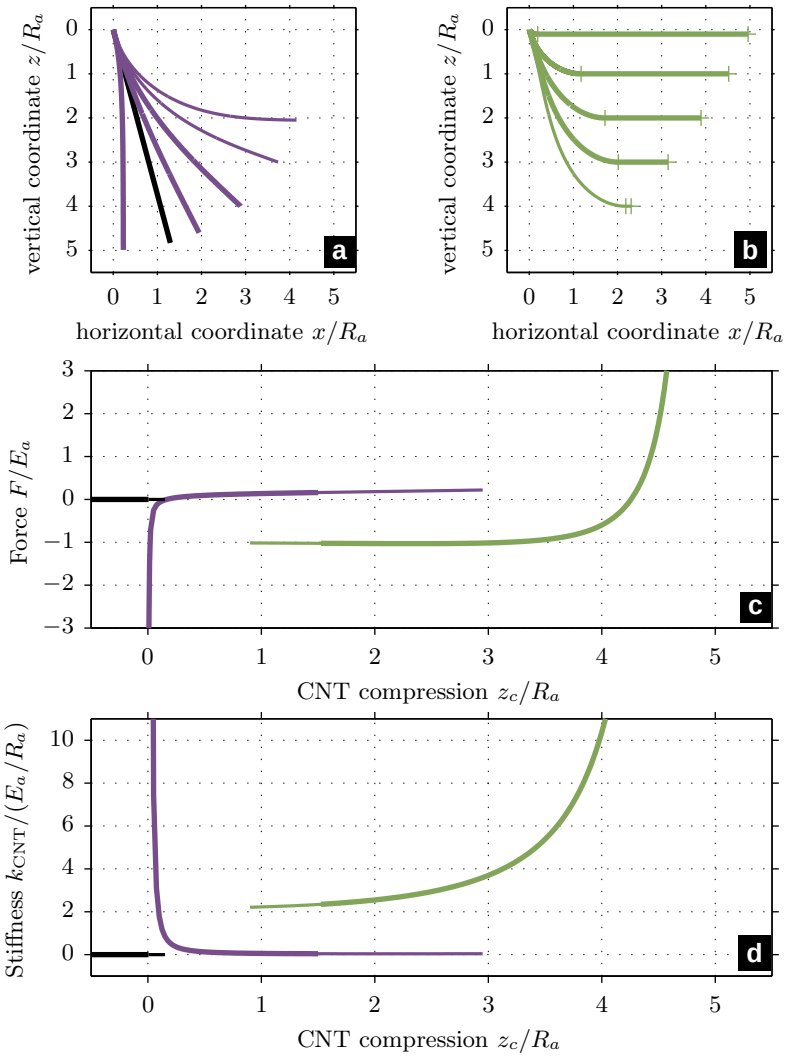

Figure 4.9 – *Numerical integration of CNT compression for* $L = 5R_a$ *and* clamped origin *in absorbed state. Fundamental and metastable states are respectively drawn as thick and thin lines. Shape for point contact (**a**) and adsorbed state (**b**). Force* F *(**c**) and dynamic stiffness* k_{CNT} *(**d**) as a function of compression. When cycling* Z*, the nanotube switches between straight shape (black), weakly bended state (purple), and adsorbed state (green), presenting large force and dynamic stiffness plateau except for the highest compressions, where* $F \to +\infty$.

4.4.2 Boundary condition at the origin

The effect of the boundary condition chosen at the origin in the limit of small separation ($L \ll R_a$) has a huge effect of the behavior of the force F: we will now show that for a clamped origin (eq. 4.14), the force will go to $+\infty$ (diverging compression force), whereas if we choose a torque free condition (eq. 4.13), $F \to -\infty$ (diverging pulling force).

Case 1: clamped origin

Let $s_{\max}$ correspond to the coordinate of the maximum value of θ', we immediately get:

$$\frac{1}{L}(\theta_L - \theta_0) = \frac{1}{L}\int_0^L \theta'(s)\mathrm{d}s \leqslant \theta'(s_{\max}) \tag{4.27}$$

From the expression of the second invariant of the Elastica (eq. 4.11) in $s = L$ and $s = s_{\max}$, we have:

$$\frac{1}{2}EI\theta'(s_{\max})^2 - F\cos\theta(s_{\max}) = \frac{1}{2}EI{\theta'_L}^2 = E_a \tag{4.28}$$

therefore,

$$F = \frac{E_a}{\cos\theta(s_{\max})}\left(R_a^2\theta'(s_{\max})^2 - 1\right) \geqslant \frac{E_a}{\cos\theta(s_{\max})}\left(\frac{R_a^2}{L^2}(\theta_L - \theta_0)^2\right) \tag{4.29}$$

The limit as L tends to zero is thus

$$\lim_{L/R_a \to 0} F = +\infty \tag{4.30}$$

Clamped boundary condition at the origin (eq. 4.14) thus leads to a diverging compression force in the limit of small separation, when $L \ll R_a$. This is easy to understand as linking the two different slopes at the extremities on shorter and shorter length leads to a diverging curvature ($\theta' \propto 1/L$) and associated energy ($E_c \propto L\theta'^2 \propto 1/L$). A numerical integration of the Elastica corresponding to these boundary conditions is plotted in figure 4.9, illustrating this divergence of the force at large compression.

Case 2: torque free origin

Let us express the first invariant of the Elastica (eq. 4.10) at $s = L$, using a torque free hypothesis ($\theta'_0 = 0$) at the origin :

$$EI\theta'_L = 2E_aR_a = -FX \tag{4.31}$$

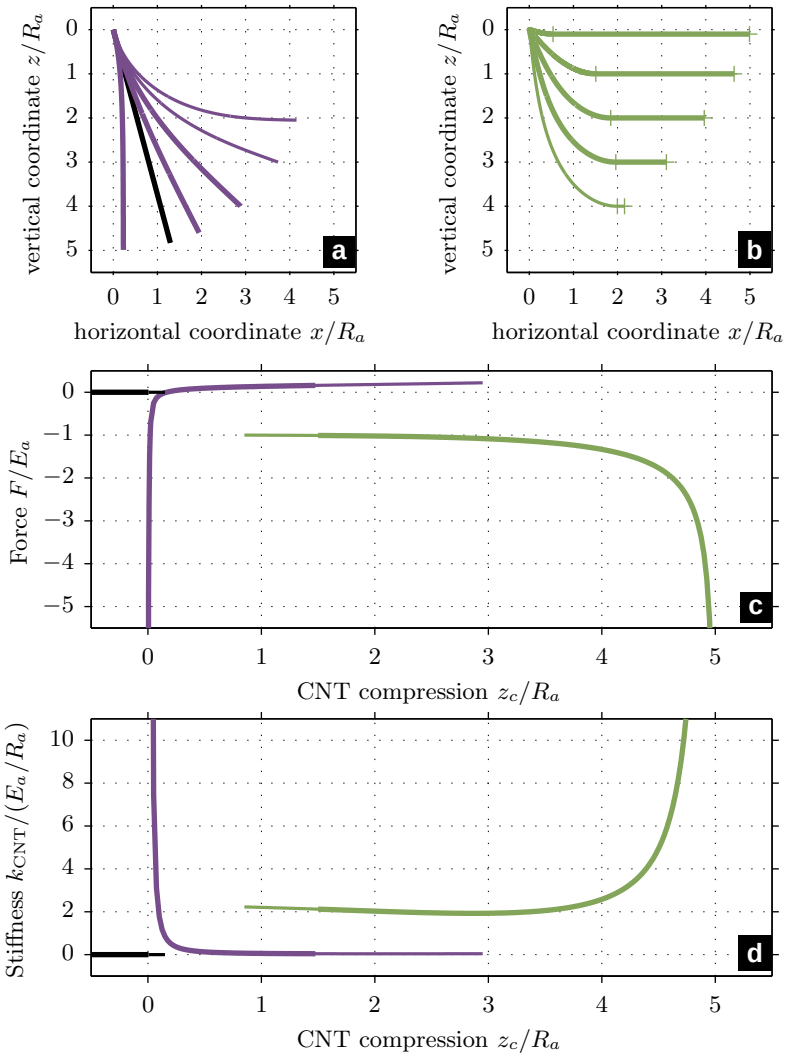

Figure 4.10 – *Numerical integration of CNT compression for* $L = 5R_a$ *and* torque free origin *in absorbed state. Fundamental and metastable states are respectively drawn as thick and thin lines. Shape for point contact (***a***) and adsorbed state (***b***). Force* F *(***c***) and dynamic stiffness* k_{CNT} *(***d***) as a function of compression. When cycling* Z*, the nanotube switches between straight shape (black), weakly bended state (purple), and adsorbed state (green), presenting large force and dynamic stiffness plateau except for the highest compressions, where* $F \to -\infty$*.*

Since $X \leqslant L$, we immediately get

$$\lim_{L/R_a \to 0} F \leqslant \lim_{L/R_a \to 0} -2E_a \frac{R_a}{L} = -\infty \tag{4.32}$$

Torque free boundary condition at the origin thus leads to a diverging attractive force in the limit of small separation , when $L \ll R_a$.

Again, this can be simply understood using energy considerations: if the nanotube is entirely adsorbed, freeing a length X from the surface only implies a lift of $Z \propto X^2/R_a$ (curvature R_a at the detachment point), releasing an energy $E_a X$. The work done during this operation is $W = FZ$, hence $F \propto -E_a R_a/X$. A numerical integration of the Elastica corresponding to these boundary conditions is plotted in figure 4.10, illustrating this divergence of the force at large compression.

Comparison to experiments

As seen in the previous part (figures 4.5 to 4.7), when the compression of the nanotube is increased, the force in an adsorbed state tend to be more attractive, and a "diverging like" attractive force is needed to lift an adsorbed segment. This scenario is consistent with the second case studied here: $\theta_0' = 0$. We shall therefore adopt the hypothesis of a torque free origin (eq. 4.13) in the analysis of the behavior of the adsorbed nanotube.

4.4.3 Loosing adhesion

In this paragraph, we compute the minimum nanotube compression $z_c^{\min}$ for which the adsorbed state exists : when peeling the nanotube, the length of the absorbed part $L_{\mathrm{CNT}} - L$ will vanish at some point, and this branch of solution will disappear. Following the conclusion of the previous paragraph, we use boundary conditions (4.12) and (4.13) : torque free origin, adsorbed end. We rewrite equation 4.22 to compute the quantity $L - Z$:

$$\mathrm{d}s = R_a \left(1 + \frac{F}{E_a}\cos\theta\right)^{-1/2} \mathrm{d}\theta \tag{4.33}$$

$$L - Z = \int_0^L (1 - \cos\theta)\mathrm{d}s \tag{4.34}$$

$$L - Z = R_a \int_{\theta_0}^{\pi/2} (1 - \cos\theta)\left(1 + \frac{F}{E_a}\cos\theta\right)^{-1/2} \mathrm{d}\theta \tag{4.35}$$

The last adsorption point corresponds to the largest extension Z of the nanotube in the adsorbed state, we thus work in the limit of $Z \gg R_a$. We

therefore have $F \simeq -E_a$, and equation 4.19 with boundary condition $\theta'_0 = 0$ leads to $\theta_0 \simeq 0$. Hence

$$L - Z \simeq R_a \int_0^{\pi/2} (1 - \cos\theta)^{1/2} \mathrm{d}\theta = 2(\sqrt{2} - 1)R_a \tag{4.36}$$

The minimum compression occurs when $L = L_{\mathrm{CNT}}$, thus from the definition of the nanotube compression z_c (equation 4.6) we estimate

$$z_c^{\min} = L_{\mathrm{CNT}} - Z \approx 0.83 R_a \tag{4.37}$$

The minimum compression needed for the adsorbed state to exist is thus just a little smaller than R_a. The compression for which we loose adhesion during the experiment can thus be used to estimate directly R_a. In figure 4.10, we indeed check from the numerical integration of the Elastica in the case $L_{\mathrm{CNT}} = 5R_a$ that this transition occurs at $z_c^{\min} \approx 0.85 R_a$, very close to the prediction of equation 4.36, corresponding to the limit $L_{\mathrm{CNT}} \gg R_a$.

4.4.4 Dynamic stiffness

We will now focus on the vertical stiffness of the CNT, using boundary conditions (4.12) and (4.13) : torque free origin, adsorbed end, as in previous paragraph. Let us rewrite the two invariants of the Elastica (eq. 4.10 and 4.11) for $s = 0$ and $s = L$:

$$EI\theta'_L = -FX \tag{4.38}$$

$$\frac{1}{2} EI {\theta'_L}^2 = -F\cos\theta_0 \tag{4.39}$$

Using the definition of $R_a = 1/\theta'_L$ (eq. 4.18), we easily get from these equations in the following relations for an adsorbed nanotube in equilibrium:

$$F = -\frac{E_a}{\cos\theta_0} \tag{4.40}$$

$$X = 2R_a \cos\theta_0 \tag{4.41}$$

In the limit of large separations, we have shown in paragraph 4.4.1 that the equilibrium force is independent of Z, thus the static stiffness is zero. Nevertheless, if we suppose that the adhesion process is slow, at higher frequency the nanotube behaves as if its length L is fixed and cannot be adjusted to balance the adsorption. We will however stay in slow time scale

with respect to the dynamics of the free standing part of the nanotube, such that we still can use the Elastica to compute the dynamic stiffness k_{CNT}:

$$k_{\mathrm{CNT}} = -\left.\frac{\partial F}{\partial Z}\right|_L \tag{4.42}$$

Note that if the adhesion process is not completely frozen at the time scale we are probing, the measured stiffness will actually be somewhere between the static and dynamic value.

Let us first derive by Z equations 4.38 and 4.39 :

$$EI\frac{\partial \theta'_L}{\partial Z} = k_{\mathrm{CNT}}X - F\frac{\partial X}{\partial Z} \tag{4.43}$$

$$EI\theta'_L\frac{\partial \theta'_L}{\partial Z} = k_{\mathrm{CNT}}\cos\theta_0 + F\sin\theta_0\frac{\partial \theta_0}{\partial Z} \tag{4.44}$$

Combining those two equations, we have

$$k_{\mathrm{CNT}}(X - R_a\cos\theta_0) = F\left(\frac{\partial X}{\partial Z} + R_a\sin\theta_0\frac{\partial \theta_0}{\partial Z}\right) \tag{4.45}$$

We use relations 4.40 and 4.41 in the limit of large separation (implying $\theta_0 \to 0$) to rewrite this last equation as:

$$k_{\mathrm{CNT}}^{\mathrm{peeling}} = -\frac{E_a}{R_a}\left.\frac{\partial X}{\partial Z}\right|_L (\theta_0 \to 0) \tag{4.46}$$

To evaluate the derivative $\partial_Z X|_L$, we combine equations 4.36 and 4.41 to link X and Z in the limit $\theta_0 \to 0$:

$$L - Z = 2(\sqrt{2}-1)R_a = (\sqrt{2}-1)X \tag{4.47}$$

hence

$$\left.\frac{\partial X}{\partial Z}\right|_L (\theta_0 \to 0) = -(1+\sqrt{2}) \tag{4.48}$$

which leads to

$$k_{\mathrm{CNT}}^{\mathrm{peeling}} = (1+\sqrt{2})\frac{E_a}{R_a} \approx 2.4\frac{E_a}{R_a} \tag{4.49}$$

We have demonstrated that the dynamic stiffness should also present a plateau at large separation, the value of which is directly linked to the energy of adhesion and mechanical properties of the CNT. In figure 4.10, we present a numerical integration of the Elastica in the case $L_{\mathrm{CNT}} = 5R_a$,

demonstrating a quite flat peeling stiffness around $2.1E_a/R_a$, close to the value expected from equation 4.49 in the limit $L_{\mathrm{CNT}} \gg R_a$.

This plateau can be used to compute the bending stiffness EI of the nanotube:

$$EI = 2E_a R_a^2 = (6 + 4\sqrt{2})\frac{E_a^3}{(k_{\mathrm{CNT}}^{\mathrm{peeling}})^2} \tag{4.50}$$

The quadratic moment I is a function on the nanotube geometry [82]:

$$I = \frac{\pi D_{\mathrm{CNT}}^3 t_{\mathrm{CNT}}}{8} \tag{4.51}$$

where D_{CNT} is the nanotube diameter and t_{CNT} the wall thickness (0.34 nm for a single wall [81]). From the measurement of EI, we may either extract the Young's modulus E of the nanotube using a known geometry, or use the accepted value $E = 1\,\mathrm{TPa}$ to infer its diameter.

4.5 Point contact state

If the nanotube is now modeled as an elastic line subject to the boundary conditions of equations 4.14 and 4.15 (clamped origin, torque free end), its description is a classic of Elastica textbooks [82]. We will just focus here on two points of interest for our study: we will first show that the repulsive force during compression of the nanotube is small compared to E_a if $L = L_{\mathrm{CNT}} \gg R_a$, and then study the maximum attractive force expected during retraction.

4.5.1 Magnitude of the repulsive force

The repulsive force when pushing the nanotube on the surface can be shown to be an increasing function of the compression z_c. Its maximum $F_{\max}$ is thus reached for the maximum compression before switching to the adsorbed state, that's to say when the nanotube gets tangent to the surface: $\theta_L = \pi/2$. Using boundary condition (4.15) describing torque free point of contact of the nanotube with the substrate, we also have $\theta'_L = 0$. The second invariant of the Elastica (eq. 4.11) evaluated in $s = L$ leads to:

$$\frac{1}{2}EI\theta'^2 - F_{\max}\cos\theta = 0 \tag{4.52}$$

We now adapt again the calculation of the period of a pendulum to our problem using the new boundary conditions. We are interested here in

compression forces ($F > 0$), and will calculate the link between F and L:

$$\left(\frac{\mathrm{d}\theta}{\mathrm{d}s}\right)^2 = \frac{2F_{\max}}{EI}\cos\theta \tag{4.53}$$

$$\mathrm{d}s = \sqrt{\frac{EI}{2F_{\max}}}\frac{\mathrm{d}\theta}{\sqrt{\cos\theta}} \tag{4.54}$$

$$L = \int_0^L \mathrm{d}s = \sqrt{\frac{EI}{2F_{\max}}}\int_{\theta_0}^{\pi/2}\frac{\mathrm{d}\theta}{\sqrt{\cos\theta}} \tag{4.55}$$

$$F_{\max} = \frac{EI}{2L^2}\left(\int_{\theta_0}^{\pi/2}\frac{\mathrm{d}\theta}{\sqrt{\cos\theta}}\right)^2 \tag{4.56}$$

$$F_{\max} \leqslant \frac{EI}{2L^2}\left(\int_{-\pi/2}^{\pi/2}\frac{\mathrm{d}\theta}{\sqrt{\cos\theta}}\right)^2 \tag{4.57}$$

$$F_{\max} \leqslant E_a\frac{R_a^2}{L^2}\left(2\sqrt{2}\mathrm{K}(1/2)\right)^2 \approx 13.7E_a\frac{R_a^2}{L^2} \tag{4.58}$$

where K is the complete elliptic integral of the first kind. Note that this upper bound is divided by two with the simple hypothesis that $\theta_0 = \theta_{\mathrm{AFM}} > 0$. Anyhow, we see that in the limit of a long nanotube with respect to R_a, the maximum repulsive force is much smaller that E_a, the force scale of the problem. Numerical integration of the Elastica presented in Figure 4.9 illustrates this point.

4.5.2 Switching to the adsorbed state

Using the expression of $\mathrm{d}s$ of equation 4.54, we can also compute the ratio $z_c^{\max}/L$ for which this point contact state stops existing. This ratio is:

$$\frac{z_c^{\max}}{L} = \frac{L-Z}{L} = 1 - \int_0^L \cos\theta\mathrm{d}s \Big/ \int_0^L \mathrm{d}s \tag{4.59}$$

$$\frac{z_c^{\max}}{L} = 1 - \int_{\theta_0}^{\pi/2}\sqrt{\cos\theta}\mathrm{d}\theta \Big/ \int_{\theta_0}^{\pi/2} 1/\sqrt{\cos\theta}\mathrm{d}\theta \tag{4.60}$$

These integrals could be expressed in terms of elliptic integrals of the first and second kind, but it is easier to understand the behavior of this ratio $z_c^{\max}/L$ as a function of θ_0 from its plot in figure 4.11. We see that the

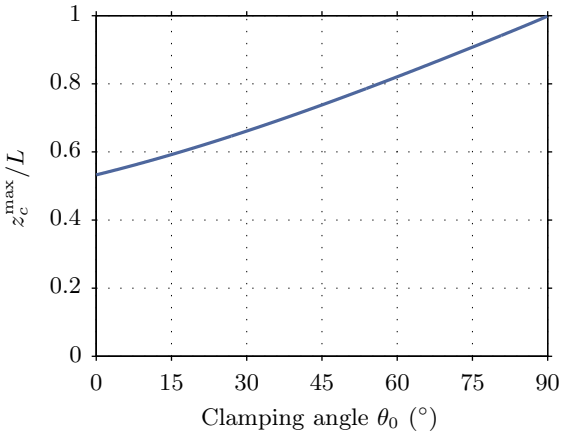

Figure 4.11 – *Maximum compression $z_c^{\max}$ (normalized to nanotube length L) for which the point contact state exists, as a function of the clamping angle θ_0. This curve is obtained from equation 4.60, expressing the ratio z_c/L when the nanotube becomes tangent to the surface at its the contact point.*

greater is the clamping angle θ_0, the longer can last the point contact state when we press the nanotube against a substrate. For θ_0 close to 0, this state will stop existing for compression around half the nanotube length. This behavior may be checked from the direct integration of the Elastica plotted in figure 4.9, where we notice that the point contact state stops existing for $z_c \approx 0.59 L_{\mathrm{CNT}}$, as expected for a 15° clamping.

4.5.3 Breaking the last contact point

During retraction of the nanotube from the surface, one might be surprised to encounter high forces just before the jump out of contact event. Those forces are several times higher than the peeling plateau value, when a long portion of the nanotube is absorbed, whereas this last contact is just attributed to the extremity of the nanotube. We will anyway show that this is to be expected from the adhesion energy.

The extremity in contact with the surface has a characteristic length D_{CNT}, the diameter of the nanotube, thus the expected binding energy is $E_a D_{\mathrm{CNT}}$. As long as the total curvature energy of the nanotube is smaller than this value, the contact will remain stable.

Let us now characterize the curvature energy when we are pulling the nanotube away from the surface. Just before loosing contact, we measure important attractive force ($F < 0$), suggesting that the nanotube is extended, thus almost perpendicular to the surface: $0 < \theta < \theta_0$. We suppose that $\theta_0 = \theta_{\mathrm{AFM}}$ is small, so that we can linearize the Elastica:

$$EI\theta'' = -F\theta \tag{4.61}$$

The solution of this equation, given boundary conditions (4.14) and (4.15), is

$$\theta(s) = \theta_0 \left[e^{-s/l} + \frac{e^{-L/l}}{\cosh(L/l)} \sinh(s/l) \right] \tag{4.62}$$

where $l = \sqrt{-EI/F}$ is the characteristic length of equation 4.61. The second term of this equation can be dropped for large forces: $F < -E_a$ leads to $l < \sqrt{2}R_a \ll L$. We now directly compute the energy of curvature of the line from this asymptotic expression:

$$E_c = \frac{EI}{2} \int_0^L \theta'(s)^2 \mathrm{d}s \approx \frac{EI}{2} \int_0^L \frac{\theta_0^2}{l^2} e^{-2s/l} \mathrm{d}s \approx \frac{EI\theta_0^2}{4l} \tag{4.63}$$

The contact between the nanotube end and the substrate is stable as long as $E_c < E_a D_{\mathrm{CNT}}$, which translates into

$$F > F_{\min}^{\mathrm{curvature}} = -E_a \frac{8}{\theta_0^4} \frac{D_{\mathrm{CNT}}^2}{R_a^2} \tag{4.64}$$

In the limit of small clamping angle $\theta_0 \to 0$, the contact point would be stable up to diverging forces in this description. In such a case, we should also consider the elastic energy E_e, due the deformation along the axis [82]:

$$E_e = \frac{1}{2} \frac{L}{E\pi D_{\mathrm{CNT}} t_{\mathrm{CNT}}} F^2 \tag{4.65}$$

Using the same stability criterium $E_e < E_a D_{\mathrm{CNT}}$, she easily show that the contact is stable as long as:

$$F > F_{\min}^{\mathrm{elasticity}} = -E_a 4 \sqrt{\frac{2R_a^2}{L D_{\mathrm{CNT}}}} \tag{4.66}$$

Let us compute the numerical values of these 2 stability limits. We use for R_a and D_{CNT} the results of the measurement described further (table 4.1), for a nanotube over graphite: $R_a = 59\,\mathrm{nm}$ and $D_{\mathrm{CNT}} = 3.7\,\mathrm{nm}$.

We use the full length visible in figure 4.1 for the nanotube length since under tension every portion of the nanotube should contribute to the elastic energy: $L = 2\,\mu$m. As for the clamping angle θ_0, we will use the value $\theta_{\mathrm{AFM}} = 15°$, due to the angle between the substrate an the AFM cantilever. We estimate:

$$F_{\min}^{\text{curvature}}/E_a \sim -6.7 \tag{4.67}$$

$$F_{\min}^{\text{elasticity}}/E_a \sim -3.9 \tag{4.68}$$

We see that in this case, the elastic energy will be the first to overcome the binding energy of the nanotube end with the surface, and the computed value for the maximum pulling force before rupture of the link is very close to the observation (see figure 4.5).

4.6 Numerical integration of the Elastica

The Elastica is a non linear ordinary differential equation (ODE) of the second order, and its solutions do not have a simple analytical expression for most boundary conditions. It is therefore useful integrate it numerically, to go beyond the limit cases treated with the analytical description. We implemented this task using Matlab built-in ODE solver `bvp4c` (Matlab script in Appendix C.2).

The control parameter in the experiment is the nanotube compression z_c, which appears as an integral constraint (equation 4.5) in the analytical formulation. F should be adjusted to fulfill this constraint. This is clearly not an ideal control parameter for the simulation, so we adopt the inverse strategy: we compute the family of solutions for an adequate range of force F, then calculate the corresponding z_c, and just switch the axes when plotting the results.

The simulation for the point contact state is straightforward, since there are no other adjustable parameters. The adsorbed case has an additional step, since the length L of the free standing part of the nanotube has to be tuned to balance adhesion and curvature energies. However, the usual boundary conditions (θ fixed or $\theta' = 0$) are independent of the nanotube length, so we normalize the simulated equation using: arc length $\hat{s} = s/L$, compression $\hat{z_c} = z_c/L$, force $\hat{f} = FL^2/EI$, curvature energy $\hat{e}_c = E_c L/EI$. The normalized Elastica reads

$$\frac{\mathrm{d}^2\theta}{\mathrm{d}\hat{s}^2} = -\hat{f}\sin\theta \tag{4.69}$$

From its numerical integration using the appropriate boundary conditions, we obtain for each force $\hat{f}$ the shape of the solution $\theta(\hat{s})$, the corresponding compression $\hat{z_c}$ and curvature energy $\hat{e}_c$. For a given z_c, the value of the length L of the free standing part of the nanotube realizes the minimum of the total energy E_{CNT} (equation 4.16). Let us express E_{CNT} using normalized quantities:

$$E_{\mathrm{CNT}} = \hat{e}_c(\hat{z})\frac{EI}{L} + (L - L_{\mathrm{CNT}})E_a \tag{4.70}$$

$$= EI\hat{e}_c(\hat{z_c})\frac{\hat{z_c}}{z_c} + E_a\frac{z_c}{\hat{z_c}} - E_a L_{\mathrm{CNT}} \tag{4.71}$$

Using this formulation, we can easily find the value of $\hat{z_c}$ corresponding to the minimum of E_{CNT} for a given z_c.

To avoid any quantization effect, we do not limit this minimization to the computed values of $\hat{z_c}$: for a given z_c, we first find the minimum within the computed values, then fit E_{CNT} versus $\hat{f}$ on a few values around this minimum with a parabola. The lowest point of this fit leads to the adequate value of $\hat{f}$, for which we integrate one more time the normalized Elastica. Knowing z_c, the resulting value of $\hat{z_c}$ leads to that of L and every other quantity of interest for the adsorbed state. The Matlab code corresponding to this strategy can be found in Appendix C.2. Some illustrations of the numerical integration of the Elastica are shown in figures 4.9, 4.10 and 4.12.

4.7 Analysis of experimental data

4.7.1 The global picture from the Elastica

Let us summarize the main points we have analytically demonstrated. We use the Elastica to model the nanotube shape, and an adsorption energy per unit length E_a to model the interaction with the substrate. The experimental control parameter corresponds to the nanotube vertical compression z_c, and the system can switch between 3 different states:

- No contact
- Point contact — only the end of the nanotube is in contact with the substrate.
- Adsorbed — A finite length of the nanotube is in contact with the substrate.

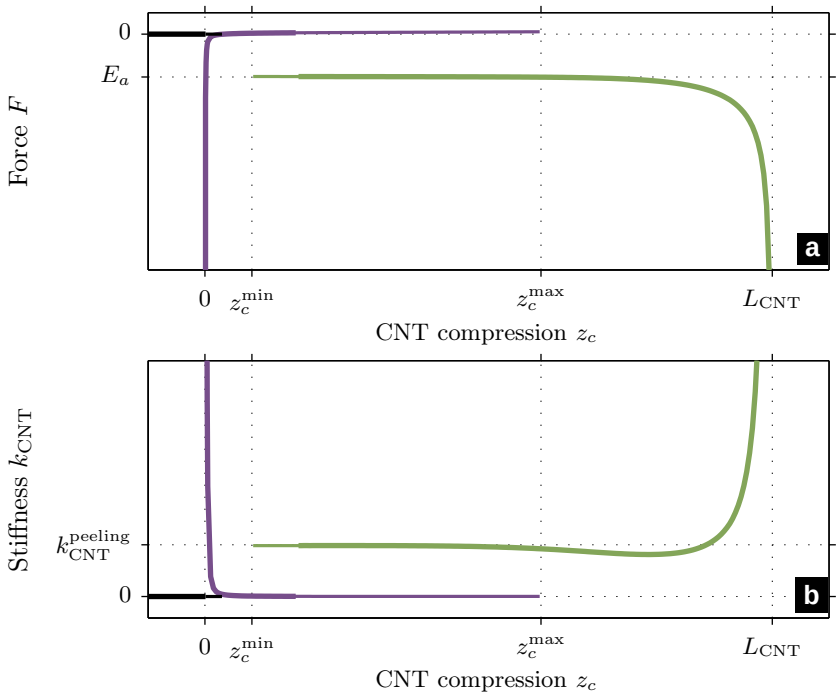

Figure 4.12 – *Numerical inegration of CNT compression for $L = 10R_a$ and torque free origin in absorbed state. Fundamental and metastable states are respectively drawn as thick and thin lines. Force F (**a**) and dynamic stiffness k_{CNT} (**b**) as a function of compression. When cycling Z, the nanotube switches between straight shape (black), weakly bended state (purple), and adsorbed state (green), presenting large force and dynamic stiffness plateau except for the highest compressions, where $F \to -\infty$. All characteristic points of the curves can be computed analytically in the limit $L \gg R_a$, and are noted on the graphics. The highest compression for which the point contact state exists is given by $z_c^{\max}$ (equation 4.60) and associated to an almost zero force (equation 4.58). The lowest compression which the adsorbed state exist is given by $z_c^{\min}$ (equation 4.36), and ends the force and stiffness plateaux of values E_a and $k_{\mathrm{CNT}}^{\mathrm{peeling}}$ (equation 4.26 and 4.49, respectively).*

The adsorbed state defines a natural scale of the problem: R_a, the radius of curvature of the nanotube at the contact point with the substrate, resulting from a balance between adsorption and curvature. The analysis has been conducted in the limit of long nanotubes with respect to this length: $R_a \ll L_{\mathrm{CNT}}$.

Our main findings are summarized in figure 4.12, where we present the force and stiffness versus compression curves, numerically integrated for the model of an elastic line with $R_a = 0.1 L_{\mathrm{CNT}}$. During approach, the nanotube will first adopt a weakly bended shape, resulting in a repulsive force that is small compared to E_a (see paragraph 4.5.1). As the compression is increased, this state turns metastable, but may remain till the end of the nanotube gets tangent to the substrate. The value of the compression $z_c^{\max}$ at this point can be estimated with equation 4.60. For larger compression, this branch of solution stops existing and part of the nanotube will be absorbed on the surface, on a force plateau close to the value of E_a (paragraph 4.4.1). As the suspension point is brought closer to the surface, the force exhibit a divergence towards $-\infty$ (paragraph 4.4.2, case 2).

During retraction, the adsorbed shape will remains stable or metastable as long as the absorbed length is non zero, the force presenting the peeling plateau expected when the free standing length is larger than R_a. The dynamic stiffness k_{CNT} also presents a plateau, the value of which is linked to the mechanical properties of the nanotube (paragraph 4.4.4). For a compression $z_c^{\min}$ a bit smaller than R_a (equation 4.36), the absorbed state disappear, the force jumps close to 0 as the nanotube recover a weakly bended shape. Further retraction eventually leads to a fully extended nanotube (perpendicular to the surface), probing high binding forces as the longitudinal response start being solicited. The connection with the substrate will finally break, for a force a few times larger than E_a (paragraph 4.5.3). The phenomenology expected from this model is very close to the experimental observations, as shown by the similarity between figures 4.10 and 4.5 or 4.6.

4.7.2 Extracting information from the measurements

Using this global picture from the Elastica, let us have a closer look at the information we can extract from figures 4.5 to 4.7. We will restrict the analysis to the first part of the curve, using the hypothesis that the nanotube is composed of several ideal segments linked by defects presenting high flexibility. The length of the portion under test is thus about 300 nm long, the upper part of the nanotube (about 2 μm long) acting mainly as suspension point that can freely move laterally.

A first point of interest in the force-compression curves is $z_c^{\max}$, the maximum compression before the transition to the adsorbed state. We read on figure 4.5 to 4.7 $z_c^{\max} \approx 230\,\mathrm{nm}$, which leads to $z_c^{\max}/L_{\mathrm{CNT}} \approx 0.8$. According to figure 4.11, this would correspond to a clamping angle of the origin around 55°. This is clearly much larger than what can be expected from the TEM image of figure 4.1, and yet another hint that the segment probed here is weakly connected to the upper part of the nanotube.

In part 4.2.3, we already associated the plateaux of the force-compression curves with the adsorption energy per unit length, and estimated $E_a^{\mathrm{HOPG}} \simeq 0.98\,\mathrm{nJ/m}$ for a graphite substrate, and $E_a^{\mathrm{mica}} \simeq 0.42\,\mathrm{nJ/m}$ for mica (see details in table 4.1). The peeling plateau for stiffness, as well, can be read on figures 4.5 and 4.6, and used with equation 4.49 to infer the radius of curvature at the adsorption point[2]: we estimate $R_a^{\mathrm{HOPG}} \simeq 59\,\mathrm{nm}$ for a graphite substrate, and $R_a^{\mathrm{mica}} \simeq 72\,\mathrm{nm}$ for mica. The ratio R_a/L_{CNT} is thus of order 1/5, corresponding to the numerical integration of the Elastica of figure 4.10. Note that if the adhesion process is not completely frozen at the frequency we are probing in our estimation of k_{CNT}, the actual dynamic stiffness would be larger (hence R_a smaller) than the value measured here.

Another way to estimate R_a is to measure the distance between the last point before loosing adhesion and the fully extended nanotube: for a ratio $R_a/L = 0.2$, $z_c^{\min} \approx 0.85 R_a$. In fact, as the last adhesion point is a metastable state (corresponding to a vanishing adsorbed length), the estimation we get through this observation gives only an upper bound to R_a. This leads to $R_a^{\mathrm{HOPG}} \lesssim 90\,\mathrm{nm}$ and $R_a^{\mathrm{mica}} \lesssim 115\,\mathrm{nm}$, values that are coherent with the estimation through the dynamic stiffness.

Using equation 4.50, we can compute from the previous estimations of E_a and R_a the value of the bending stiffness EI. Assuming for the Young's modulus a value $E = 1 \times 10^{12}\,\mathrm{Pa}$ [81], we can deduce from equation 4.51 the diameter D_{CNT} for the nanotube segment probed in this experiment. We report in table 4.1 the estimations we get from measurements on graphite and mica, leading to $D_{\mathrm{CNT}} \sim 3.5\,\mathrm{nm}$. This size is close to the expected diameter for our nanotubes.

4.7.3 Comparison to other techniques

As mentioned in the introduction of this chapter, although the adhesion of carbon nanotube and other nano-objects is of great practical interest, very

[2] As seen on figure 4.10, a small correction has to be considered with respect to equation 4.49: the numerical pre-factor $(1+\sqrt{2})$, valid in the limit $R_a \ll L_{CNT}$, is closer to 2.1 in the case $R_a/L_{CNT} = 0.2$.

Substrate	HOPG	mica
E_a (nJ/m)	0.98 ± 0.07	0.42 ± 0.04
$k_{\mathrm{CNT}}^{\mathrm{peeling}}$ (N/m)	0.036 ± 0.007	0.013 ± 0.003
R_a (nm)	59 ± 10	72 ± 15
EI (10^{-24} Jm)	7.1 ± 2.5	4.5 ± 2.1
D_{CNT} (nm)	3.7 ± 0.4	3.2 ± 0.5

Table 4.1 – *Measured values for the adhesion energy per unit length E_a, dynamic spring constant plateau $k_{\mathrm{CNT}}^{\mathrm{peeling}}$, radius of curvature at adhesion point R_a, bending modulus of the nanotube EI and estimated nanotube diameter D_{CNT} for two different substrates. Data correspond to mean values and standard deviations on the plateau of force and stiffness for compression z_c in the $(80-220)$ nm range for graphite, and $(120-280)$ nm range for mica, for the measurements presented in figures 4.5 and 4.6.*

few experiments have been successful in providing quantitative information. A few others using peeling protocols have also been very instructive about the adhesion processes, but imply complex data analysis that prevents reliable access to quantitative characterization. We will first quickly review other significative experiments we are aware of, then compare our results and stress the difference of our technique with respect to other peeling tests.

4.7.4 Quick review of nanotube adhesion in the literature

Calculation based on a Lennard-Jones potential describing the graphite system [56] have been extended by Girifalco and coworkers [57] to the case of nanotube and C_{60} interactions, leading to the definition of a universal graphitic potential. This theoretical approach evaluates the graphene/graphene interaction to $0.33\,\mathrm{J/m^2}$, and the energy of adhesion per unit length between parallel nanotubes to $E_a = (-0.406\sqrt{D_{\mathrm{CNT}}/(\mathrm{nm})} + 0.015)\,\mathrm{nJ/m}$. For SWNT of diameter $D_{\mathrm{CNT}} = 1.4\,\mathrm{nm}$ for example, the nanotube-nanotube interaction is estimated to $E_a = 0.45\,\mathrm{nJ/m}$.

Hertel and coworkers [63, 64], imaged by AFM the shape of crossed CNT adsorbed on a H-passivated silicon (100) substrate. The top nanotube profile balances the increase of curvature energy and the loss of surface energy in this configuration, providing an estimation of the adhesion energy if the CNT mechanical properties are assumed. For multiwall nanotubes with diameters around 10 nm, the estimated adhesion en-

ergy is $E_a = (1.3 \pm 0.5)\,\mathrm{nJ/m}$. Using molecular-mechanics calculations, they also obtain an estimation for a rigid nanotube on graphite: $E_a = -0.085\,\mathrm{nJ/m} + 0.14\,\mathrm{J/m^2} \times D_{\mathrm{CNT}}$, in very good agreement with their experimental observation (although the substrate is different).

Benedict and coworkers [15], observed with TEM collapsed multi-wall nanotubes (MWNT) [33]. The shape of the section of those objects is a balance between the adhesion of the collapsed section and the curvature of the edges. Their typical nanotube size is $D_{\mathrm{CNT}} = (10 - 15)\,\mathrm{nm}$, formed by 6 to 8 walls. The magnitude of interlayer cohesive energy per unit surface is evaluated around $(0.15 - 0.24)\,\mathrm{J/m^2}$.

Chen and coworkers [31] study the interaction between two separate carbon nanotubes that are bonded together by examining the geometry of the point of connexion. Assuming the diameter of the two double wall nanotubes (4 nm) and their Young's modulus, they estimated from the Y shape analyzed within the Elastica framework a binding energy of $0.36\,\mathrm{nJ/m}$.

Kis and coworkers [80] performed a direct measurement using an AFM tip to pull the inner core of a telescopic multi wall nanotubes (MWNT) [36], with TEM visualisation. Their experiment demonstrated a friction free interaction between the concentric layers, and provides an estimation of the adhesion for this very specific geometry of concentric nanotubes. For a 5 nm MWNT, they measure from the force plateau $E_a = (2 - 3)\,\mathrm{nJ/m}$, leading to an adsorption energy per unit surface of $(0.14 - 0.2)\,\mathrm{J/m^2}$.

Strus and coworkers [134, 135] performed peeling experiments on graphite and polymer substrates. A MWNT is attached at the extremity of a tip-less AFM cantilever, parallel to it. It is then pressed on the substrate, and easily adsorbed since it is presented almost tangentially. The force curve during approach and retraction present a characteristic signature for point contact and adsorbed states, though the geometry (clamping angle at the origin almost parallel to the surface) makes this signature complex to interpret (see Figure 4.13). Moreover, the snap-in instability of the cantilever itself hides part of the peeling process. A global adhesion energy can be estimated from the integral of the hysteresis of part of the force curve, but the length of the nanotube that is implied is unknown. Using the full nanotube length, they reach a lower bound for the adsorption energy per unit length, which is $E_a > 1.1\,\mathrm{nJ/m}$ for a MWNT of outer diameter $D_{\mathrm{CNT}} = (40 \pm 6)\,\mathrm{nm}$, inner diameter $(10 \pm 2)\,\mathrm{nm}$, and a substrate of graphite [114]. They suggest that the peeling method could be quantitative if one could also monitor the length of nanotube in contact with the sample. The analysis is complicated by several transitions between different adsorbed states, hinting at their nanotubes also presenting some weak bending points, just like ours.

Ishikawa and coworkers [70, 71] perform peeling experiments on graphite with self sensing AFM cantilever inside a scanning electron microscope, in an attempt to monitor simultaneously the peeling force and the shape of the adsorbed nanotube. The nanotube clamping is similar to the experiment of Strus and coworkers [134, 135], the force curve analysis thus suffers from the same complexity. The total cycle energy, including peeling and energy losses during the process (friction, curvature energy suddenly released on conformational changes, etc.) is 1.2×10^{-14} J for a MWNT whose length and diameter are $L_{\mathrm{CNT}} = 3\,\mu$m and $D_{\mathrm{CNT}} = 30$ nm. If the whole length is implied and energy losses are neglected, the energy of adhesion per unit length is $E_a = 4$ nJ/m.

Finally, Ke and coworkers [77], are peeling with a nano-manipulator a bundle of a few SWNT from a larger free standing one. Using SEM and TEM imaging, they interpret the shape of the delaminated bundle with an Elastica description, leading to a measurement of E_a/EI for the bundle. Assumption on EI from observations of the bundles of SWNT of diameter $D_{\mathrm{CNT}} = 1.3$ nm leads to nanotube-nanotube interaction of $E_a = (0.13 - 0.16)$ nJ/m.

4.7.5 Comparison of peeling procedures

As can be seen from this quick review, our method leads to a value of E_a in reasonable agreement with other protocols for quite similar systems. The incertitude is however reduced by our approach, which is self sufficient: there is no need from extra information implying other measurements, to evaluate the mechanical properties of the nanotube or the geometry of the contact with the substrate.

Other peeling experiments [70, 71, 134, 135] using AFM detection are based on a parallel geometry : the clamping of the nanotube is almost parallel to the surface (see Figure 4.13). The benefit of this approach is that the adsorbed state is natural, and can be reached for any rigidity of the nanotube. However, according to the authors, extracting quantitative information from the force curve would require a simultaneous precise observation of the shape of the nanotube, which is a very complex task (even more for SWNT). Moreover, friction may play a non negligible but hard to characterize role in the peeling process.

In our approach, the clamping of the nanotube is close to being perpendicular to the surface. While at first glance it seems counterintuitive to use such a configuration to measure absorption properties, it turns out to ease the interpretation of the experimental data, as the force plateaux

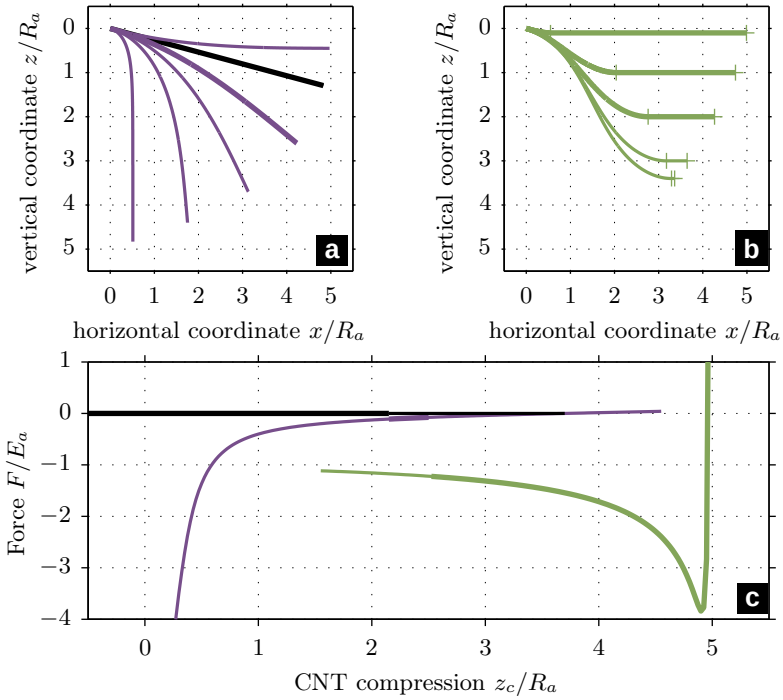

Figure 4.13 – *Numerical integration of CNT compression for $L = 5R_a$ and clamped origin almost parallel to the substrate (15° inclination), corresponding to peeling protocols of references [70, 71, 134, 135]. Shape for point contact and adsorbed state are ploted in (**a**) and (**b**), while (**c**) presents the force F as a function of compression. When cycling Z, the nanotube switches between straight shape (black), weakly bended state (purple), and adsorbed state (green). Fundamental and metastable states are respectively drawn as thick and thin lines. For the point contact state, an adsorption energy corresponding to a contact length of $R_a/13$ has been considered to compute the metastability limits (see paragraph 4.5.3). No obvious force plateau corresponding to E_a can be read on this force-compression curve: for relatively short nanotubes, the quasi-horizontal clamping condition at the origin is less efficient to access quantitative information than the quasi vertical (see figure 4.9) or torque free clamping (see figure 4.10) corresponding to our experiment.*

provide a direct reading of the energy of adsorption per unit length E_a. The only requisite of our method is to have a nanotube longer than R_a, the natural radius of curvature at the peeling point. In this limit, friction forces have little impact on the measurements: the free standing part of the nanotube presents a weak horizontal rigidity, letting the horizontal force relax to small values. In fact, we have demonstrated in section 4.4.1 that in the limit $L_{\mathrm{CNT}} \ll R_a$, the force plateaux should be present for any clamping condition at the origin. A vertical or weak (torque free) clamping is however helpful as it enlarges the compression range for which the plateau can be observed. A good illustration of this point is given by comparison between figures 4.9, 4.10 and 4.13, all corresponding to a numerical integration of CNT compression for $L = 5R_a$ but using different clamping conditions at the origin. Peeling protocols should therefore benefit from adopting such a configuration, either using appropriate clamping of CNT on a AFM cantilever tip, or adopting more specialized tools as nanotweezers [144].

4.8 Conclusions and perspectives

In this last section, let us first summarize the main points of this chapter:

- We perform a series of experiments where a single wall carbon nanotube is pushed almost perpendicularly against a substrate of graphite or mica. We measure the quasi-static force as a function of the compression, and we can also access the dynamic stiffness using an analysis of thermal noise during this process. The most striking feature of these two observables is a plateau curve for a large range of compression, the values of which are substrate dependent.

- We use the Elastica to describe the shape of the nanotube, and a simple energy of adhesion per unit length E_a to describe the interaction with the substrate. A natural length R_a is defined using this approach, corresponding to the radius of curvature at the last point of the free standing part of the nanotube when a non zero length is adsorbed on the substrate. We analytically derive a complete description of the expected behavior in the limit of long nanotubes with respect to R_a, and numerically integrate the Elastica for intermediate lengths.

- The analysis of the experimental data within this simple framework naturally leads to every quantity of interest in the problem (see table 4.1): the force plateau is a direct measurement of the energy of adhesion per unit length E_a for each substrate, and we easily determine

R_a from the dynamic stiffness plateau. Mechanical properties of the nanotube itself (its bending stiffness EI) can be extracted from those values, and prove to be independent of the substrate.

This method has thus proved to be a very valuable tool to characterize both the nanotubes and their interaction with a substrate. It can easily be applied to other materials or environmental conditions, to gather data of interest for technological applications of nanotubes or nanowires. The key point for the method to work is a weak rigidity with respect to adsorption: the radius of curvature at the adsorption point should be small compared to the length of the nanotube.

A number of questions still have to be addressed to have a complete understanding of the physical processes of adhesion: what is the characteristic time scale of adhesion ? What are the associated dissipation processes ? What can we learn with similar experiments about the friction of the nanotube on the substrate ? A number of experiments are already foreseen to answer those questions, that will imply vertical and horizontal oscillations of the sample to test the frequency response of the adsorbed nanotube.

Chapter 5

Conclusion

This mémoire presents my current research interests in micro and nano-mechanics in a comprehensive manuscript. A first chapter describes our atomic force microscope (AFM) and its innovative detection system that has been designed and realized in our laboratory. Its quadrature phase differential interferometer allows the measurement of the fluctuations of micro-cantilevers with an outstanding resolution, and is used in the second chapter to study their mechanical properties. Dissipation processes as well as elastic response are precisely characterized through measurements of the thermal noise of the system. In the last chapter, we study the mechanical properties of carbon nanotubes (CNT) in interaction with a substrate. These nano-peeling experiments proved to be very rich, with a quantitative access to both the intrinsic mechanical properties of the CNT and to the interaction potential with the surface. Before mentioning the perspectives of this work, let me summarize the main results of each chapter.

The first chapter presents our experimental device: a home made atomic force microscope whose detection is based on a quadrature phase differential interferometer. Several strategies to sense the deflexion are described: the bi-calcite setup features a small environmental susceptibility, and is used for low frequency thermal noise studies, while the Wollaston configuration allows calibrated measurements on a wide spectral range. The quadrature phase design enables a very high resolution (down to $10^{-14}\,\mathrm{m}/\sqrt{\mathrm{Hz}}$), equaling or out-performing the best results reported in the literature for a much larger deflexion range (up to a few μm). The dual output of the interferometer implies a specific handling to interface common scanning probe microscope controllers. We developed analog circuitries to tackle static (contact

mode) and dynamic (tapping mode) operations, and we demonstrate their performance by imaging a simple calibration sample.

The second chapter first introduces a few useful tools in order to study the mechanical behavior of a cantilever from its fluctuations. The keystone of the analysis is the Fluctuation-Dissipation Theorem (FDT), relating the thermal noise spectrum to the dissipative part of the response. Using Kramers-Kronig relations, we show that we can compare theoretical models and experimental data both in terms of noise spectra and of mechanical response. We apply this strategy to compare Sader's model for viscous dissipation with measurements on raw silicon cantilevers in air, demonstrating an excellent agreement. When a gold coating is present on the cantilever, the low frequency behavior is strongly modified, the thermal noise presenting a $1/f$ like trend. We demonstrate this behavior to be the signature of a viscoelastic dissipation process in the cantilever. We provide a quantitative phenomenological description of this effect : a simple power law is found to describe accurately the frequency dependence of the viscoelastic dissipation. In a last section, we characterize the mechanical properties of cantilevers from a mapping of the thermal noise on their surface. This analysis validates the description of the system in term of its normal modes of oscillations in an Euler-Bernoulli framework for flexion and in Saint-Venant approach for torsion. The correct description of the dispersion relation for torsional modes however lead to the introduction of Barr's refined model to account for the observations at high mode numbers. The cantilever stiffness can be precisely measured from this approach, as well as the elastic coefficients E (Young's modulus) and S (shear modulus) of its constituting material.

The last chapter presents peeling experiments on a single wall carbon nanotube, attached to the cantilever tip. It is pushed almost perpendicularly against a substrate of graphite or mica. We measure the quasi-static force as a function of the compression, and we can also access the dynamic stiffness using an analysis of the thermal noise during this process. The most striking feature of these two observables is a plateau curve for a large range of compression, the values of which are substrate dependent. We use the Elastica to describe the shape of the nanotube, and a simple energy of adhesion per unit length E_a to describe the interaction with the substrate. A natural length R_a is defined using this approach, corresponding to the radius of curvature at the last contact point when a non zero length on the nanotube is adsorbed on the substrate. We analytically derive a complete description of the expected behavior in the limit of long nanotubes with respect to R_a, and numerically integrate the Elastica for intermediate lengths.

The analysis of the experimental data within this simple framework naturally leads to every quantity of interest in the problem: the force plateau is a direct measurement of the energy of adhesion per unit length E_a for each substrate, and we can easily determine R_a from the dynamic stiffness plateau. Mechanical properties of the nanotube itself (its bending stiffness EI) can be extracted from those values, and prove to be independent of the substrate.

The low noise of our interferometer, as well as its intrinsic calibration, are obviously central in these various experiments : none of the results we presented in this manuscript could have been characterized with the classic optical lever scheme of commercial AFMs. The access to the thermal noise spectrum outside resonances is for instance a key point in the evaluation of the dissipation processes of cantilevers. The use of thermal noise is in itself a key point, since we don't need to determine exactly the transfer function of the external forcing method which is usually necessary to measure a response function. In the presented research topics, it results in an innovative approach to evaluate the mechanical behavior of the system. Using the same geometries, this method could be applied to other materials or environmental conditions, to gather data of interest for technological applications of cantilever based sensors or nanotubes and nanowires. Our interferometric setup could thus find a very useful place next to the scarce tools for dynamic metrology at nanoscale.

Next...

Apart a natural continuation of the research interests mentioned along this manuscript, one of the main project we have for the next years is the experimental study of adhesion at nanoscale. We will focus on two cases of huge practical importance:

- Capillary forces, arising from the condensation of a liquid from its undersaturated vapor in a confined geometry, present a considerable interest both for fundamental physics and industrial applications [72]: fundamentally, the study of capillary condensation provides an useful test bench to investigate a number of major questions of statistical physics, as the competition between surface and finite-size effects [18], the role of disorder [21], or the hysteresis and slow nucleation dynamics associated with any first order phase transition. As for applications, forces associated with capillary bridges are deeply implied in a broad range of phenomena, as the cohesion of divided matter [47, 67], the creep of composite materials such as plaster, the fracture of mate-

rials (rocks, concrete, glass...) [85, 141], the storage and transport in porous materials [86], the aging of mechanical contacts in tribology [20, 44], or stiction (destruction by adhesion and friction) in micro (or nano) electromechanical systems (MEMS or NEMS) [16, 83, 92].

- Van der Waals (VdW) forces, are undoubtedly a key point in understanding and controlling the behavior of nano-systems. Such devices present indeed a high surface to volume ratio, so that surface effects become more and more important as technology progresses towards smaller and smaller systems. Carbone nanotubes for instance mainly interact through VdW forces with their environment. To harness their unique mechanical and electrical properties [5], understanding their interaction with the rest of the world is certainly of prime importance. The growing number of their (foreseen) applications, from fillers in high-strength composites to components of nanoscale electronics and mechanics [5, 81], or their generic use as a bench system to study fundamental physical phenomena on the mesoscopic scale make them a piece of choice for the study of VdW interaction.

It is thus of prime interest to understand the physics of adhesion in these two cases, both for fundamental and practical reasons. Direct measurements of force-distance profiles between two interacting surfaces are a priori a very powerful way to study these attractive forces, as they offer a direct access to the potential energy of the interaction as well as quantitative values of practical interest [72]. However, this approach has been severely impeded by the intrinsic difficulty of accessing attractive forces by surface force measurements techniques (typically Surface Force Apparatus or AFM), due to a mechanical instability: the finite compliance of the force sensor is problematic in the lowest (and most interesting) range of distance. Very few experiments [30, 80, 111, 142], restricted to special configurations, managed to overcome this obstacle so far, and this project proposes an answer to this experimental challenge.

Our innovative AFM, with its outstanding sensitivity can be used to overcome the intrinsic difficulty of attractive force measurements: cantilevers much stiffer can be used, preventing the mechanical instability to occur without sacrificing too much of the force resolution. The full force versus distance curve can therefore be explored, and adhesion forces can be directly characterized. For the first axis of this project, measurements of capillary forces will be carried out in order to investigate several questions of both fundamental and applied interest, more especially: the influence of disorder on wetting and prewetting transitions, the mechanical properties of

capillary bridges from nano-scale to microscale, and the slow nucleation dynamics of capillary bridges and the associated hysteresis phenomena. This project will be conducted in collaboration with Audrey Steinberger, who has been hired as a CNRS researcher in 2009 with a project focused on capillary adhesion and fluctuations in confined phase transitions.

The second axis of the project, on Van der Waals forces, is in continuation of our preliminary work on nanotube peeling. The procedure described in chapter three will be extended to other nano-objects, like nanowires for example. A number of questions still have to be addressed to have a complete understanding of the physical processes of adhesion: what is the characteristic time scale of adhesion ? What are the associated dissipation processes ? What can we learn with similar experiments about the friction of the nanotube on the substrate ? A number of experiments are already foreseen to answer those questions; they will imply vertical and horizontal oscillations of the sample to test the frequency response of the adsorbed nanotube. Tianjun Li, recently graduated from the East China Normal University (ECNU), is starting a PhD thesis in joint supervision between the ENS Lyon and the ECNU on this topic, under the supervision of Zhuo Sun and myself.

On a more technical level, some of the objectives mentioned above require an excellent control of the distance between the probe (AFM tip, colloidal particle or nanotube) and the reference surface (substrate). As in most AFM setups, we currently rely on the piezo translating the sample to infer this separation. This technique suffers from slow environmental drifts which degrades its long time accuracy. We thus need to measure independently the probe-surface distance, and if needed use this information as a retroaction signal to drive the sample position and keep the distance at the desired value. For this, we will build a second differential interferometer with performances similar to the one used for deflexion measurement. Felipe Aguilar, recently graduated in the University of Santiago de Chile (USACH), is starting a PhD thesis in joint supervision between the ENS Lyon and the USACH around the further instrumental development of the AFM, under the supervision of Francisco Melo and Myself. This topic should provide our experimental setup other unique features with respect to commercial devices, and could open many research tracks beyond our current projects.

Appendices

Appendix A

Quadrature phase interferometer

A.1 Dynamic mode with large oscillations

In this appendix, we deal with the case of oscillations that are not small compared to the wavelength in dynamic mode. The link between the filtered contrast $\tilde{C}_n^0 = \langle C_n \rangle$ and the filtered phase $\varphi_0 = \langle \varphi \rangle$ is now not trivial. Indeed, let us compute $\tilde{C}_1^0$ from eq. 2.12:

$$\begin{aligned} \tilde{C}_1^0 &= \langle \mathcal{C}_1 \cos(\varphi_0 + \delta\varphi) \rangle & \text{(A.1)} \\ &= \mathcal{C}_1 \langle \cos(\varphi_0)\cos(\delta\varphi) - \sin(\varphi_0)\sin(\delta\varphi) \rangle & \text{(A.2)} \\ &= \mathcal{C}_1 (\cos(\varphi_0) \langle \cos(\delta\varphi) \rangle - \sin(\varphi_0) \langle \sin(\delta\varphi) \rangle) & \text{(A.3)} \end{aligned}$$

As well, C_2^0 is given by

$$\tilde{C}_2^0 = \mathcal{C}_2 (\sin(\varphi_0 + \psi) \langle \cos(\delta\varphi) \rangle + \cos(\varphi_0 + \psi) \langle \sin(\delta\varphi) \rangle) \quad \text{(A.4)}$$

As soon as $\langle \sin(\delta\varphi) \rangle \neq 0$, which is the case when φ is anharmonic, we see that the additional terms in the expressions of $\tilde{C}_n^0$ will proscribe the use of eq. 2.12 to compute φ_0.

Let us introduce M and α, both dependent on $\delta\varphi$ such that

$$M e^{i\alpha} = \left\langle e^{i\delta\varphi} \right\rangle = \langle \cos(\delta\varphi) \rangle + i \langle \sin(\delta\varphi) \rangle \quad \text{(A.5)}$$

α will reflect the anharmonicity of the oscillation. The contrasts C_n can

now be rewritten as

$$\tilde{C}_1^0 = \mathcal{C}_1 M \cos(\varphi_0 + \alpha) \quad \text{(A.6)}$$

$$\tilde{C}_2^0 = \mathcal{C}_2 M \cos(\varphi_0 + \psi + \alpha) \quad \text{(A.7)}$$

Using this notation clearly demonstrate that the averaging process will bias the estimation of the average optical phase φ_0 by α. As well, U_{AC} defined by eq. 2.15 can be computed as:

$$U_{AC} = M\mathcal{C}_1\mathcal{C}_2 \cos(\psi) \sin(\delta\varphi - \alpha) \quad \text{(A.8)}$$

Again, as soon as $\langle \sin(\delta\varphi) \rangle \neq 0$, the relation between U_{AC} and $\delta\varphi$ is non trivial. If this quantity is still independent from the working point (the value of φ_0), it is hard to interpret simply when $\delta\varphi$ is not much smaller than one. It may be used for imaging, but at the expense of a much harder interpretation of the measured values when the interaction changes during the scan.

Appendix B

Around Kramers Kronig

B.1 Jonscher like stiffness

Let $k(\omega) = \mathrm{Re}[k(\omega)] + i\,\mathrm{Im}[G(\omega)]$ be a response function in Fourier space. Causality implies that $k(\omega)$ obeys the Kramers-Kronig relations :

$$\mathrm{Re}[k(\omega)] = \frac{1}{\pi}\mathcal{PP}\int_{-\infty}^{\infty}\frac{\mathrm{Im}[k(\Omega)]}{\Omega-\omega}\mathrm{d}\Omega \tag{B.1}$$

$$\mathrm{Im}[k(\omega)] = -\frac{1}{\pi}\mathcal{PP}\int_{-\infty}^{\infty}\frac{\mathrm{Re}[k(\Omega)]}{\Omega-\omega}\mathrm{d}\Omega \tag{B.2}$$

Following the experimental observation of the power law dependence of $\mathrm{Im}\left[G^{\mathrm{vacuum}}(\omega)\right] = \mathrm{Im}[k(\omega)]$, we write

$$\mathrm{Im}[k(\omega)] = K_i\omega^{\alpha} \tag{B.3}$$

where K_i is a real constant. Relation B.1 implies for the real part:

$$\mathrm{Re}[k(\omega)] = \frac{1}{\pi}\mathcal{PP}\int_{-\infty}^{\infty}\frac{K_i\Omega^{\alpha}}{\Omega-\omega}\mathrm{d}\Omega \tag{B.4}$$

A change of variable with $\varpi = \Omega/\omega$ leads to

$$\mathrm{Re}[k(\omega)] = \left[\frac{1}{\pi}\mathcal{PP}\int_{-\infty}^{\infty}\frac{K_i\varpi^{\alpha}}{\varpi-1}\mathrm{d}\varpi\right]\omega^{\alpha} \tag{B.5}$$

$$= K_r\omega^{\alpha} \tag{B.6}$$

where K_r is a real constant.

The initial response function $k(\omega)$ is thus

$$k(\omega) = (K_r + iK_i)\omega^\alpha = Ke^{i\zeta}\omega^\alpha \tag{B.7}$$

Let us now evaluate the ratio K_i/K_r, or equivalently the argument $\zeta = \arctan(K_i/K_r)$. We will use that $k(t)$ is a real function in time space. The inverse Fourier transform of $k(\omega)$ reads

$$k(t) = \frac{1}{2\pi}\int_{-\infty}^{+\infty} e^{i\omega t}Ke^{i\zeta}\omega^\alpha \mathrm{d}\omega \tag{B.8}$$

and its conjugated complex

$$\overline{k(t)} = \frac{1}{2\pi}\int_{-\infty}^{+\infty} e^{-i\omega t}Ke^{-i\zeta}\omega^\alpha \mathrm{d}\omega \tag{B.9}$$

$$= \frac{1}{2\pi}\int_{-\infty}^{+\infty} e^{i\omega t}Ke^{-i\zeta}(-\omega)^\alpha \mathrm{d}\omega \tag{B.10}$$

$k(t)$ being real translates into $k(t) = \overline{k(t)}$, hence

$$e^{i\zeta} = e^{-i\zeta}(-1)^\alpha \tag{B.11}$$

$$\zeta = \frac{\pi}{2}\alpha \tag{B.12}$$

We report this value in equation B.7 to get

$$k(\omega) = K\,(i\omega)^\alpha \tag{B.13}$$

We have thus demonstrated that if $k(\omega)$ has an imaginary part presenting a power law dependence in frequency described by equation B.3, then it can be written in the form of equation B.13. The two real coefficient of this equation are fixed by the initial law for $\mathrm{Im}[k(\omega)]$: the exponent α is unchanged, and the prefactor is given by $K = K_i/\sin(\alpha\pi/2)$.

B.2 Kramers-Kronig algorithm

function KK.m

```
function G=KK(sp,fs,T)

% G=KK(sp,fs,T)
%
% This program computes a response function starting from the noise power
% spectrum density, using Fluctuation-Dissipation Theorem (FDT) and Kramers
% Kronig (KK) relations.
%
% Input variables are :
%   sp : power spectrum density (units U^2/Hz)
%   fs : sampling frequency (Hz)
%   T  : temperature (K) (if omitted, the default value is 295K)
%
% Ouput variable is G : response function, (units U/q, where q is the unit
% of the conjugate variable of U)
%
% FDT reads : sp=4 kB T Im(G) / omega
% where kB is the Boltzmann constant and omega = 2 pi f is the pulsation
% corresponding to frequency f. The knowlegde of Sp thus leads to Im(G),
% and KK relations lead to Re(G).

if (nargin<3)
    kT=1.38e-23*295;
else
    kT=1.38e-23*T;
end

% number of point of input spectrum
npt=length(sp);

% round number of point to nearest power of 2
npt=2^floor(log2(npt));

% define frequency vector
f=(0:npt)/(npt)*fs/2;

% compute Im(G) from FDT
imG=sp/4/kT*2*pi.*f;

% define Im(G) for negative frequencies for FT
imG=[imG(1:npt+1) -imG(npt:-1:2)];

% compute inverse FT of Im(G) (Im(G) is an odd function, its FT is supposed
% to be purely imaginary, thus we take only the imaginary part of the result)
imG_t=imag(ifft(imG));

% we compute the direct FT of sign_t*imG_t (FT of an even function is
% supposed to be purely real, so we keep ony the real part)
sign_t=[0 ones(1,npt) -ones(1,npt-1)];
reG=real(fft(sign_t.*imG_t));

% limit the result to positive frequencies
G=reG(1:npt+1)+1i*imG(1:npt+1);

return
```

Appendix C

Adsorbed Elastica

C.1 Balance between adhesion and adsorption

Let us prove the validity of equation 4.17 step by step:

$$E_a = \frac{\partial E_c}{\partial L} \tag{C.1}$$

$$= \frac{1}{2} EI \frac{\partial}{\partial L} \int_0^L \left(\frac{\partial \theta(s,L)}{\partial s} \right)^2 \mathrm{d}s \tag{C.2}$$

$$= \frac{1}{2} EI {\theta'_L}^2 + \frac{1}{2} EI \int_0^L \frac{\partial}{\partial L} \left(\frac{\partial \theta(s,L)}{\partial s} \right)^2 \mathrm{d}s \tag{C.3}$$

$$= \frac{1}{2} EI {\theta'_L}^2 + EI \int_0^L \frac{\partial^2 \theta(s,L)}{\partial L \partial s} \frac{\partial \theta(s,L)}{\partial s} \mathrm{d}s \tag{C.4}$$

$$= \frac{1}{2} EI {\theta'_L}^2 + EI \left[\frac{\partial \theta(s,L)}{\partial L} \frac{\partial \theta(s,L)}{\partial s} \right]_0^L - EI \int_0^L \frac{\partial \theta(s,L)}{\partial L} \frac{\partial^2 \theta(s,L)}{\partial s^2} \mathrm{d}s \tag{C.5}$$

Let us compute the boundary term first. In $s = 0$, the standard boundary conditions ($\theta(0, L)$ constant or $\theta'(0, L) = 0$) cancel this boundary term. In $s = L$ however, the boundary condition is sliding with L: $\theta(s = L, L) = \pi/2$.

We can therefore write:

$$\frac{\mathrm{d}\theta(L,L)}{\mathrm{d}L} = 0 = \left.\frac{\partial\theta}{\partial s}\right|_L (L,L) + \left.\frac{\partial\theta}{\partial L}\right|_s (L,L) \tag{C.6}$$

$$\left.\frac{\partial\theta}{\partial L}\right|_s (L,L) = -\left.\frac{\partial\theta}{\partial s}\right|_L (L,L) = -\theta'_L \tag{C.7}$$

The boundary term is thus $-EI{\theta'_L}^2$. Then, using the Elastica, we can rewrite equation C.5 as:

$$E_a = -\frac{1}{2}EI{\theta'_L}^2 + \int_0^L \frac{\partial\theta(s,L)}{\partial L} F\sin\theta(s,L)\mathrm{d}s \tag{C.8}$$

$$= -\frac{1}{2}EI{\theta'_L}^2 - F\int_0^L \frac{\partial}{\partial L}\cos\theta(s,L)\mathrm{d}s \tag{C.9}$$

$$= -\frac{1}{2}EI{\theta'_L}^2 - F\left(\frac{\partial}{\partial L}\int_0^L \cos\theta(s,L)\mathrm{d}s - \cos\theta_L\right) \tag{C.10}$$

$$= -\frac{1}{2}EI{\theta'_L}^2 - F\left(\frac{\partial Z}{\partial L} - \cos\theta_L\right) \tag{C.11}$$

Z is fixed in the minimization of E_{CNT}, and $\theta_L = \pi/2$ for the adsorbed nanotube, thus the second term of this equation is 0 and the validity of equation 4.17 verified.

C.2 Numerical integration of the Elastica

The following Matlab code can be use to integrate numerically the Elastica in the case of a torque free origin and an adsorbed end. It consists of two different files :

- `flambage.m`: function to compute the shape and curvature energy for given pulling force and boundary conditions

- `elastica.m`: script to compute the shape, total energy, force and dynamic stiffness of an adsorbed Elastica for a set of origin/substrate distances. Figure C.1 corresponds to the output of this script.

C.2.1 function `flambage.m`

```
function [X,Z,Ec,sol]=flambage(F,theta0,thetaL,solinit)

% [X,Z,Ec,sol]=flambage(F,theta0,thetaL,solinit)
%
% Recherche la forme d'équilibre d'une tige de longueur 1 subissant une
% force F selon l'axe vertical. La raideur en torsion de la tige
% est unitaire : EI=1. theta0 et thetaL précisent les conditions aux
% limites à l'origine et au point final de la tige. S'ils sont définis, ils
% fixent l'angle avec la verticale, sinon la condition imposée est celle
% d'un couple nul. solinit est le paramètre de départ de l'optimisation
% (optionel).
%
% X et Z sont les coordonnées du point final. Ec est l'énergie de courbure
% de la tige, et sol contient la (ou les) fonction(s) optimisée(s).
%
% Remarque : Ec prend la valeur NaN si la valeur maximale de z est
% supérieure à Z (impossible pour une compression de la tige par un plan).

% En l'absence de solution initiale, on prend une fonction linéaire de
% l'abscisse curviligne
if (nargin<4||isempty(solinit))
    if isempty(theta0)
        solinit = bvpinit(linspace(0,1),[thetaL 0]);
    else
        solinit = bvpinit(linspace(0,1),[theta0 0]);
    end
end

% Initialisation des variables de sortie
X=zeros(size(F));
Z=zeros(size(F));
Ec=zeros(size(F));

for idx=1:length(F)
    % résolution de l'ODE compte tenu des conditions aux bords
    sol(idx)=bvp4c(@(s,T) twoode(s,T,F(idx)),...
        @(T_0,T_L) twobc(T_0,T_L,theta0,thetaL),...
                   solinit);

    % calcul de la forme de la tige courbée paramétrée par l'abscisse
    % curviligne s.
    ds=1e-3;
    s= 0:ds:1;
    T = deval(sol(idx),s);
    x=cumsum(sin(T(1,:)))*ds;
    z=cumsum(cos(T(1,:)))*ds;

    % variables de sortie
    X(idx)=x(end);
    Z(idx)=z(end);
    Ec(idx)=sum(T(2,:).^2)*ds/2;
    if max(z)>Z(idx)
        Ec(idx)=NaN;
    end

    % On conserve la solution actuelle pour la prochaine résolution
    % (convergence accélérée si la force F change peu)
    solinit=sol(idx);
```

```
end

% fonction à usage interne : définition de l'ODE du premier ordre
% équivalente à theta"=-F sin(theta) à l'aide de T=[theta theta']
function dTds = twoode(~,T,F)
dTds = [ T(2)
         -F*sin(T(1))];

% fonction à usage interne : définition des conditions aux bords
function res = twobc(T_0,T_L,theta0,thetaL)
if isempty(theta0)
    % moment nul à l'origine : theta_0'=T_0(2)=0
    idx0=2;
    theta0=0;
else
    % angle fixé à l'origine : theta_0=T_0(1)=theta0
    idx0=1;
end
if isempty(thetaL)
    % moment nul l'extrémité  : theta_L'=T_L(2)=0
    idxL=2;
    thetaL=0;
else
    % angle fixé à l'extrémité : theta_L=T_L(1)=thetaL
    idxL=1;
end

res = [ T_0(idx0)-theta0
        T_L(idxL)-thetaL];
```

C.2.2 script `elastica.m`

```
%% Forme d'équilibre d'une tige tractée - adsorbée

% On simule le décollage d'une tige d'une surface sur laquelle elle est
% adsorbée, en cherchant la relation entre la force appliquée, la longueur
% décollée de la tige, et la distance entre le point de traction et le plan
% d'adsorption.

% La raideur en torsion de la tige est unitaire, tout comme sa longeur :
EI=1;
L0=1;

% Rayon de courbure naturel au point de contact avec la surface
Ra=0.2*L0;

% Énergie d'adhésion de la tige
Ea=EI/2/Ra^2;

%% Solution générique tige appuyée encastrée

% On calcule un ensemble de courbes de flambage d'une tige unitaire
% subissant une force F verticale et un moment nul à l'origine, et
% formant un angle pi/2 à son autre extrémité.

% Plage d'exploration en force
F=-(0:0.003:1).^2*2*Ea;
[X,Z,Ec,sol]=flambage(F,[],pi/2);
```

```
%% Forme d'équilibre d'une tige tractée - adsorbée

% On simule le décollage d'une tige d'une surface sur laquelle elle est
% adsorbée, en cherchant la relation entre la force appliquée, la longueur
% décollée de la tige, et la distance entre le point de traction et le plan
% d'adsorption.

figure

% distance entre le point de traction et le plan d'adsorption
H=(0.005:0.005:0.995)*L0;

% abscisse curviligne
ds=1e-3;
s=0:ds:1;

% variable de couleur pour le tracé des courbes
couleur=jet(100);

% Initialisation des variables :
E=zeros(size(H));           % énergie totale de la tige
L=zeros(size(H));           % longueur de tige adsorbée
Fz=zeros(size(H));          % force verticale
kdyn=zeros(size(H));        % raideur dynamique
deltakdyn=zeros(size(H));   % erreur sur l'estimation de la raideur

for idx=1:length(H)
    % On laisse la longueur de la tige comme paramètre libre (mais
    % inférieur à L0) et on cherche le minimum d'énergie entre la courbure
    % de cette tige et l'adsorption de la partie restante sur la surface
    [E(idx) idx2]=min(Ec.*Z/H(idx)+Ea*(H(idx)./Z-L0));
    % Pour éviter les effets de quantisation dus aux nombre limité de
    % valeur de F, on cherche à réaliser un fit parabolique autour de ce
    % minimum en utilisant une dizaine de point
    idxfit=max(1,idx2-5):min(length(F),idx2+5);
    if (length(idxfit)>2)
        P=polyfit(F(idxfit),...
                  Ec(idxfit).*Z(idxfit)/H(idx)+Ea*(H(idx)./Z(idxfit)-L0),2);
        Ftmp=-P(2)/2/P(1);
    else
        Ftmp=F(idx2);
    end
    % On résoud à nouveau l'ODE en prenant la valeur adéquate de F, ainsi
    % que de petite variations autour pour estimer la raideur dynamique
    [Xtmp,Ztmp,Ectmp,soltmp]=flambage(Ftmp*[0.99 1 1.01],[],pi/2,sol(idx2));

    % longeur de tige adsorbée
    L(idx)=H(idx)./Ztmp(2);
    % Si la solution existe
    if (L(idx)<L0)
        % Énergie totale de la tige
        E(idx)=Ectmp(2)/L(idx)+Ea*(L(idx)-L0);
        % Force de traction
        Fz(idx)=Ftmp/L(idx)^2;
        % raideur dynamique
        kdyn(idx)=...
            -0.01*Ftmp*(1/(Ztmp(2)-Ztmp(1))+1/(Ztmp(3)-Ztmp(2)))/2/L(idx)^3;
        deltakdyn(idx)=...
            0.01*Ftmp*(1/(Ztmp(2)-Ztmp(1))-1/(Ztmp(3)-Ztmp(2)))/2/L(idx)^3;
        % solution de l'ODE
```

```
        soladh(idx)=soltmp(2);
        ttp = deval(soladh(idx),s);
        x=cumsum(sin(ttp(1,:)))*ds*L(idx);
        z=cumsum(cos(ttp(1,:)))*ds*L(idx);
        % tracé de la solution (1 courbe sur 10)
        if (~mod(idx-1,10))
            plot(x/Ra,z/Ra,'color',couleur(ceil(z(end)*100),:))
            hold on
            plot((x(end)+[0 1-L(idx)])/Ra,[z(end) H(idx)]/Ra,...
                '+-','color',couleur(ceil(z(end)*100),:))
        end
    else
        Fz(idx)=NaN;
        E(idx)=NaN;
        L(idx)=NaN;
        kdyn(idx)=NaN;
    end
    pause(0.01)
end
axis([-0.1 5.1 -0.1 5.1])
axis square
set(gca,'ydir','reverse')
xlabel('x/Ra')
ylabel('z/Ra')
grid

%% Énergie, force et raideur vs distance

figure

subplot(3,1,1)
plot(H/Ra,E/Ea)
xlabel('H/Ra')
ylabel('E/Ea')
grid

subplot(3,1,2)
plot(H/Ra,Fz/Ea)
xlabel('H/Ra')
ylabel('F/Ea')
axis([0 5 -6 0])
grid

subplot(3,1,3)
plot(H/Ra,kdyn/(Ea/Ra))
xlabel('H/Ra')
ylabel('kdyn/(Ea/Ra)')
axis([0 5 0 10])
grid
```

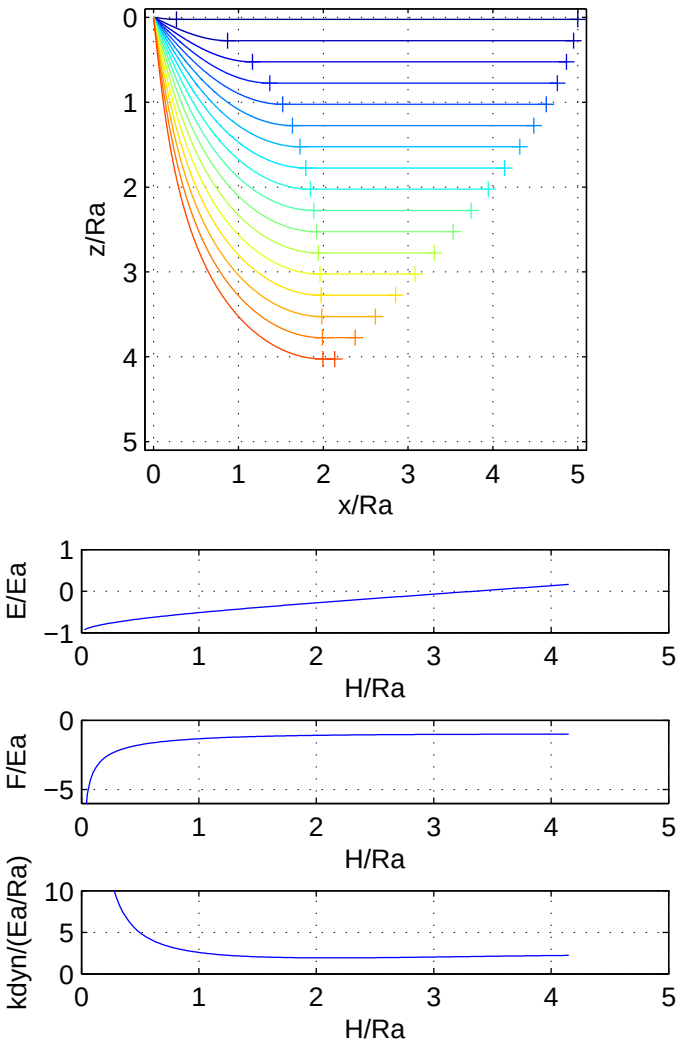

Figure C.1 – *Output of script* `elastica.m`*: shape of adsorbed Elastica for various origin/substrate distances, and total energy, force and dynamic stiffness versus distance.*

Appendix D

Datasheets of cantilevers and calibration samples

D.1 *Budget Sensors* Cont-GB cantilever

Budget Sensors

AFM probe Model: ContGB-G

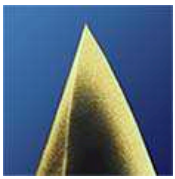

This probe has alignment grooves on the backside of the holder chip.

- Contact Mode and Special Applications
- Rotated Monolithic Silicon Probe
  Symmetric Tip Shape
  Chipsize: 3.4 x 1.6 x 0.3 mm
- Coating: Overall gold coating with a nominal thickness of 70nm on both sides of the cantilever. This coating also enhances the laser reflectivity of the cantilever.
- This probe uses an “on scan angle” symmetric tip to provide a more ymmetric representation of features over 200 nm.

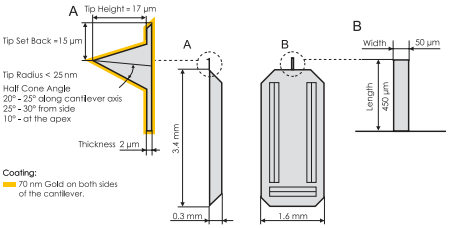

	Typical Values	Range
Resonant Frequency	13 kHz	+/- 4 kHz
Force Constant	0.2 N/m	0.07 - 0.4 N/m
Cantilever Length	450 µm	+/- 10 µm
Mean Width	50 µm	+/- 5 µm
Thickness	2 µm	+/- 1 µm
Tip Height	17 µm	+/- 2 µm
Tip Set Back	15 µm	+/- 5 µm
Tip Radius	< 25 nm	
Coating	Overall Gold Coating	
Half Cone Angle	20° - 25° along cantilever axis 25° - 30° from side 10° at the apex	

D.2 *Budget Sensors* Cont cantilever

Budget Sensors

AFM probe Model: Contact

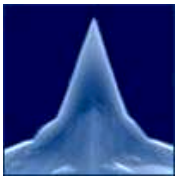

- Contact Mode
- Rotated Monolithic Silicon Probe
  Symmetric Tip Shape
  Chipsize: 3.4 x 1.6 x 0.3 mm
- Coating: none
- This probe uses an “on scan angle” symmetric tip to provide a more symmetric representation of features over 200 nm.

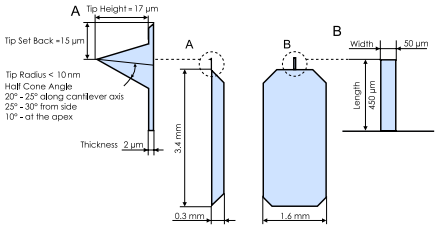

	Typical Values	Range
Resonant Frequency	13 kHz	+/- 4 kHz
Force Constant	0.2 N/m	0.07 - 0.4 N/m
Cantilever Length	450 µm	+/- 10 µm
Mean Width	50 µm	+/- 5 µm
Thickness	2 µm	+/- 1 µm
Tip Height	17 µm	+/- 2 µm
Tip Set Back	15 µm	+/- 5 µm
Tip Radius	< 10 nm	
Coating	none	
Half Cone Angle	20º - 25º along cantilever axis 25º - 30º from side 10º at the apex	

D.3 *NanoWorld* Arrow TL cantilever

Arrow™ Silicon-SPM-Probes General Description

NANO WORLD
INNOVATIVE TECHNOLOGIES

General

- SPM probe for very high resolution imaging
- fits to all well-known commercial SPMs
- cantilever and tip are supported by a single crystal silicon holder
- monolithic design of holder, cantilever and tip
- tip is pointing into the <100> direction

Material Features

- highly doped, single crystal silicon
- high conductivity of the doped silicon prevents electrostatic charging
- resistivity is as low as 0.01-0.025 Ohm*cm.
- no intrinsic stress and absolutely straight cantilevers
- no bending of cantilever by changing temperatures
- chemically inert silicon for application in fluids or electrochemical cells

Cantilever

- rectangular cantilever that is shaped like an arrow
- trapezoidal cross section of the cantilever
- wide detector side for easy adjustment of the detection system
- small width at the tip side reduces damping

Datasheet Arrow™ TL8

NANO WORLD
INNOVATIVE TECHNOLOGIES

Special Application Cantilevers

NanoWorld Arrow™ TL8 sensors are tipless cantilevers for special applications. They can for example be used for attaching spheres and other objects to the free end of the cantilever, or for functionalizing and sensing applications.

All sensors of the Arrow™ series are made from monolithic silicon which is highly doped to dissipate static charge and are chemically inert. The TL8 sensors feature eight rectangular cantilevers having a triangular free end.
The cantilevers have a pitch of 250 µm.

The Arrow™ TL8 sensors are optionally available with a top side coating of 5nm titanium / 30nm gold. (Arrow™ TL8Au)

Cantilever Data	Value	Range*
Thickness	**1.0 µm**	0.5 - 2.5
Width (rectangular part)	**100 µm**	95 - 105
Length	**500 µm**	495 - 505
Force Constant	**0.03 N/m**	0.004 - 0.54
Pitch	**250 µm**	n.a.
Resonance Frequency	**6 kHz**	3 - 14

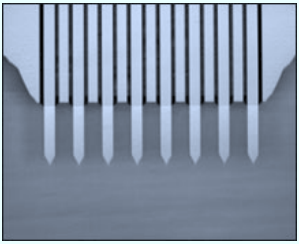

D.4 *Budget Sensors* HS-20MG calibration sample

BudgetSensors

Product Model: HS-20MG

Why do you need the HS-20MG?

Atomic Force Microscopy has become a valuable tool not only for visualization but also for performing accurate measurements on the nanometer and micrometer scale.

In order to make the most of their measurement capabilities, AFM systems need to be properly calibrated.

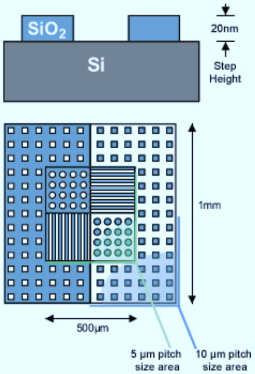

Our Solution

HS-20MG is one of the height standards introduced by BudgetSensors as a response to the increased demand for affordable high-quality AFM calibration standards.

The HS-20MG features Silicon Dioxide structure arrays on a 5x5mm Silicon chip. The fabrication process guarantees excellent uniformity of the structures across the chip. This in turn ensures easy and reliable Z-axis calibration of your AFM system.

The calibration area is situated in the center of the chip. It is easy to find with the AFM optical system. The structure step height is in the range of 20nm. The exact value for each chip is indicated on the box label. Arrays of structures with different shape and pitch are integrated on the chip. The larger square (1x1mm) contains square pillars and holes with a 10µm pitch. The smaller square (500x500µm) contains circular pillars and holes as well as lines in the X- and Y-direction with a 5µm pitch.

Aside from Z-axis calibration, this design also allows X- and Y-axis calibration for bigger scanners (40-100µm range). What is more, the structure symmetry makes it possible to calibrate your AFM system without the need to rotate and realign the sample in-between X- and Y-axis calibration.

The HS-20MG chip is glued onto a 12mm metal disc using a high-quality electrically-conductive epoxy resin and it is ready for use as shipped.

Technical data at a glance:

Die size:
5x5mm

Step height:
~20nm, the precise value is stated on the label of each box

Structure geometry:
- square holes and pillars with a 10µm pitch arranged in a 1x1mm square
- circular pillars and holes, and lines in the x- and y-direction with a 5µm pitch arranged in a 500x500µm square

Bibliography

[1] D. Anselmetti, Ch. Gerber, B. Michel, H.-J. Guntherodt, and H. Rohrer. Compact, combined scanning tunneling/force microscope, *Rev. Sci. Instrum.* **63**, 3003–3006 (1992).

[2] S. Bal and S. S. Samal. Carbon nanotube reinforced polymer composites - a state of the art, *Bull. Mater. Sci.* **30**, 379–386 (2007).

[3] A.D.S. Barr. Torsional waves in uniform rods of non-circular section, *Journal of Mechanical Engineering Science* **4**, 127–135 (1962).

[4] Sudipta Basak, Arvind Raman, and Suresh V. Garimella. Hydrodynamic loading of microcantilevers vibrating in viscous fluids, *Journal of Applied Physics* **99**, 114906 (2006).

[5] Ray H. Baughman, Anvar A. Zakhidov, and Walt A. de Heer. Carbon nanotubes–the route toward applications, *Science* **297**, 787–792 (2002).

[6] L. Bellon. Thermal noise of microcantilevers in viscous fluids, *Journal of Applied Physics* **104**, 104906 (2008).

[7] L. Bellon and S. Ciliberto. Experimental study of the fluctuation dissipation relation during an aging process, *Physica D-Nonlinear Phenomena* **168**, 325–335 (2002).

[8] L. Bellon, S. Ciliberto, and C. Laroche. Memory in the aging of a polymer glass, *Europhysics Letters* **51**, 551–556 (2000).

[9] L. Bellon, S. Ciliberto, and C. Laroche. Violation of the fluctuation-dissipation relation during the formation of a colloidal glass, *Europhysics Letters* **53**, 511–517 (2001).

[10] L. Bellon, L. Buisson, S. Ciliberto, and F. Vittoz. Zero applied stress rheometer, *Review of Scientific Instruments* **73**, 3286–3290 (2002).

[11] L. Bellon, S. Ciliberto, H. Boubaker, and L. Guyon. Differential interferometry with a complex contrast, *Optics Communications* **207**, 49–56 (2002).

[12] L. Bellon, S. Ciliberto, and C. Laroche. Advanced memory effects in the aging of a polymer glass, *European Physical Journal B* **25**, 223–231 (2002).

[13] L. Bellon, M. Gibert, and R. Hernandez. Coupling between aging and convective motion in a colloidal glass of laponite, *European Physical Journal B* **55**, 101–107 (2007).

[14] Ludovic Bellon. *Vieillissement des systèmes vitreux et rapport fluctuation-dissipation.* PhD thesis, École Normale Supérieure de Lyon, 04 2001. – `http://tel.archives-ouvertes.fr/tel-00003649/`.

[15] Lorin X. Benedict, Nasreen G. Chopra, Marvin L. Cohen, A. Zettl, Steven G. Louie, and Vincent H. Crespi. Microscopic determination of the interlayer binding energy in graphite, *Chemical Physics Letters* **286**, 490 – 496 (1998).

[16] B. Bhushan. *Handbook of Nanotechnology.* Springer-Verlag, Heidelberg, 2004.

[17] Bharat Bhushan. Nanotribology, nanomechanics and nanomaterials characterization, *Philosophical Transactions of the Royal Society A: Mathematical, Physical and Engineering Sciences* **366**, 1351–1381 (2008).

[18] K Binder. Phase transitions in reduced geometry, *Annual Review of Physical Chemistry* **43**, 33–59 (1992).

[19] G. Binnig, C. F. Quate, and Ch. Gerber. Atomic force microscope, *Phys. Rev. Lett.* **56**, 930–933 (1986).

[20] L. Bocquet, E. Charlaix, S. Ciliberto, and J. Crassous. Moisture-induced ageing in granular media and the kinetics of capillary condensation, *Nature* **396**, 735–737 (1998).

[21] Daniel Bonn, Jens Eggers, Joseph Indekeu, Jacques Meunier, and Etienne Rolley. Wetting and spreading, *Rev. Mod. Phys.* **81**, 739–805 (2009).

[22] O. Breuer and Uttandaraman Sundararaj. Big returns from small fibers: A review of polymer/carbon nanotube composites, *Polymer Composites* **25**, 630–645 (2004).

[23] Julien Buchoux, Jean-Pierre Aimé, Rodolphe Boisgard, Cattien V. Nguyen, Lionel Buchaillot, and Sophie Marsaudon. Investigation of the carbon nanotube afm tip contacts: free sliding versus pinned contact, *Nanotechnology* **20**, 475701 (2009).

[24] L. Buisson, L. Bellon, and S. Ciliberto. Intermittency in ageing, *Journal of Physics: Condensed Matter* **15**, S1163–S1179 (2003).

[25] N A Burnham, X Chen, C S Hodges, G A Matei, E J Thoreson, C J Roberts, M C Davies, and S J B Tendler. Comparison of calibration methods for atomic-force microscopy cantilevers, *Nanotechnology* **14**, 1–6 (2003).

[26] H J Butt and M Jaschke. Calculation of thermal noise in atomic force microscopy, *Nanotechnology* **6**, 1 (1995).

[27] Hans-Jurgen Butt, Brunero Cappella, and Michael Kappl. Force measurements with the atomic force microscope: Technique, interpretation and applications, *Surface Science Reports* **59**, 1–152 (2005).

[28] Herbert B. Callen and Richard F. Greene. On a theorem of irreversible thermodynamics, *Phys. Rev.* **86**, 702–710 (1952).

[29] Mariano Carrion Vazquez, Andres F. Oberhauser, Susan B. Fowler, Piotr E. Marszalek, Sheldon E. Broedel, Jane Clarke, and Julio M. Fernandez. Mechanical and chemical unfolding of a single protein: A comparison, *Proceedings of the National Academy of Sciences of the United States of America* **96**, 3694–3699 (1999).

[30] Elisabeth Charlaix and Jérôme Crassous. Adhesion forces between wetted solid surfaces, *The Journal of Chemical Physics* **122**, 184701 (2005).

[31] B Chen, M Gao, JM Zuo, S Qu, B Liu, and Y Huang. Binding energy of parallel carbon nanotubes, *Applied Physics Letters* **83**, 3570–3571 (2003).

[32] James W. M. Chon, Paul Mulvaney, and John E. Sader. Experimental validation of theoretical models for the frequency response of atomic force microscope cantilever beams immersed in fluids, *Journal of Applied Physics* **87**, 3978–3988 (2000).

[33] Nasreen G. Chopra, Lorin X. Benedict, Vincent H. Crespi, Marvin L. Cohen, Steven G. Louie, and A. Zettl. Fully collapsed carbon nanotubes, *Nature* **377**, 135–138 (1995).

[34] D R M Crooks, P Sneddon, G Cagnoli, J Hough, S Rowan, M M Fejer, E Gustafson, R Route, N Nakagawa, D Coyne, G M Harry, and A M Gretarsson. Excess mechanical loss associated with dielectric mirror coatings on test masses in interferometric gravitational wave detectors, *Classical and Quantum Gravity* **19**, 883–896 (2002).

[35] Leticia F. Cugliandolo, Jorge Kurchan, and Luca Peliti. Energy flow, partial equilibration, and effective temperatures in systems with slow dynamics, *Phys. Rev. E* **55**, 3898–3914 (1997).

[36] John Cumings and A. Zettl. Low-Friction Nanoscale Linear Bearing Realized from Multiwall Carbon Nanotubes, *Science* **289**, 602–604 (2000).

[37] M. J. Cunningham, S. T. Cheng, and W. W. Clegg. A differential interferometer for scanning force microscopy, *Measurement Science and Technology* **5**, 1350 (1994).

[38] P. G. Datskos, N. V. Lavrik, and S. Rajic. Performance of uncooled microcantilever thermal detectors, *Review of Scientific Instruments* **75**, 1134–1148 (2004).

[39] S.R. de Groot and P.. Mazur. *Non-equilibrium thermodynamics*. Dover, 1984.

[40] B. de Saint-Venant. Mémoire sur les vibrations tournantes des verges élastiques, *Comptes Rendus* **28**, 69 (1849).

[41] A. Débarre, M. Kobylko, A. M. Bonnot, A. Richard, V. N. Popov, L. Henrard, and M. Kociak. Electronic and mechanical coupling of carbon nanotubes: A tunable resonant raman study of systems with known structures, *Phys. Rev. Lett.* **101**, 197403 (2008).

[42] A. J. den Boef. Scanning force microscopy using a simple low-noise interferometer, *Appl. Phys. Lett.* **55**, 439–441 (1989).

[43] A. J. den Boef. The influence of lateral forces in scanning force microscopy, *Review of Scientific Instruments* **62**, 88–92 (1991).

[44] J.H. Dieterich and G. Conrad. Effect of humidity on time- and velocity-dependent friction in rocks, *J. Geophys. Res.* **89**, 4196–4202 (1984).

[45] Zoran Djuric. Mechanisms of noise sources in microelectromechanical systems, *Microelectronics Reliability* **40**, 919 – 932 (2000).

[46] Jerome Dorignac, Agnieszka Kalinowski, Shyamsunder Erramilli, and Pritiraj Mohanty. Dynamical response of nanomechanical oscillators in immiscible viscous fluid for in vitro biomolecular recognition, *Physical Review Letters* **96**, 186105 (2006).

[47] J. Duran. *Sables, Poudres et Grains*. Eyrolles Sciences, Paris, 1997.

[48] M. D. Ediger, C. A. Angell, and Sidney R. Nagel. Supercooled liquids and glasses, *The Journal of Physical Chemistry* **100**, 13200–13212 (1996).

[49] V. S. Ekel'Chik. Torsional vibrations and dispersion of torsional waves in orthotropic composite rods, *Mechanics of Composite Materials* **44**, 109–120 (2008).

[50] Franz-Josef Elmer and Markus Dreier. Eigenfrequencies of a rectangular atomic force microscope cantilever in a medium, *Journal of Applied Physics* **81**, 7709–7714 (1997).

[51] Marie Faith Fiawoo. *Étude par microscopie électronique en transmission de la germination et de la croissance des nanotubes de carbone synthétisés à moyenne température*. PhD thesis, University Pierre et Marie Curie/Onera, July 2009.

[52] Thomas E Fisher, Piotr E Marszalek, Andres F Oberhauser, Mariano Carrion-Vazquez, and Julio M Fernandez. The micro-mechanics of single molecules studied with atomic force microscopy, *The Journal of Physiology* **520**, 5–14 (1999).

[53] Patrick L.T.M. Frederix, Patrick D. Bosshart, and Andreas Engel. Atomic force microscopy of biological membranes, *Biophysical journal* **96**, 329–338 (2009).

[54] Takeshi Fukuma. Wideband low-noise optical beam deflection sensor with photothermal excitation for liquid-environment atomic force microscopy, *Review of Scientific Instruments* **80**, 023707 (2009).

[55] Murali Krishna Ghatkesar, Thomas Braun, Viola Barwich, Jean-Pierre Ramseyer, Christoph Gerber, Martin Hegner, and Hans Peter Lang. Resonating modes of vibrating microcantilevers in liquid, *Applied Physics Letters* **92**, 043106 (2008).

[56] L. A. Girifalco and R. A. Lad. Energy of cohesion, compressibility, and the potential energy functions of the graphite system, *The Journal of Chemical Physics* **25**, 693–697 (1956).

[57] L. A. Girifalco, Miroslav Hodak, and Roland S. Lee. Carbon nanotubes, buckyballs, ropes, and a universal graphitic potential, *Phys. Rev. B* **62**, 13104–13110 (2000).

[58] Gabriela I. González and Peter R. Saulson. Brownian motion of a torsion pendulum with internal friction, *Physics Letters A* **201**, 12 – 18 (1995).

[59] Kazuya Goto, Minoru Sasaki, Shigeru Okuma, and Kazuhiro Hane. A double-focus lens interferometer for scanning force microscopy, *Review of Scientific Instruments* **66**, 3182–3185 (1995).

[60] Christopher P. Green and John E. Sader. Torsional frequency response of cantilever beams immersed in viscous fluids with applications to the atomic force microscope, *Journal of Applied Physics* **92**, 6262–6274 (2002).

[61] Christopher P. Green and John E. Sader. Frequency response of cantilever beams immersed in viscous fluids near a solid surface with applications to the atomic force microscope, *Journal of Applied Physics* **98**, 114913 (2005).

[62] M. G. L. Gustafsson and J. Clarke. Scanning force microscope springs optimized for optical-beam deflection and with tips made by controlled fracture,, *J. Appl. Phys.* **76**, 172–181 (1994).

[63] Tobias Hertel, Richard Martel, and Phaedon Avouris. Manipulation of individual carbon nanotubes and their interaction with surfaces, *The Journal of Physical Chemistry B* **102**, 910–915 (1998).

[64] Tobias Hertel, Robert E. Walkup, and Phaedon Avouris. Deformation of carbon nanotubes by surface van der waals forces, *Phys. Rev. B* **58**, 13870–13873 (1998).

[65] B. W. Hoogenboom, P. L. T. M. Frederix, J. L. Yang, S. Martin, Y. Pellmont, M. Steinacher, S. Zäch, E. Langenbach, H.-J. Heimbeck, A. Engel, and H. J. Hug. A fabry–perot interferometer for micrometer-sized cantilevers, *Applied Physics Letters* **86**, 074101 (2005).

[66] B W Hoogenboom, P L T M Frederix, D Fotiadis, H J Hug, and A Engel. Potential of interferometric cantilever detection and its application for sfm/afm in liquids, *Nanotechnology* **19**, 384019 (2008).

[67] D.R. Hornbaker, I. Albert, A.L. Barabasi, and P. Shiffer. What keeps sandcastles standing?, *Nature* **387**, 765–766 (1997).

[68] Farzana Hussain, Mehdi Hojjati, Masami Okamoto, and Russell E. Gorga. Review article: Polymer-matrix Nanocomposites, Processing, Manufacturing, and Application: An Overview, *Journal of Composite Materials* **40**, 1511–1575 (2006).

[69] Jeffrey L. Hutter and John Bechhoefer. Calibration of atomic-force microscope tips, *Review of Scientific Instruments* **64**, 1868–1873 (1993).

[70] Makoto Ishikawa, Ryuichi Harada, Naruo Sasaki, and Kouji Miura. Visualization of nanoscale peeling of carbon nanotube on graphite, *Applied Physics Letters* **93**, 083122 (2008).

[71] Makoto Ishikawa, Ryuichi Harada, Naruo Sasaki, and Kouji Miura. Adhesion and peeling forces of carbon nanotubes on a substrate, *Phys. Rev. B* **80**, 193406 (2009).

[72] J. Israelachvili. *Intermolecular and Surface Forces.* Academic Press, London, 1992.

[73] K. Jonason, E. Vincent, J. Hammann, J. P. Bouchaud, and P. Nordblad. Memory and chaos effects in spin glasses, *Phys. Rev. Lett.* **81**, 3243–3246 (1998).

[74] A. K. Jonscher. The 'universal' dielectric response, *Nature* **267**, 673–679 (1977).

[75] G. Jourdan, A. Lambrecht, F. Comin, and J. Chevrier. Quantitative non-contact dynamic casimir force measurements, *EPL (Europhysics Letters)* **85**, 31001 (2009).

[76] Mariko Kajima, Nobuhiro Kusumi, Shigenori Moriwaki, and Norikatsu Mio. Wide-band measurement of mechanical thermal noise using a laser interferometer, *Physics Letters A* **263**, 21 – 26 (1999).

[77] Changhong Ke, Meng Zheng, Guangwen Zhou, Weili Cui, Nicola Pugno, and Ronald N. Miles. Mechanical peeling of free-standing single-walled carbon-nanotube bundles, *Small* **6**, 438–445 (2010).

[78] A. L. Kimball and D. E. Lovell. Internal friction in solids, *Phys. Rev.* **30**, 948–959 (1927).

[79] A. Kis, G. Csanyi, J. P. Salvetat, Thien-Nga Lee, E. Couteau, A. J. Kulik, W. Benoit, J. Brugger, and L. Forro. Reinforcement of single-walled carbon nanotube bundles by intertube bridging, *Nat Mater* **3**, 153–157 (2004).

[80] A. Kis, K. Jensen, S. Aloni, W. Mickelson, and A. Zettl. Interlayer forces and ultralow sliding friction in multiwalled carbon nanotubes, *Physical Review Letters* **97**, 025501 (2006).

[81] Andras Kis and Alex Zettl. Nanomechanics of carbon nanotubes, *Philosophical Transactions of the Royal Society A: Mathematical, Physical and Engineering Sciences* **366**, 1591–1611 (2008).

[82] L. Landau and E. Lifchitz. *Theory of elasticity.* Mir, Moscow, 1967.

[83] Kenneth K. S. Lau, Jose Bico, Kenneth B. K. Teo, Manish Chhowalla, Gehan A. J. Amaratunga, William I. Milne, Gareth H. McKinley, and Karen K. Gleason. Superhydrophobic carbon nanotube forests, *Nano Letters* **3**, 1701–1705 (2003).

[84] Nickolay V. Lavrik, Michael J. Sepaniak, and Panos G. Datskos. Cantilever transducers as a platform for chemical and biological sensors, *Review of Scientific Instruments* **75**, 2229–2253 (2004).

[85] B. Lawn. *The Fracture of Brittle Solids.* Cambridge University Press, Cambridge, 1993.

[86] B. Lefevre, A. Saugey, J. L. Barrat, L. Bocquet, E. Charlaix, P. F. Gobin, and G. Vigier. Intrusion and extrusion of water in hydrophobic

mesopores, *The Journal of Chemical Physics* **120**, 4927–4938 (2004).

[87] Ron Lifshitz and M. L. Roukes. Thermoelastic damping in micro- and nanomechanical systems, *Phys. Rev. B* **61**, 5600–5609 (2000).

[88] F. Lochon, L. Dufour, D. Rebiere, U. Sampath, S.M. Heinrich, and F. Josse. Effect of viscoelasticity on quality factor of microcantilever chemical sensors: optimal coating thickness for minimum limit of detection. In *Sensors, 2005 IEEE*, pages 265–268, 2005.

[89] A.E.H. Love. *Mathematical theory of elasticity.* Cambridge University Press, 4th edition, 1927.

[90] A.E.H. Love. *Mathematical theory of elasticity*, page 325. Cambridge University Press, 4th edition, 1927.

[91] Abdelhamid Maali, Cedric Hurth, Rodolphe Boisgard, Cédric Jai, Touria Cohen-Bouhacina, and Jean-Pierre Aimé. Hydrodynamics of oscillating atomic force microscopy cantilevers in viscous fluids, *Journal of Applied Physics* **97**, 074907 (2005).

[92] Roya Maboudian and Roger T. Howe. Critical review: Adhesion in surface micromechanical structures, *Journal of Vacuum Science & Technology B: Microelectronics and Nanometer Structures* **15**, 1–20 (1997).

[93] H. J. Mamin and D. Rugar. Sub-attonewton force detection at millikelvin temperatures, *Appl. Phys. Lett.* **79**, 3358–3360 (2001).

[94] L. Marty, A. Iaia, M. Faucher, V. Bouchiat, C. Naud, M. Chaumont, T. Fournier, and A.M. Bonnot. Self-assembled single wall carbon nanotube field effect transistors and afm tips prepared by hot filament assisted cvd, *Thin Solid Films* **501**, 299 – 302 (2006).

[95] Constanze Hohberger Metzger and Khaled Karrai. Cavity cooling of a microlever, *Nature* **432**, 1002–1005 (2004).

[96] Ernst Meyer, Hans Josef Hug, and Roland Bennewitz. *Scanning Probe Microscopy: The Lab on a Tip.* Springer, 2004.

[97] Gerhard Meyer and Amer Nabil M. Novel optical approach to atomic force microscopy, *Appl. Phys. Lett.* **53**, 1045–1047 (1988).

[98] P. J. Mulhern, T. Hubbard, C. S. Arnold, B. L. Blackford, and M. H. Jericho. A scanning force microscope with a fiber-optic-interferometer displacement sensor, *Review of Scientific Instruments* **62**, 1280–1284 (1991).

[99] Kenji Numata, Masaki Ando, Kazuhiro Yamamoto, Shigemi Otsuka, and Kimio Tsubono. Wide-band direct measurement of thermal fluctuations in an interferometer, *Phys. Rev. Lett.* **91**, 260602 (2003).

[100] J. W. Obreimoff. The Splitting Strength of Mica, *Proceedings of the Royal Society of London. Series A* **127**, 290–297 (1930).

[101] A. Oral, R. A. Grimble, H. Ö. Özer, and J. B. Pethica. High-sensitivity noncontact atomic force microscope/scanning tunneling microscope (nc afm/stm) operating at subangstrom oscillation amplitudes for atomic resolution imaging and force spectroscopy, *Review of Scientific Instruments* **74**, 3656–3663 (2003).

[102] Xabier Oyharcabal and Thomas Frisch. Peeling off an elastica from a smooth attractive substrate, *Phys. Rev. E* **71**, 036611 (2005).

[103] P. Paolino and L. Bellon. Single beam interferometric angle measurement, *Optics Communication* **280**, 1–9 (2007).

[104] P. Paolino and L. Bellon. Frequency dependence of viscous and viscoelastic dissipation in coated micro-cantilevers from noise measurement, *Nanotechnology* **20**, 405705 (2009).

[105] Pierdomenico Paolino. *Bruit thermique et dissipation d'un microlevier*. PhD thesis, École Normale Supérieure de Lyon, 11 2008. – `http://tel.archives-ouvertes.fr/tel-00423692`.

[106] Pierdomenico Paolino and Ludovic Bellon. Quadrature phase interferometer for afm measurements, *in preparation* (2010).

[107] Pierdomenico Paolino, Bruno Tiribilli, and Ludovic Bellon. Direct measurement of spatial modes of a microcantilever from thermal noise, *Journal of Applied Physics* **106**, 094313 (2009).

[108] Shivprasad Patil, George Matei, Hang Dong, Peter M. Hoffmann, Mustafa Karaköse, and Ahmet Oral. A highly sensitive atomic force microscope for linear measurements of molecular forces in liquids, *Review of Scientific Instruments* **76**, 103705 (2005).

[109] M. R. Paul and M. C. Cross. Stochastic dynamics of nanoscale mechanical oscillators immersed in a viscous fluid, *Phys. Rev. Lett.* **92**, 235501 (2004).

[110] M R Paul, M T Clark, and M C Cross. The stochastic dynamics of micron and nanoscale elastic cantilevers in fluid: fluctuations from dissipation, *Nanotechnology* **17**, 4502–4513 (2006).

[111] Olivier Pitois, Pascal Moucheront, and Xavier Chateau. Liquid bridge between two moving spheres: An experimental study of viscosity effects, *Journal of Colloid and Interface Science* **231**, 26 – 31 (2000).

[112] Constant A. J. Putman, Bart G. De Grooth, Niek F. Van Hulst, and Jan Greve. A detailed analysis of the optical beam deflection technique for use in atomic force microscopy, *Journal of Applied Physics* **72**, 6–12 (1992).

[113] Manfred Radmacher. Studying the mechanics of cellular processes by atomic force microscopy. In Yu[hyphen (true graphic)]Li Wang and Dennis E. Discher, editors, *Cell Mechanics*, volume 83 of *Methods in Cell Biology*, pages 347–372. Academic Press, 2007.

[114] Arvind Raman. private communication:. in [135], the units corresponding to figure 5 should read fJ instead of nJ. In part 4, units for interfacial energies per unit length should read nJ/m instead of pJ/m, and should be considered as lower bounds (instead of upper bounds), 2010.

[115] S. Rowan, J. Hough, and D.R.M. Crooks. Thermal noise and material issues for gravitational wave detectors, *Physics Letters A* **347**, 25 – 32 (2005). Einstein Special Issue - Special Issue in celebration of this year's World of Physics and the centenary of Einstein's annus mirabilis.

[116] D. Rugar, H. J. Mamin, R. Erlandsson, J. E. Stern, and B. D. Terris. Force microscope using a fiber-optic displacement sensor, *Review of Scientific Instruments* **59**, 2337–2340 (1988).

[117] D. Rugar, H. J. Mamin, and P. Guethner. Improved fiber-optic interferometer for atomic force microscopy, *Appl. Phys. Lett.* **55**, 2588–2590 (1989).

[118] John Russo and Francesco Sciortino. How do self-assembling polymers and gels age compared to glasses?, *Phys. Rev. Lett.* **104**, 195701 (2010).

[119] John Elie Sader. Frequency response of cantilever beams immersed in viscous fluids with applications to the atomic force microscope, *Journal of Applied Physics* **84**, 64–76 (1998).

[120] M. V. Salapaka, H. S. Bergh, J. Lai, A. Majumdar, and E. McFarland. Multi-mode noise analysis of cantilevers for scanning probe microscopy, *Journal of Applied Physics* **81**, 2480–2487 (1997).

[121] Jean-Paul Salvetat, G. Andrew D. Briggs, Jean-Marc Bonard, Revathi R. Bacsa, Andrzej J. Kulik, Thomas Stöckli, Nancy A. Burnham, and László Forró. Elastic and shear moduli of single-walled carbon nanotube ropes, *Phys. Rev. Lett.* **82**, 944–947 (1999).

[122] R Sandberg, K Mølhave, A Boisen, and W Svendsen. Effect of gold coating on the q-factor of a resonant cantilever, *Journal of Micromechanics and Microengineering* **15**, 2249–2253 (2005).

[123] Naruo Sasaki, Arihiro Toyoda, Noriaki Itamura, and Kouji Miura. Simulation of nanoscale peeling and adhesion of single-walled carbon nanotube on graphite surface, *e-Journal of Surface Science and Nanotechnology* **6**, 72–78 (2008).

[124] Peter R. Saulson. Thermal noise in mechanical experiments, *Phys. Rev. D* **42**, 2437–2445 (1990).

[125] Francesca Sbrana, Chiara Sassoli, Elisabetta Meacci, Daniele Nosi, Roberta Squecco, Ferdinando Paternostro, Bruno Tiribilli, Sandra Zecchi-Orlandini, Fabio Francini, and Lucia Formigli. Role for stress fiber contraction in surface tension development and stretch-activated channel regulation in C2C12 myoblasts, *Am J Physiol Cell Physiol* **295**, C160–172 (2008).

[126] Tilman E Schäffer. Calculation of thermal noise in an atomic force microscope with a finite optical spot size, *Nanotechnology* **16**, 664–670 (2005).

[127] B. Schnurr, F. Gittes, F. C. MacKintosh, and C. F. Schmidt. Determining microscopic viscoelasticity in flexible and semiflexible polymer networks from thermal fluctuations, *Macromolecules* **30**, 7781–7792 (1997).

[128] C. Schonenberger and S. F. Alvarado. A differential interferometer for force microscopy, *Review of Scientific Instruments* **60**, 3131–3134 (1989).

[129] Udo Seifert. Adhesion of vesicles in two dimensions, *Phys. Rev. A* **43**, 6803–6814 (1991).

[130] Benjamin S. Sheard, Malcolm B. Gray, Conor M. Mow-Lowry, David E. McClelland, and Stanley E. Whitcomb. Observation and characterization of an optical spring, *Phys. Rev. A* **69**, 051801 (2004).

[131] K. S. Sinnathamby, H. Oukris, and N. E. Israeloff. Local polarization fluctuations in an aging glass, *Physical Review Letters* **95**, 067205 (2005).

[132] Peter Sollich, Suzanne Fielding, and Peter Mayer. Fluctuation-dissipation relations and effective temperatures in simple non-mean field systems, *Journal of Physics: Condensed Matter* **14**, 1683 (2002).

[133] M C Strus, A Raman, C-S Han, and C V Nguyen. Imaging artefacts in atomic force microscopy with carbon nanotube tips, *Nanotechnology* **16**, 2482 (2005).

[134] M. C. Strus, L. Zalamea, A. Raman, R. B. Pipes, C. V. Nguyen, and E. A. Stach. Peeling force spectroscopy: Exposing the adhesive nanomechanics of one-dimensional nanostructures, *Nano Letters* **8**, 544–550 (2008).

[135] Mark C. Strus, Camilo I. Cano, R. Byron Pipes, Cattien V. Nguyen, and Arvind Raman. Interfacial energy between carbon nanotubes and polymers measured from nanoscale peel tests in the atomic force microscope, *Composites Science and Technology* **69**, 1580 – 1586 (2009).

[136] Cornelis A. Van Eysden and John E. Sader. Frequency response of cantilever beams immersed in viscous fluids with applications to the atomic force microscope: Arbitrary mode order, *Journal of Applied Physics* **101**, 044908 (2007).

[137] M. Vial, L. Bellon, and R. H. Hernandez. Mechanical forcing of the wake of a flat plate, *Experiments in Fluids* **37**, 168–176 (2004). 25.

[138] E. Vidal Russell and N. E. Israeloff. Direct observation of molecular cooperativity near the glass transition, *Nature* **408**, 695 (2000).

[139] M. Vogel, C. Mooser, K. Karrai, and R. J. Warburton. Optically tunable mechanics of microlevers, *Applied Physics Letters* **83**, 1337–1339 (2003).

[140] H. Walther. Internal friction in solids, *Scientific monthly* **41**, 275 (1935).

[141] S. M. Wiederhorn. Influence of water vapor on crack propagation in soda-lime glass, *Journal of the American Ceramic Society* **50**, 407–414 (1967).

[142] Christopher D. Willett, Michael J. Adams, Simon A. Johnson, and Jonathan P. K. Seville. Capillary bridges between two spherical bodies, *Langmuir* **16**, 9396–9405 (2000).

[143] J. J. Wortman and R. A. Evans. Young's modulus, shear modulus, and poisson's ratio in silicon and germanium, *Journal of Applied Physics* **36**, 153–156 (1965).

[144] Hui Xie and Stéphane Régnier. In situ peeling of one-dimensional nanostructures using a dual-probe nanotweezer, *Review of Scientific Instruments* **81**, 035112 (2010).

[145] Kazuhiro Yamamoto, Shigemi Otsuka, Masaki Ando, Keita Kawabe, and Kimio Tsubono. Experimental study of thermal noise caused by an inhomogeneously distributed loss, *Physics Letters A* **280**, 289 – 296 (2001).

[146] K.Y. Yasumura, T.D. Stowe, E.M. Chow, T. Pfafman, T.W. Kenny, B.C. Stipe, and D. Rugar. Quality factors in micron- and submicron-thick cantilevers, *Journal of Microelectromechanical Systems* **9**, 117–125 (2000).

[147] C. Zener, W. Otis, and R. Nuckolls. Internal friction in solids iii. experimental demonstration of thermoelastic internal friction, *Phys. Rev.* **53**, 100–101 (1938).

[148] Clarence Zener. Internal friction in solids. i. theory of internal friction in reeds, *Phys. Rev.* **52**, 230–235 (1937).

[149] Clarence Zener. Internal friction in solids ii. general theory of thermoelastic internal friction, *Phys. Rev.* **53**, 90–99 (1938).

[150] Kun Zhang. *Mesostructured porous materials: pore and surface engineering towards bio-inspired synthesis of heterogeneous copper catalysts*. PhD thesis, École Normale Supérieure de Lyon, 07 2008. – http://tel.archives-ouvertes.fr/tel-00310153.

Abstract

This mémoire presents my current research interests in micro and nano-mechanics in a comprehensive manuscript. Our experimental device is first presented: this atomic force microscope, designed and realized in the Laboratoire de Physique de l'ENS Lyon, is based on a quadrature phase differential interferometer. It features a very high resolution (down to $10^{-14}\,\mathrm{m}/\sqrt{\mathrm{Hz}}$) in the measurement of deflexion, down to low frequencies and on a huge input range. The dual output of the interferometer implies a specific handling to interface common scanning probe microscope controllers. We developed analog circuitries to tackle static (contact mode) and dynamic (tapping mode) operations, and we demonstrate their performance by imaging a simple calibration sample.

As a first application, we used the high sensitivity of our interferometer to study the mechanical behavior of micro-cantilevers from their fluctuations. The keystone of the analysis is the Fluctuation-Dissipation Theorem (FDT), relating the thermal noise spectrum to the dissipative part of the response. We apply this strategy to confront Sader's model for viscous dissipation with measurements on raw silicon cantilevers in air, demonstrating an excellent agreement. When a gold coating is added, the thermal noise is strongly modified, presenting a $1/f$ like trend at low frequencies: we show that this behavior is due to a viscoelastic damping, and we provide a quantitative phenomenological model. We also characterize the mechanical properties of cantilevers (stiffness and Elastic Moduli) from a mapping of the thermal noise on their surface. This analysis validates the description of the system in term of its normal modes of oscillations in an Euler-Bernoulli framework for flexion and in Saint-Venant approach for torsion, but points toward a refined model for the dispersion relation of torsional modes.

Finally, we present peeling experiments on a single wall carbon nanotube attached to the cantilever tip. It is pushed against a flat substrate, and we measure the quasi-static force as well as the dynamic stiffness using an analysis of the thermal noise during this process. The most striking feature of these two observables is a plateau curve for a large range of compression, the values of which are substrate dependent. We use the Elastica to describe the shape of the nanotube, and a simple energy of adhesion per unit length E_a to describe the interaction with the substrate. We analytically derive a complete description of the expected behavior in the limit of long nanotubes. The analysis of the experimental data within this simple framework naturally leads to every quantity of interest in the problem: the force plateau is a direct measurement of the energy of adhesion E_a for each substrate, and we easily determine the mechanical properties of the nanotube itself.